Large area of Ultrathin Alumina Membranes Toward Innovative Heterogeneous Nanostructure Arrays for Solar Energy Conversion

Dissertation

zur Erlangung des Doktorgrades

Dr. rer. nat.

vorgelegt der

Fakultät für Mathematik und Naturwissenschaften der

Technischen Universität Ilmenau

von

M. Sc. Ahmed Shukur Hameed Al-Haddad

Ilmenau

Doktorvater und 1. Gutachter: Prof. Dr. Yong Lei

2. Gutachter: Prof. Dr. Michael Köhler

3. Gutachter: Prof. Dr. Pu-Xian Gao

Tag der Einreichung: 24.05.2016

Tag der wissenschaftlichen Aussprache: 30.09.2016

urn: nbn: de: gbv: ilm1- 2016000479

Gedruckt mit Unterstützung des Deutschen Akademischen Austauschdienstes

Abstract

Ordered nanostructure arrays are attracting intensive scientific attention because of their many and varied applications. However, it is still a challenge to achieve ordered nanostructure patterning over a relatively large area (for instance on the wafer scale) by a technique that will allow high throughput, large pattern area and low equipment costs. Part of the work reported here is the achievement of facile transferring of ultrathin alumina membranes (UTAMs) which have been attached on wafer-scale substrates without any twisting, folding, cracking or contamination because of the unique design of the fabrication and transferring processes. The crucial element of this method is fixing the prepared 4-inch UTAM onto a wafer-scale substrate before removing the remaining Al and the alumina barrier layer. The thickness and surface smoothing of the UTAMs play a vital role in this process. By using these perfectly transferred UTAMs as masks, various nanostructuring patterns including nanoparticles, nanomeshes, and nanowire arrays have been fabricated on wafer-scale substrates with tunable and uniform dimensions. The method is a template method, which is not reliant on a specific requirement for the UTAMs, the substrates and the deposited materials. It thus provides a cost-effective platform for the fabrication of ordered nanostructures on large substrates for a range of applications in nanotechnology.

The work has included fabricating hexagonal arrays of TiO_2 nanotubes (TNTs) with an excellent crystalline quality by techniques combining anodic aluminum oxide templates and atomic layer deposition (ALD). Absorption spectroscopic analysis showed that the optical absorption band edge of the TNTs exhibited a red shift as the diameter of the nanotubes was tuned to be larger and the distance between two nanotubes became smaller, while the wall thickness of the nanotube was kept constant. Subsequent finite-difference time-domain simulations supported the observation from the theoretical aspect and

revealed a large near-field enhancement around the nanotubes for the arrays with densely distributed nanotubes when the corresponding arrays were illuminated. These were results which provided a new perspective on the shift of the optical band gap, which is of significance to research in photoelectronics. In addition, the prepared CdTe/TiO_2 core-shell nanowire arrays with various diameters showed an improvement in photoelectrochemical (PEC) water splitting and in photovoltaic properties. By tuning diameters of CdTe/TiO_2 nanowire arrays, it was possible to achieve photocurrent as high as 1.1 mA cm^{-2}.

Unlike many previously reported heterogeneous photoelectrodes that adopt core/shell configurations and are based on connected UTAMs, in the present work TNTs╫Si and TNWs┼Si heterostructures with a configuration of TiO_2 nanotubes or nanowires were prepared vertically rooted into Si substrate for PEC water splitting. The unique structure of the TNTs╫Si heterostructure enabled the PEC performance of TNTs╫Si heterostructures to be among the best of heterogeneous photoelectrodes based on TiO_2 and Si, while maintaining excellent structural stability during the water oxidation reaction. In addition, the TNWs┼Si heterostructure served better to enhance the photovoltaic did the TNTs╫Si heterostructures. The fabrication technique enabled such heterostructure arrays to be easily produced on a large scale. Importantly, the fabrication strategy is universal, leaving enough space for structure optimization and selection of the materials for heterostructure arrays, which will benefit solar energy applications.

Zusammenfassun

Geordnete Nanostruktur-Arrays haben viel Aufmerksamkeit erfahren durch ihre vielfältigen Anwendungen. Jedoch ist es noch immer eine große Herausforderung geordnete Nanostrukturen über eine große Fläche (wie z.B. Wafer-Größe) durch Methoden die einen hohen Durchsatz bei großen Flächen und geringen Gerätekosten ermöglichen herzustellen. Hier, durch ein einzigartiges Design für den Herstellungs- und Transferprozess, konnten wir einen einfachen Transfer von wafer-großen gebundenen ultradünnen Aluminium-Membranen (UTAMs) auf Substrate ohne Verdrehen, Faltung, Einreißen oder Verunreinigungen erreichen. Das wichtigste unserer Methode ist das Anheften der 4 Inch großen UTAMs auf wafer-große Substrate vor dem Entfernen des Rückseitenaluminiums und der Aluminiumoxidschicht (sog. Barrier Layer). Es wird auch gezeigt, dass die Dicke und das Glätten der Oberflächen der UTAMs eine wichtige Rolle in dem Prozess spielen. Durch perfekt transferierte UTAMs als Masken werden viele unterschiedliche Nanostruktur-Anordnungen wie Nanopartikel, Nanomeshs, und Nanowire-Arrays auf wafer-großen Substraten hergestellt mit einstellbaren und einheitlichen Abmessungen. Weil es für UTAMs keine Limitierungen was Substrate und abzuscheidende Materialien gibt repräsentiert die Methode eine kostengünstige und effiziente Möglichkeit zur Herstellung von geordneten Nanostrukturen auf großflächigen Substraten für viele Anwendungen der Nanotechnologie.

Zusätzlich wurden hexagonale TiO_2 Nanotube-Arrays mit exzellenter Kristallqualität durch die Kombination von anodischen Aluminiumoxid (AAO)-Templaten und Atomlagenabscheidung (ALD) hergestellt. Durch spektroskopische Absorptionsmessungen haben wir beobachtet, dass die optische Absorptionsbandkante der TiO_2 Nanotube-Arrays eine Rotverschiebung erfährt mit steigendem Durchmesser der Nanotubes und entsprechend kleineren Abstand zwischen den einzelnen Nanotubes, während die Wandstärke konstant gehalten wurde.

Nachfolgende FDTD-Simulationen unterstützten diese Beobachtung im Blick auf den theoretischen Hintergrund und machten eine große Nahfeldverstärkung im Außenbereich der Nanotubes deutlich für Arrays mit dicht angeordneten Nanotubes wenn diese beleuchtet wurden. Demnach liefern diese Ergebnisse eine neue Perspektive auf die Verschiebung der optischen Bandlücke, was von großer Bedeutung für die Forschung im Bereich Photoelektronik ist. Andererseits zeigten die hergestellten CdTe/TiO_2 Core-Shell-Nanowire-Arrays mit unterschiedlichen Durchmessern eine Verbesserung der photoelektrischen Wasserspaltung und der photovoltaischen Eigenschaften. Durch Modulation der Durchmesser konnte ein optimierter Photostrom von 1,1 mA/cm² erreicht werden.

Im Gegensatz zu vielen vorherigen heterogenen Photoelektroden die Core/Shell Konfigurationen anwenden, basierend auf verbundenen UTAMs, TNTs╫Si und TNWs┼Si Heterostrukturen mit einer Konfiguration aus TiO_2 Nanotubes oder Nanowires wurden vertical verwurzelt im Si-Substrat für PEC Wasserspaltung. Die einzigartige Struktur der TNTs╫Si Heterostrukturen ermöglicht eine PEC Performance, die unter den Besten der heterogenen Photoelektroden basierend auf TiO_2 und Si ist, während eine exzellente strukturelle Stabilität während der Wasser-Oxidations-Reaktion gegeben ist. Zusätzlich kann die TNWs┼Si Heterostruktur die photovoltaischen Eigenschaften stärker als andere Heterostrukturen verbessern. Die Herstellungsmethode erlaubt es diese Heterostruktur-Arrays einfach und in Massenfertigung zu produzieren und ebenfalls wichtig, die Methode ist universell einsetzbar und lässt genug Spielraum für strukturelle Optimierungen sowie weitere Materialien für Heterostruktur-Arrays für Verbesserungen in Richtung solarer Energieanwendungen.

Acknowledgement

First of all, I would like to express my deepest gratitude to my advisor Professor Yong Lei. I thank him for the opportunity to join his group, for his continuous support throughout my Ph.D. studies and related research; for his patience, motivation, and immense knowledge. His guidance has helped me during my academic research in his group; I could not have imagined having a better advisor and mentor for my Ph.D. studies. He has also encouraged me into academic activities such as conference management and a range of teaching activities. In addition, I thank him for all the social activities and rich memories that we shared in the past years.

In daily lab work, I have been blessed with a friendly and cheerful group, great thanks to all of my colleagues from our group for their inspiring working environment. My special thanks go to Dr. Huaping Zhao, Dr. Zhijie Wang, Dr. Chengliang Wang, Dr. Zhibing Zhan and Mr. Rui Xu for their fruitful scientific discussions and knowledge exchanging and many kinds of activities. I sincerely thank Ms. Samar Tarish, Mr. Ranjith Vellacheri, Dr. Liaoyong Wen and Mr. Max Sommerfeld for their friendship; they have always been willing to help and give their best suggestions.

In regard to measurements, I would like to thank Dr. Haoyuan Qi and Mr. Jörg Bernhard from Professor Ute Kaiser's group at the University of Ulm for their effort, time and valuable discussion on TEM measurements. I also thank Dr. Henry Romanus, Dr. Alexander Konkin, Ms. Manuela Breiter and Mr. Joachim Döll for discussions and suggestions during the respective measurements like TEM, UV-vis spectroscopy, Si etching and sample cutting.

I also would like to acknowledge the financial support of the MOHESR/DAAD Iraqi-German scholarship program for the Ph.D. fellowship with its opportunity to me to live in Germany and learn more about German culture.

Last but not least; an acknowledgement of my family. Very special thanks go to my wife for her constant support, her patience and her care of our children during my Ph.D. studies. To my parents, brothers and sisters go my thanks for supporting me spiritually through my life in general and for all their love, care and encouragement.

Ilmenau, May 2016
Ahmed Al-Haddad

Table of Content

A. List of Figures

B. List of Tables

List of Abbreviations

1-D	One-dimensional
2-D	Two-dimensional
3-D	Three-dimensional
α	Optical absorption coefficient near
A-UTAM	Attached ultrathin alumina membrane
AAO	Anodic aluminum oxide
ABPE	Applied bias photon-to-current efficiency
Al	Aluminum
Al_2O_3	Aluminium oxide
ALD	Atomic layer deposition
ALE	Atomic layer epitaxy
Au	Gold
AZO	aluminum doped zinc oxide
B_L	Barrier layer
C-UTAM	Connected ultrathin alumina membrane
CdTe	Cadmium telluride
DI	Deionized
CB	Conduction band
CNT	Carbon nanotube
CVD	Chemical vapor deposition
ΔG	Free energy change for conversion H_2O to H_2 and 1/2 O_2
D_C	Cell diameter
D_P	Pore diameter
d_S	Interpore distances
EBE	E-beam evaporation
EBL	Electron beam lithography
E_c	Edge of conduction band
ECD	Electrochemical deposition
EDX	Energy-dispersive detector X-rays
E_f	Fermi level
E_f^*	Quasi-Fermi level
E_g	Bandgap energy
ELP	Electroless plating
EQE	External quantum efficiency
E_{RHE}	Applied potential versus hydrogen electrode
E_v	Edge of valence band
FAB	Fast atom beam
FDTD	Finite-difference time-domain

FE-SEM	Field emission scanning electron microscopy
FFT	Fast Fourier transform
FIB	Focus ion beam
H_2	Hydrogen
hν	Photon energy
HRTEM	High-resolution transmission electron microscopy
I-V	Current-voltage
ICP	Inductively coupled plasma
IBID	Ion beam induced deposition
II	Ion implantation
IM	Ion milling
IPCE	Incident photon to charge carrier efficiency
J-V	Current density-voltage
J_{ph}	Photocurrent density
MBE	Molecular beam epitaxy
MaCE	Metal-assisted chemical etching
MOCVD	Metalorganic chemical vapor deposition
NP	Nanopillar
NR	Nanoring
NS	Nanosphere
NT	Nanotube
O_2	Oxygen
P_d	Pore density
PE	Plasma etching
PEC	Photoelectrochemical
PECVD	Plasma enhanced chemical vapor deposition
P_h	Surface area of a single hexagonal cell
P_{in}	Power density
PLD	Pulsed laser deposition
PMMA	Polymethyl methacrylate
Pt(MeCp)Me_3	Trimethyl(methylcyclopentadienyl)platinum(IV)
PVD	Physical vapor deposition
RIE	Reactive ion etching
SE	Secondary electron
SAED	Selected area electron diffraction
SEM	Scanning electron microscope
Si	Silicon
SP	Sputtering
SPM	Scanning probe microscopy
τ	Decay constants
TE	Thermal evaporation
TEM	Transmission electron microscopy

Ti	Titanium
TiO_2	Titanium dioxide
TNT	Titanium dioxide nanotube
TNW	Titanium dioxide nanowire
U	Anodization potential
$U_{f\text{-}b}$	Flat-band potential
UTAM	Ultrathin alumina membrane
V_{app}	Applied potential
VE	Vacuum evaporation
VLS	Vapor–liquid–solid
W_t	Wall thickness
XRD	X-ray diffraction

1. Introduction

One of the applications of nanotechnology is to help improve the performance of solar energy conversion. On the nanoscale (less than 100 nanometers), several physical phenomena have been reported in which the nanomaterials behave unexpectedly, and can exhibit different properties than does the material in the bulk state. Although nanotechnology is still in the development stage, nanostructured materials are already intensively used in various fields such as biomedicine,[1-3] sensors,[4] photonics,[5, 6] and photovoltaics.[5, 7]. The unique optical properties of semiconductor nanostructures have been extensively studied in the respect of quantum confinement effects: when the dimensions of semiconductors are at or below the characteristic size (for instance the exciton Bohr radius), the bandgap becomes larger in comparison with the relevant bulk material, and a blue shift of the optical absorption ensues. The phenomenon is caused by localization of electrons and holes in a confined space, resulting in observable quantization of the energy levels of the electrons.[8-10] In this case, the optical properties of nanomaterials present a series of features that the bulk materials do not possess. However, excluding the quantum effects, other geometrical factors that influence the optical bandgap of semiconductors have rarely been reported.[11, 12]

With the nanostructured materials, an improvement has been shown in the light harvesting efficiency and in the solar energy conversion (thermal storage, electricity, and fuel). The current challenges in nanostructured materials include how to generate the nanostructure over large areas at low cost while ensuring well-defined and innovative nanostructures. Another challenge is to improve understanding of nanomaterials for this is crucial to the design of new nanostructures and the multiple junctions, multiple exciton generation, multiple levels of energy, and hot-carrier junctions which would help

maximize the conversion of light energy. Ordered nanostructure arrays are another focus. They have important applications in various fields, such as in optoelectronics, energy conversion, sensing, and data storage.[13-17] In order to achieve ordered nanostructure patterning over a large area for device applications, various methods have been adopted lithographical processes,[18, 19] imprinting techniques[20-23] or self-assembly methods.[24-28] Among these, the lithographical processes and imprinting techniques require expensive and complex equipment and costly imprinting stamps respectively. The self-assembly method is capable of cost-effective and large-scale nanostructuring, but usually suffers from low structural regularity and poor uniformity.[25] As an alternative to these methods, template-based nanostructuring, especially using an anodic aluminum oxide (AAO) nanoporous template, is cost-effective in producing large scale nanostructure arrays or patterns with high regularity. Generally, the AAO template is adopted for synthesizing one-dimensional (1-D) nanostructure arrays in self-organized nanopore arrays[13, 14, 27, 29-31] or for replicating into metallic or semiconductor nanostructures,[32-35] because of the advantages in cost, ease of fabrication, and high manipulability.[36-38] Accordingly, a large diversity of nanostructure arrays has been realized, including nanopores, nanodots, nanorods, nanotubes, and even nanocones.[39-41]

It is shown in this dissertation and in already published papers from Professor Lei's group (in which this dissertation has been developed) that a special AAO template, ultrathin alumina membrane (UTAM), can be used as a deposition or etching mask for achieving ordered nanoparticle arrays or surface patterns with nanopores on substrates.[36-38, 42] UTAM maintains the advantages of an AAO template, including the uniformity and high density of self-organized nanopores, and the tunability of pore parameters (diameter, length and interspacing).[43] Two types of UTAMs have been devised, namely connected and attached UTAMs.[36-38, 42] Although the connected UTAM has good adhesion to the

substrate and the capacity to form nanopore arrays on a relatively large scale, it suffers from the drawbacks of low regularity of the nanopores and difficult complete removal of the barrier layer,[21-23] These drawbacks limit its application potential. However, the attached type of UTAM has also its limitations in wet-chemical processes [37] and attaching the UTAM to the substrate is a great challenge.[37] Because of its ultrathin and fragile nature, direct transfer of freestanding UTAMs on substrates usually results in the twisting, folding or cracking of UTAMs. For this reason, an organic supporting layer (e.g., PMMA) is normally exploited for transferring the UTAM onto a substrate.[20, 37] However, this organic-assistant process could contaminate the substrate and cause non-uniformity of the UTAM pores. Moreover, after the organic layer has been removed, it is difficult to obtain a perfect and flat UTAM attached to a substrate with a large area.

One intensive use of the AAO templates is to realize core-shell nanostructure arrays which enhance light harvesting efficiency. Recently, considerable efforts have been made to develop heterogeneous photoelectrodes for highly efficient solar-to-fuel conversion. Generally, these heterogeneous photoelectrodes are full of promise for solar water splitting and high light-harvesting efficiency. They offer a large solid-solid contact interface to promote the photogenerated electrons from the conduction band of photocatalyst I and holes from the valence band of photocatalyst II. This feature should facilitate the balanced distribution of incident photons between photocatalyst I and photocatalyst II, so that the utilization efficiency of solar light is maximized.[44-47] Accordingly, there are mainly two factors which influence the performance of heterogeneous photoelectrodes for solar energy conversion: components and configuration. The two components for constructing heterogeneous photoelectrodes should have well-matched energy levels to form a dual bandgap configuration that allows the majority of photogenerated charge carriers in the semiconductors to recombine at the interface, resulting in higher theoretical energy

conversion efficiency than that of a single bandgap configuration. The second factor, the configuration of heterogeneous photoelectrodes, has long been considered to have significant influence on light harvesting and charge separation, and subsequently on the photocatalytic efficiency.[48-50]

With an appropriate configuration, the realization of a direct solar-to-fuel device, i.e. solar water splitting to convert sunlight energy into chemical energy by splitting water to produce oxygen (O_2) and hydrogen (H_2) equivalents, offers a promising solution toward less reliance on fossil fuels.[51-54] In solar-driven water splitting, one of the main issues is to develop photoelectrodes possessing high efficiency and long-term durability in an aqueous environment.[55-57] Therefore, in current research efforts, new photocatalysts for photoelectrodes are being explored and novel photoelectrode architectures designed.[48, 58-60] Ideally, water can be efficiently split into H_2 and O_2 using photogenerated electrons and holes under illumination in a single semiconductor material with a large enough bandgap as well as a conduction band-edge energy and valence band-edge energy that straddles the electrochemical potentials for both H_2 evolution reaction and O_2 evolution reaction.[61, 62] Unfortunately, there is no single semiconductor material that can satisfy all these requirements (i.e., suitable bandgap energies for efficient solar energy absorption and at the same time the band-edges aligned with both the H_2 and O_2 redox potential of water).[53] It is therefore advantageous to utilize heterogeneous photoelectrodes (on the so-called Z-scheme) which offer the opportunities to overcome the drawbacks of a single semiconductor photocatalyst and fulfill all the requirements for improving solar-to-fuel conversion efficiency.[54, 63]

The main goal of this study was to design a new nanostructure that would optimize the light absorption for solar energy conversion applications, under the condition that these nanostructures must be realized in large area, highly ordered arrays, well-controlled

morphology, and low cost of the fabrication. In order to face these challenges and atempt to solve the major dificulties of the UTAM technology for both attached and connected UTAMs, adaptations were made enabling UTAMs to serve the desired purpose. The result is a cost-effective pattern technology which can compete with the other lithographic and nonlithographic techniques for forming the functional nanopattern devices.

2. Outline of dissertation

Chapter 2 describes the principle formation of anodic aluminum oxide nanoporous templates, and the unique features of this template technique. It is also covers the challenges of both types of ultrathin alumina membrane (A-UTAM and C-UTAM) and the major theoretical and experimental previous work that led to interest in AAO templates for a wide range of applications. The chapter also introduces atomic layer deposition (ALD), stating how important it can be to combine the ALD with an AAO template to produce highly controllable nanostructure morphology. TiO_2 nanotube arrays (TNTs) for photocatalytic water splitting are presented together with the basic principle of the water splitting mechanism.

Chapter 3 addresses the main challenge to using A-UTAM for a large area. The challenge is met: 4-inch of UTAM of varied thickness (40 – 320 nm) is transferred onto Si wafers with neither twisting, folding, cracking of UTAMs nor contamination to the substrate. The crucial factors in this successful transfer of large scale UTAMs are the treatment of the UTAM surface and the fixing of the UTAM onto the substrate before the remaining Al foil is removed. Moreover, nanostructures in various patterns are achieved over wafer-scale areas, including nanoparticle, nanomesh, and nanowire arrays with tunable and uniform dimensions.

Chapter 4 focuses on the TNTs with the preparation and the tuning of the morphology parameters to improve the suggested solar energy devices. Two crucial factors that directly affect the related solar energy applications receive attention. It is suggested that periodical parameters can also be utilized to manipulate the optical band gap of the TNTs. Second, highly ordered TNTs with excellent crystal quality are fabricated by techniques combining anodic aluminum oxide templates and atomic layer deposition. Through absorption spectroscopic analysis, it was observed that the optical absorption band edge of the TNTs exhibited a red shift as the diameter of the nanotube was tuned to be larger and the distance between two nanotubes thus became smaller, while the thickness of the wall of the nanotube was kept constant. Finite-difference time-domain simulations carried out on the structures created supports the observation from the theoretical aspect and reveals a large near-field enhancement around the nanotubes for the arrays with densely distributed nanotubes on the illumination of the corresponding arrays. In addition, unlike the conventional ALD method of preparing the materials, which usually results in low crystallinity, the specific two-step ALD procedure integrated with the annealing treatment is a means of achieving better crystal quality and has proved to be more than acceptable as a method of producing nanostructures with high crystal quality.

Chapter 5 describes well-ordered CdTe/TiO_2 nanowire arrays with high crystalline quality which are realized by a convenient template-directed method and are based on the concept of chapter 4. The tunable dimension of the template enables the size of the resulting CdTe/TiO_2 nanowire arrays to be manipulated. Thus, both absorption and photoelectrochemical properties of the composite architecture prove to be highly tunable and capable of optimization. Second, in comparison with the photoanode which only has a TiO_2 nanotube array, the CdTe/TiO_2 electrodes are dramatically improved in performance.

It is also shown that the performance of Au/CdTe/TiO_2/AZO can be optimized when the diameter is increased from 30 nm to 90 nm.

The focus shifts in Chapter 6 onto solving the barrier layer problem of C-UTAM. Furthermore, two novel heterostructures (TNTs╫Si and TNWs┼Si) are designed with a configuration of TiO_2 nanotubes or nanowires vertically rooted into a Si substrate for photoelectrochemical (PEC) water splitting. The design serves as a proof of concept for the UTAM approach. Many advantages have already been realized. The first is the enhancement of the light harvesting efficiency. Another is the large contact area at the Si/TiO_2 interface offered by the bottom Si/TiO_2 core/shell structure for the recombination of the majority of photogenerated charge carriers. Yet another is the high aspect ratio of freestanding TiO_2 nanotubes: they have a large TiO_2-electrolyte interfacial area to provide abundant reactive sites for the water oxidation reactions. They also have excellent structural stability during the water oxidation reaction. Furthermore, the photovoltaic properties are enhanced by using a TNWs┼Si heterostructure rather than the nanotube arrays patterned onto substrate.

The results included in this dissertation are summarized in Chapter 7, which concludes with thoughts on the outlook.

Chapter 8 goes on to represent the extended work, describing a nonlithographic technique to fabricate multi-core-shell nanowire arrays with separated electrodes and semiconductor situated in every core-shell nanostructure for resistive switching memories. The procedure for fabrication of nanodevice arrays over a large area can be used for producing many other different materials. Such three-dimensional electronic device arrays susceptible to adjustment of the device densities can be extended to yet more applications in the next generation of nanodevice technology.

It should be mentioned that certain chapters represent one or more papers published in or submitted to SCI-indexed international scientific journals, including chapter 3, 4, 5, 6 and 8. It should also be noted that in this dissertation, relevant chapters are self-contained, presenting not only the challenges but how they were resolved.

2. General Background

2.1. Introduction

This chapter concentrates on the basic description and fabricating principles of anodic aluminum oxide nanoporous templates, and the challenges of the two types of ultrathin alumina membrane. In addition, it provides an introduction to the deposition of the atomic layer and its efficient combination with an AAO template to produce nanostructures with highly controllable morphology. It also describes the basic principles of the water splitting mechanism based on a TiO_2 model.

2.2. Structural characteristics of the AAO template

In 1953 Keller et al. used transmission electron microscopy (TEM) to analyze anodized aluminum film, discovered its porous nature and defined the hexagonally closed packed pore arrays for the first time as an ideal structure of anodic aluminum oxide (AAO).[64] In 1995 Masuda and Fukuda described the particular anodization conditions required for producing the ideal structure of AAO.[65] From then on, AAO templates attracted intensive attention for the synthesizing of low-dimensional nanostructures.[66-69]

In general, high-purity Al (foil or thin film) when anodized forms a close-packed hexagonal cell array. Each cell has at its center a cylindrical pore perpendicular to the surface and each cell is separated by the pore wall (Al_2O_3) from the next cell. The end of pore is separated from the underlying Al by a thin hemispherical barrier layer. The formations of the AAO structure are illustrated in Figure 2-1.

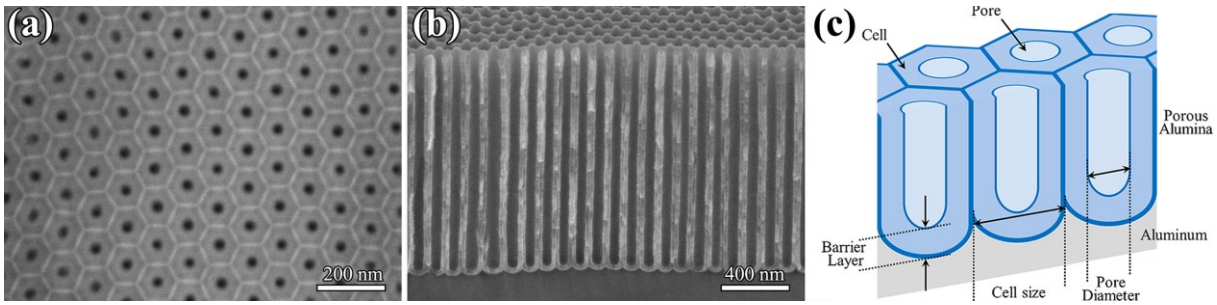

Figure 2–1. SEM images of anodic aluminum oxide template, top view (a) and cross-sectional view (b) of the template prepared in oxalic acid at 40 V. (c) Schematic diagram of AAO template.

The self-organized highly ordered nanopores of the AAO template are often defined by dimensional parameters such as the cell diameter (D_C), the pore diameter (D_P), the wall thickness (W_t), the barrier layer (B_L), and the interpore distances - the distance between the edges of two neighboring pores (d_S). The regularity of the pores is easy to control by varying the anodization conditions; the cell diameter can range from a few nanometers to hundreds of nanometers. Moreover, the depth of the cylindrical pores may exceed 200 μm and the high aspect ratio (2.5×10^4) and the high pore density (10^8 to 10^{11} cm^{-2}) are features which make the AAO template one of the most desirable non-lithographic techniques for the producing of nanostructure arrays.[70]

Generally, D_C and D_P are in linear proportion to the anodization potential (U) with the constants $\lambda_C = 2.5$ nm V^{-1}, $\lambda_P = 1.29$ nm V^{-1}, respectively:[71-73]

$$D_C = \lambda_C U \tag{2-1}$$

$$D_P = \lambda_P U \tag{2-2}$$

Keller et al. have found that D_C can be precisely calculated from the following equation:[64]

$$D_C = d_S + D_p = 2 W_t + D_P \tag{2-3}$$

The linear relationship between D_C and U is assumed on the hypothesis that D_P is independent of U. O'Sullivan and Wood found that the W_t is about 71% of the B_L. Accordingly, the following equation can be proposed:[71]

$$D_C = 1.42\ B_L + D_P \tag{2-4}$$

The experimental equations of aluminum anodization in oxalic acid have been calculated by Ebihara et al. to describe the relationship between D_C and U as:[74]

$$D_C = 14.5 + 2.00\ U \quad (U \leq 20\ V) \tag{2-5}$$

$$D_C = -1.7 + 2.81\ U \quad (U \geq 20\ V) \tag{2-6}$$

In addition to the features which arise naturally in the AAO template, the pore diameter and the interpore distance can be further adjusted by a widening process.[75]

The density of the pores of AAO template is one of the most significant features for fabrication of nanostructure arrays. Given that the pore density (P_d) is defined as the total number of pores occupying of 1 cm^2 surface area, the pore density for an AAO template can be expressed by:[73]

$$P_d = \frac{10^{14}}{P_h} = \frac{2\times10^{14}}{\sqrt{3}\times D_C^2} \tag{2-7}$$

in which P_h is a surface area of a single hexagonal cell. By substitution of the value of D_C from Eq. (2-1), the expression will be as follows:[73]

$$P_d = \frac{2\times10^{14}}{\sqrt{3}\times D_C^2} = 18.475 \times 10^{12} \times\ U^{-2} \tag{2-8}$$

This expression suggests that the anodization potential and the electrolyte (more details about acid and non-acid electrolytes are to be found in Table 2-1) are the only parameters that will influence the dimensional features of the AAO template. However, when these

factors were established as having an influence on the dimensional parameters of AAO template, the temperature of the anodization process was 20-25 ºC. Meanwhile, however, it has been found as an experimental fact that decreasing the temperature will increase the thickness of the barrier layer as well as the thickness of the pore wall, at the same time decreasing the pore diameter.[73, 76-78]

Table 2-1. Some of acid and non-acid electrolytes used to produce AAO templates.

Type	Electrolyte	Concentration (M)	D_P (nm)	Ref. No.
Acid	Acetic	1.0	Not reported	[79]
	Citric	0.1 – 2.0	90 – 250	[80, 81]
	Chromic	0.3, 0.44	17 – 100	[81, 82]
	Glycolic	1.3	35	[80]
	Malic	0.15 – 0.3	Not reported	[81, 83]
	Malonic	0.1 – 5.0	Not reported	[80, 84, 85]
	Oxalic	0.2 – 0.5	20 – 100	[36, 40, 69, 86-88]
	Phosphoric	0.04 – 1.1	30 – 400	[89-92]
	Sulfuric	0.18 – 2.5	12 – 100	[86, 93, 94]
	Tartaric	0.1 – 3.0	Not reported	[80, 81, 85]
Non-Acid	Ammonium Adipate	150g/L	6.4	[95]
	Sodium Borate	2.2	7	[96]
	Sodium chromate	0.1	10	[97]
	Sodium hydrogen phosphate	0.1	9.4	[97]
	Sodium hydroxide	0.01 – 0.1	Not reported	[98]
	Sodium sulfate	0.1	5.8	[97]
	Ammonium Adipate	150g/L	6.4	[95]
	Sodium Borate	2.2	7	[96]

2.3. Pore formation in the AAO template

Masuda et al. in 1995 synthesized a highly ordered AAO template by a two-step anodization process under constant potential.[99] To understand the pore structure formation, a typical current - time curve recorded during the anodization process under a constant potential starting from pure aluminum foil to realize the porous AAO as shown in Figure 2-2. Accordingly, the current-time curve includes four distinct regions (stages). In the initial stage (I), a thin solid aluminum oxide barrier starts to grow over the aluminum surface. As anodization time is increased, the thickness of the grown barrier (or resistance)

will increase to reach to the critical value, whereupon the current drops quickly to the minimum value (II).

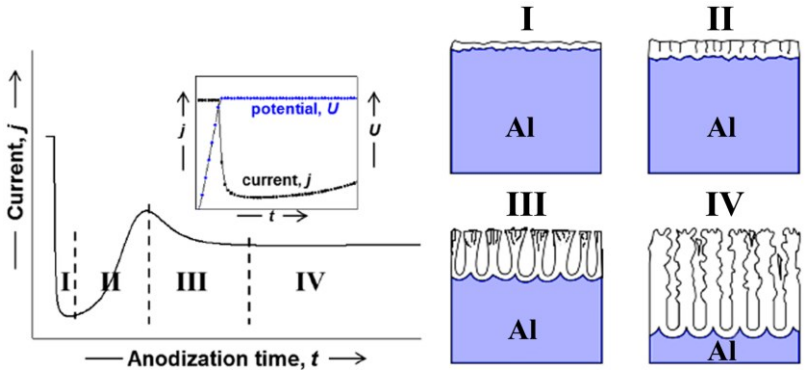

Figure 2–2. Current (j)-time (t) curves for a constant potential including the schematic diagram of the kinetics of porous AAO growth. (*Adapted from ref.* [76]).

It is at this stage that the onset of pore formation was observed. There have been several explanations, suggesting that the electrical charge passes through the local imperfections (e.g., impurity, defects, pits) resulting in the initiation of pore formation.[71, 100, 101] Continuing the anodization leads to an increase in current to the maximum value (III). Hereafter the current value becomes stable (IV) and the steady-state growth of porous alumina is observed.[102]

2.4. Steady-state growth of porous alumina

It is important to understand the chemical reactions during the steady-state growth of the pores; the following reactions dominate the anodization of the AAO in an acidic electrolyte.[37, 102-105]

1) Al^{3+} ions are formed at the interface of metal/oxide:

$$Al \Longrightarrow Al^{3+} + 3e^{-} \qquad (2\text{-}9)$$

2) At the base of the pore near the electrolyte/oxide interface, O^{2-} and H^{+} ions are produced by electrolysis of the water:

$$2H_2O \Longrightarrow 2O^{2-} + 4H^+ \quad (2\text{-}10)$$

3) The free O^{2-} ions migrate from the electrolyte/oxide interface to the metal/oxide interface and will react with Al^{3+} ions to form Al_2O_3:

$$2Al^{3+} + 3O^{2-} \Longrightarrow Al_2O_3 \quad (2\text{-}11)$$

4) When the electric-field is enhanced at the electrolyte/oxide interface, dissolute Al_2O_3 starts to form:

$$Al_2O_3 + 6H^+ \Longrightarrow 2Al^{3+}(aq) + 3H_2O \quad (2\text{-}12)$$

At this stage of the steady-state growth, there will be a balance between the electric-field-enhanced oxide dissolution at the electrolyte/oxide interface and the formation of oxide at the oxide/metal interface. This balance is an important factor in the formation of the pores of the AAO template, since the thickness of the barrier layer stabilizes in the entire anodization process and the result is steady-state pore propagation in the aluminum. Furthermore, the electric-field-enhanced dissolution itself separates the solid aluminum from the oxide barrier formed from non-porous alumina occurring in a neutral solution.[37] The dissolution process of the Al_2O_3 during anodization of a non-porous alumina prevents the continuous Al_2O_3 layer formation, as shown in Figure 2-3.

Despite the fact that the barrier type and non-porous type of Al_2O_3 layer are quite different in all physical characteristics, they are similar to each other in being linearly proportional to the applied anodization potential.[103]

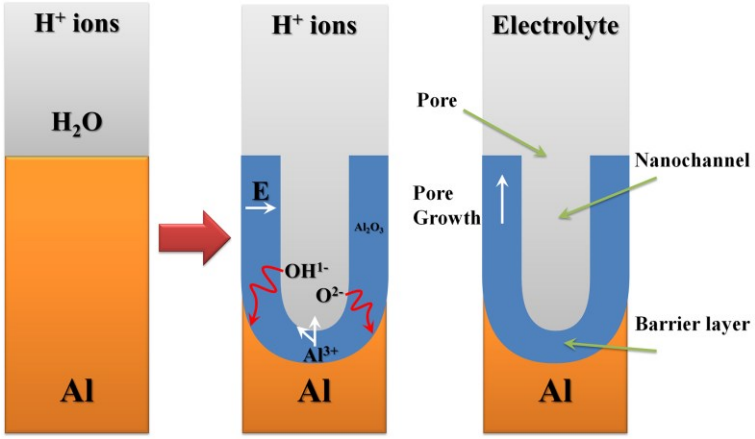

Figure 2–3. Schematic of the pore formation mechanism in an acidic electrolyte[105].

2.5. Regularity of the pores of AAO template

The highly ordered hexagonal pore arrays formed as the AAO template are a result of a self-organized process during the Al anodization.[106-108] Although the pores at the earlier stage are disordered on the top, there are regular pores at the bottom of the AAO template.[37] Masuda and Satoh suggested that a two-step anodization process can create a highly ordered pore.[65] This involves removing the first anodization from the Al foil, leaving a nanohollow array on the surface of the Al foil. [37] This highly ordered nanohollow array serves as a nucleation site for the development of a pore in the early stage of the second anodization, resulting in regular pore arrays from the second anodization.[87]

The time of the second anodization is a crucial factor to address the exact nanostructure type (i.e. nanowire and nanotube arrays or nanorod arrays or nanoparticle arrays), where the time of the second anodization is the only factor controlling the thickness of the anodic aluminum oxide. Accordingly, there are many reports of nanowire arrays and nanotube arrays prepared using anodic aluminum oxide as templates (called, in short AAO templates) or even using other materials to replicate the porosity of anodic alumina, this kind known as AAO template.[109-114] Because the nature of the barrier layer

on the back, it would have been more appropriate if the AAO template transferred directly on substrates to fabricate nanostructure arrays on substrates. Besides, the thinner AAO template could be utilized as a shadow mask to fabricate zero-dimensional nanomaterial (nanoparticles) on substrates, which has given the name of ultrathin alumina membrane.[42, 43, 115]

2.6. Ultrathin alumina membranes (UTAM)

Ultrathin alumina membranes (UTAMs) have been widely used as deposition or etching masks to pattern ordered arrays on the substrates surface.[116-119] through not until recently has the acronym UTAM been established. UTAMs with thickness of a few hundred nanometers or so can be attached or directly fabricated onto a substrate.[37, 42, 43, 120] A typical strategy to pattern nanostructure arrays on the surface of substrate can follow one of two main approaches:

2.6.1. Attached UTAM

Usually the transferring of the UTAM from the Al foils onto substrate is highly complicated because of its ultrathin and fragile nature. The schematic diagram in Figure 2-4 outlines the transferring processes of the attached UTAM (A-UTAM), with the following main steps:[37, 115, 121-123] 1) Polished high-purity Al foil at start(Figure 2-4a). 2) First anodization step, taking several hours (Figure 2-4b). 3) Removal of the first anodization (Figure 2-4c). 4) Second anodization, taking several minutes, to realize the UTAM layer (Figure 2-4d). 5) Using of a polymer (e.g. PMMA) on the top of the UTAM to support it (Figure 2-4e). 6) Removal of the Al and the B_L to form the open-hole UTAM (Figure 2-4f). 7) The UTAM with the supportive layer attached to the substrate (Figure 2-4g). 8) Finally,

removal of the supportive layer (Figure 2-4h). Typically, the thickness of the UTAMs made in this way is in the hundreds of nanometers (200-800 nm).

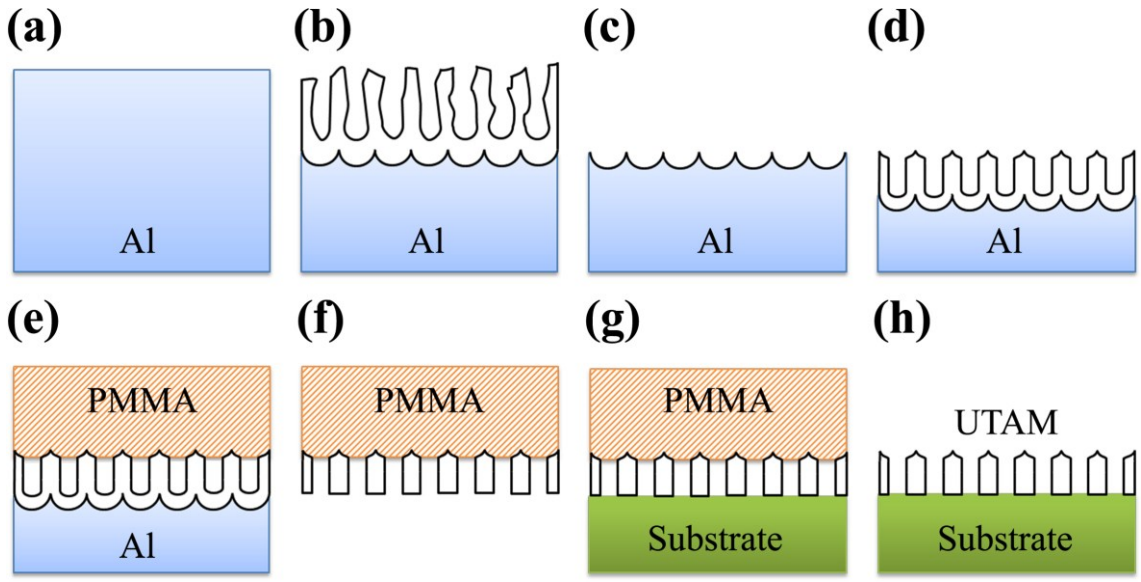

Figure 2–4. Schematic outline of the transferring processes of A-UTAM. (a) Aluminum foil; (b) first anodization; (c) removal of alumina; (d) second anodization; (e) polymerization of MMA; (f) removal of Al layer and barrier layer; (g) pore widening and mounting onto substrate; (h) removal of PMMA layer.[37]

Although this technique is effective to transfer an area of several millimeters of UTAM, the freestanding UTAMs are so fragile in nature that there is usually twisting, folding or cracking of UTAMs (Figure 2-5). Moreover, the process of the removing the supporting layer makes it very difficult to obtain a perfect and flat UTAM.

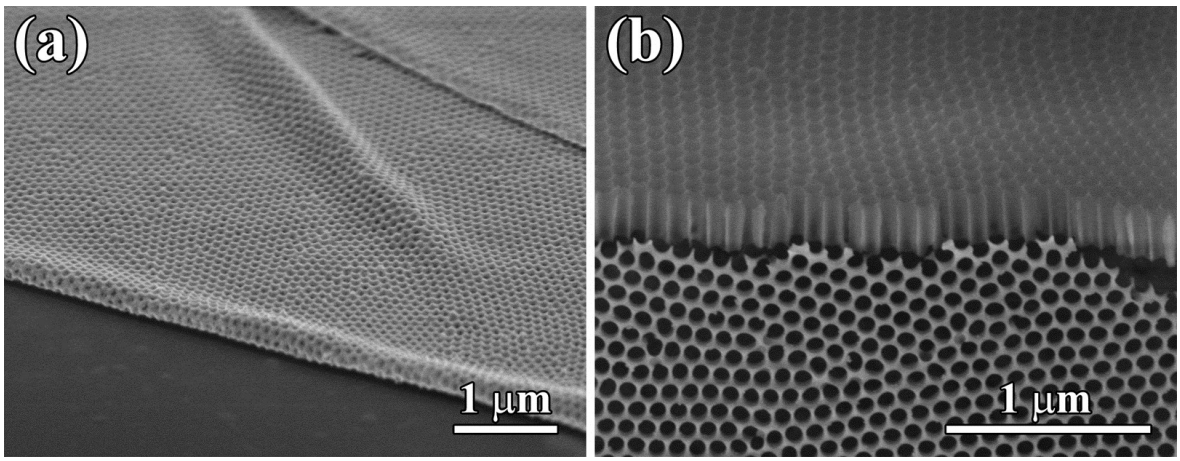

Figure 2–5. SEM images of the A-UTAM on Si substrate; folded and twisted UTAM (a), cracked UTAM (b).

2.6.2. Connected UTAM

Figure 2-6 outlines the fabrication procedures of the connected UTAM (C-UTAM). These procedures are: 1) deposition of the inter layer and high-purity Al on the surface of the substrate (Figure 2-6a). The inter layer (such as Ti) is to enhance the adhesion between the substrate and the Al layer.[37, 124] 2) Stabilization of the desired thickness of the Al layer (Figure 2-6b). 3) First anodization; duration depends on the desired thickness of the UTAM (Figure 2-6c). 4) Removal of the first anodization (Figure 2-6d). 4) Second anodization for the rest of the Al layer to realize the UTAM/substrate (Figure 2-6e). 5) Removal of the B_L of the UTAM, with the connected open-pore UTAM/substrate as the result (Figure 2-6f).

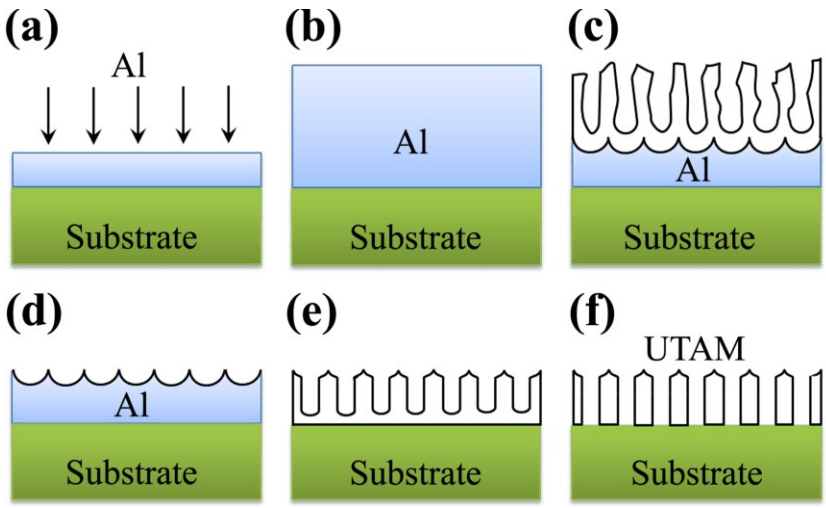

Figure 2–6. Schematic outline of the fabrication processes of C-UTAM. (a) Deposition of Al; (b) Al layer on substrate; (c) first anodization; (d) removal of alumina; (e) second anodization; (f) removal of barrier layer.[37]

Although the C-UTAM has some advantages, including the better adhesion of the UTAM than that in attached type and the fact that the C-UTAM can be formed over large scale to cover the substrate area at a depth of only a few nanometers, there are, nonetheless, many challenges facing the C-UTAM. As is well known, the thin film deposited by PVD methods has large scale defects overgrowing the metallic layer,[124-126] because of the high

energy of the atoms during the melting. There is thus larger defect nucleation and destruction at the deposition surface as well as the stress on the surface and the porosity.[124] In addition, the formation of the pores deviates from the vertical path in the Al thin film as a result of the random orientation of the grain crystallography as shown in Figure 2-7. These deficiencies lead to a C-UTAM with lower regularity of nanopores than an A-UTAM will have, especially in the case of a thicker UTAM, (≥ 200 nm). Besides, it is hard to say that the B_L has been completely removed by the wet-etching processes.[22, 127]

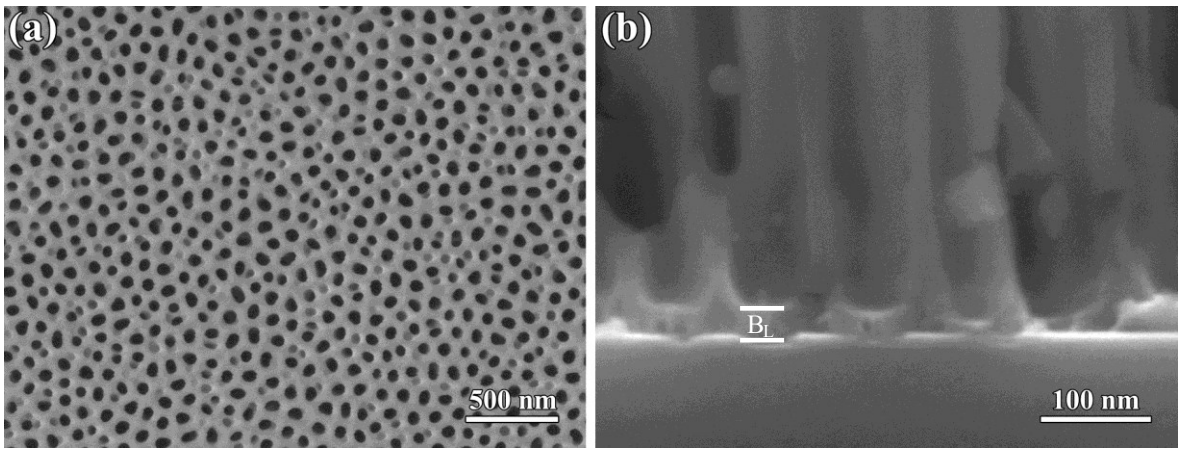

Figure 2–7. SEM images of the C-UTAM on Si substrate showing the irregularity formation of the pores (a) and B_L (b) obstacles.

2.7. UTAM combined with atomic layer deposition

There are several methods which can produce varied nanostructure arrays (nanoparticle, nanowire, nanopillar, nanoholes, and nanotube, et al.) by using either type, A-UTAM or C-UTAM (see Table 2-2). Such kinds of template can yield perfect nanostructure arrays with an adjustable pore diameter and interpore distances. There are advantages to UTAMs compared with other lithographic and nonlithographic methods (e.g. electron beam, self-assembly, scanning probe, et al.),[128-131] which have their various inherent limitations. These limitations include low pattern area, high equipment costs in the case of electron beam lithography (EBL) methods; poor control and materials limitation in

the case of self-assembly processes; and lengthy time for scanning probe microscopy (SPM) techniques.[37] In contrast, the UTAM method can produce various nanostructure arrays cost- and time-effectively.

Table 2-2. Summary of the researches in the UTAM nanopatterning. (Source: ISI Web of Science, status January 2006 – December 2015).

UTAM	Nanostructure (substrates)	Fabrication method	Features and applications
A	Ag NRs and Pd NCs	EBE	Nanostructuring on substrate[39]
−	Pt NDs, Au NTs and SiC nanopores	ECD and H_2 etching	Replication[132, 133]
−	Fe NRs	SP	Nanostructuring on substrate[134]
C	Ni_3S_2 NTs and NiS_2 NTs	Self-assembly	Ferromagnetism characteristics[135]
−	Carbon NTs	Pyrolysis of Ferrocene	Electrical properties[136]
−	GaN nanopores and NDs	MOCVD and ICP	Nanostructuring on substrate[137]
C	Ni and Au NDs	PVD and IM	Nanostructuring[138]
C	Ag NWs	ECD	Crystal structure[139]
C	Pd (Si) nanopores	SP	H_2 sensing properties[140]
C	Ni, Ag and Au nanotips	EBE	Electrochemical characterization[141]
−	Polyaniline-Au NTs	EBE	Metal-organic contact[142]
A	Ni nanopores	EP and SP	Multistage nanopore structure[143]
A	Ag nanoparticles	ELP	UV illumination[144]
A	Bowl-like ZnO nanostructures	Solvent-thermal	PL[145]
−	Pt NTs	Polymeric-wetting process	Semiconductor capacitors[146]
A	$Ba_xSr_{1-x}TiO_3$ (Si) NDs	RIE and SC	Nanostructuring[147]
C	Au nanorods and NDs	ECD	Nanostructuring[148]
A	Prepatterning AAO template	FIB	Perfectly ordered nanopores[149]
C	Carbon NTs	CVD	Template-assisted growth[150]
C	Ni and Ni/Cu (Si) NDs	TE	Magnetic hysteresis analysis[151]
−	Pt, Au and Pt-Ru nanopores	PLD	Electrochemical characterization[152]
C	Si and micro/nanofluidic channel	TE and RIE	Nanostructuring[153]
C	UTAM on ($Nb/SiO_x/Si$) substrate	SP and TE	Cathodic polarization[154]
C	Nanopores channel	SP	Magnetic recording media[155]
−	$Bi_{3.25}La_{0.75}Ti_3O_{12}$ NTs	ELP	3D ferroelectric nanotube capacitors[156]
C	Pt (Si) NWs	ECD	Ferroelectric switching characterization[157]
C	Au (Si) NWs	TE, ECD and ALD	Electrochemical characterization[158]
A	Si nanopatterned	RIE	PL[159]

UTAM	Nanostructure (substrates)	Fabrication method	Features and applications
A	Ag (Si) nanoparticles	TE	Plasmonic photovoltaics[160]
A	$Pb(Zr_{0.20}Ti_{0.80})O_3$ NDs	PLD	Nanocapacitor[161]
C	SiO_2 (Si) nanopores	EBE and RIE	p–n junction[162]
A	Si NWs	RIE, SP and MaCE	Nanostructuring[163]
C	ZnO on Si nanopores	SP and RIE	PL[164]
A	ZnO nanorod, Si nanopores	ICP, SP and microwave irradiation	Nanostructuring[165]
A	Ni (Si) NDs	TE	Nanomechanical behavior[166]
C	Ni (ITO) NDs	EBE and ECD	Nanostructuring[167]
C	Nanowell	TE	H_2 sensors[115]
–	Silica nanoporous	Wetting process	Replication process[114]
A	TiO_2 NTs	ALD	Absorption behaviors[168]
–	BiSb NTs	ECD	Nanostructuring[169]
C	Ni NWs	ECD	Nanostructuring[170]
A	$CoFe_2O_4$ NDs	PLD	Magnetic hysteresis analysis[171]
A	$Pb(Zr_{0.2}Ti_{0.8})O_3$ NDs	PLD	Ferromagnetism characteristics[172]
A	Si NWs	CVD and MaCE	Nanostructuring[173]
C	Si/Ge NWs	MBE, RIE, SP and MaCE	Nanoheterostructures[174]
C	Au NRs and NDs	SP	Nanostructuring[175]
A	Si nanopores	RIE	PL[176]
–	Ru, Co nanorods	ALD	Nanostructuring[177]
A	Si NWs	TE and CVD	Nanostructuring[178]
A	PDMS NP	SC	UV-nanoimprint lithography[179]
A	Si NWs	MaCE	Nanostructuring[180]
A	Large area UTAM	polymer support	Nanostructuring[181]
A	Nanoporous	–	Optical nonlinearity[182]
C	surface grafted of Poly(γ-benzyl-L-glutamate)	Polymerization	Optical spectroscopy[183]
C	polymeric NPs	Polymerization	Nanostructuring[184]
C	Nano-master	–	Anti-reflection effect[185]
A	Au NDs	TE	Quantum dots[115]
A	Si NWs	MaCE	Size tuning[186]
A	$Pb(Zr,Ti)O_3/CoFe_2O_4$ NDs	PLD	Ferromagnetism characteristics[187]
C	Si porous	SP and RIE	Hybrid solar cells[188]
C	Au nanopores	EBE	Surface-enhanced Raman spectroscopy[189]
C	Si NWs	TE and MaCE	Size tuning[190]
A	Semiconducting polymeric nanorods	SC	Optical and Electrochemical characterization[191]
–	PMMA mold	–	Gas sensor[192]
C	G4 Polyelectrolyte nanopores	Polymerization	Surface plasmon resonance and optical waveguide spectroscopy[193]
–	ZnO nanorods	SP and ECD	Nanostructuring[194]
C	Al_2O_3 NCs (AlN, Sapphire)	SP	Moth-eye nanostructures[195]
A	Semiconducting polymeric NPs	SC	Conductivity analyzing[196]

UTAM	Nanostructure (substrates)	Fabrication method	Features and applications
C	Pt (C/Si NCs) nanoparticles	TE, SP, RiE and CVD	Physico-chemical characterization[197]
C	Au nanowire	ECD	Diameter-modulated[198]
C	Al_2O_3 (Si, glass) nanopores	SP	Nanostructuring[199]
C	Pt porous	CVD, RIE and SP	Fuel cells[200]
A	c-Si NDs	PLD	Raman spectroscopy[123]
A	Au/Ag NM and Si NWS	SP and MaCE	Nanostructuring[201]
C	Si nanopores	EBE and RIE	Tunable photon trapping[202]
C	Si porous	RIE	PN junction substrate[203]
C	Ni (Si) NWs	SP, RIE and ECD	Magnetism characteristics[204]
C	Surface pattern	TE, EBE	Reflectance effect[205]
A	$BaTiO_3/CoFe_2O_4$ ($SrTiO_3$) NDs	PLD	Magnetoelectric nanocomposite[206]
–	Au, Cu, Ni, Ag, Pt, Al, and Ti NDs	IM and wet etching	Contact-printed[207]
A	Au NM and Si NWs	SP and MaCE	Nanostructuring[208]
–	Polymeric NPs	Polymerization	Adhesion properties[209]
–	Ag/UTAM	ECD	Surface-enhanced Raman spectroscopy[210]
C	Al_2O_3 nanopores	EBE	Pre-oxidation patterning[211]
A	Co implanted	TE and II	Nanopatterning[212]
A	Au/HfO_2 NDs	SP	Resistive switching memory[213]
C	AZO/Al_2O_3/AZO NWs	TE and ALD	Nanocapacitor[214]
C	Si NWs	TE, SP and MaCE	p-n diode[215]
A	Al_2O_3 (Si) nanopores	RIE, EBE and SC	Hexagonally or tetragonally nanopore arrays[216]
A	Graphene NM	SC, microwave and O_2 plasma etching	Field-effect transistors[217]
A	Ag (ITO)	TE	Optical characterization[218]
A	SiC nanopores andTiO_2 NTs	RIE and ECD	3D nanostructuring[219]
C	Ag NTs, NP and NWs	ECD	Surface plasmon resonance[220]
A	Ag (ITO) NDs	EBE	Surface plasmon resonance[221]
–	Ni and Ni/Pt NWs	EP and ECD	Resistive switching memory[222]
C	SiC/AlSiC NWs	PVD, CVD	Core-shell nanostructuring[223]
A	Polymeric nanotubes	SP and polymerization	Nanostructuring[224]
C	$Si_{1-x}Ge_x$ NDs and NWs	TE, RIE and CVD	Nanostructuring[225]
C	Co/Cu/Co (Si) NWs	TE and EP	Magnetic sensor[226]
–	ZnO NTs	Sol–gel	Nanostructuring[227]
A	Au, Ag (ITO) NDs	TE	Surface-enhanced Raman scattering[228]
A	Au NM and Si NWs	SP and MaCE	Nanostructuring[229]
A	Ag NDs	EBE	Surface plasmon resonance[230]
C	Au NDs, ZnSe and ZnO nanorods and NWs	SP and VLS	Nanostructuring[231]
A	Co, Pt and Co/Pt (Si_3N_4) implanted	TE and II	Nanostructuring[232]
A	GaAs nanopore	CVD and RIE	Solar cell[233]

UTAM	Nanostructure (substrates)	Fabrication method	Features and applications
A	$BiFeO_3$ ($SrRuO_3$/$SrTiO_3$) NDs	PLD	Resistive switching[234]
C	Al_2O_3 nanopores	SP	H_2 sensor[235]
–	TiO_2 NTs	ALD	Crystallization[236]
A	Ni (GaAs) NPs	ECD	Nanostructuring[237]
C	Sub-wavelength structures	Polymerization	Anti-reflection and self-cleaning
C	UTAM	TE and RIE	Anodization on an insulating substrate[238]
C	Poly(3-hexylthiophene) NPs	SC and pressing	Nanoimprinting[239]
C	Ag (Si, Ag) NDs	TE and SC	Optical characterization[240]
A	Pt (SiO_2, glass) NM	SP and SC	Surface plasmon resonance[241]
–	AuCr bimetallic nanorods	SP, ECD and TE	Conductivity and relaxation characteristics[242]
C	UTAM (Si)	TE	Integrated sensors[243]
A	Ag and $La_{1-x}Sr_xMnO_3$ ($Pt/Ti/SiO_2/Si$) NDs	SP	Resistive switching memory[244]
A	Au and Ag (Si, ITO) NDs	EBE	Nanoimprinting[20]
A	Cr (Si) NDs	TE	Nanoimprinting[121]
A	Au NDs/Ag nanohemisphere	SP	3D urchin-like nanodot arrays[245]
A	ZnO nanotubular	SC and ALD	Nanoimprinting[246]
A	Au/Ag NDs	ECD and RIE	Core-shell nanostructuring[247]
A	Ag (Si) NDs	SC and TE	Optical characterization[248]
C	Au NM	TE	Plasmonic nanostructure[249]
A	Au/Ag NDs	–	Optical characterization[250]
A	Ag NDs	RIE	Surface-enhanced Raman spectroscopy[251]
C	Al_2O_3 (TiN/Si) nanopores	PVD	Nanostructuring[252]
C	Ag Nanostructure	EBE	Surface-enhanced Raman spectroscopy[253]
C	Si NWs	TE, RIE and MaCE	Nanostructuring[254]
–	SnO_2/MnO_2 NTs	ALD and ECD	Supercapacitors[255]
A	Au (Si) NDs	PVD	Surface-enhanced Raman spectroscopy[256]
A	Ni/Au (Si) hybrid NDs	EBE	Surface-enhanced Raman spectroscopy[257]
A	Ag (Si) NDs	TE	Surface-enhanced Raman spectroscopy[258]
A	Au (Si) NDs, Au (Si) nanomesh and Si NWs	IM, EBE	Wafer-scale nanopattern[87]
C	Cu (Si) nanorods	EBE and ECD	Influence of wet etching time[259]
A	Graphene nanopattern	TCV, CVD and plasma etching	High optical transparency graphene[260,261]
C	ZnO (ITO) nanorods	SP and hydrothermal	Electrical and chemical characteristics[262]
A	Ag (TiO_2/Si) NDs	EBE	Plasmonic photovoltaics[263]
A	UTAM		Morphologies and optical characterization[264]
A	$Pb(Zr_{0.52}Ti_{0.48})O_3$ NDs	Sol-gel and SC	Piezoresponse properties[265]
A	Si nanopores	Plasma etching	Nanostructuring[122]

UTAM	Nanostructure (substrates)	Fabrication method	Features and applications
A	Ag (Quartz) NDs	Plasma etching, SC and TE	Hierarchical UTAM[266]
A	$Y_3Fe_5O_{12}$ ($Ga_3Gd_5O_{12}$) NDs	PLD	Magnetic hysteresis analysis[267]
A	$Y_3Fe_5O_{12}$ (Si) NDs	PLD	Magnetic hysteresis analysis[268]
A	$BiFeO_3/SrRuO_3$ ($SrTiO_3$) NDs		Resistive switching in nanocapacitor[269]
A	Si NWs	RIE and CVD	Enhanced light trapping[270]
C	UTAM (paper)	TE	Humidity sensors[271]
A	Ag NDs	TE	Glucose detection[272]
A	$BiFeO_3/CoFe_2O_4/SrRuO_3$ ($SrTiO_3$) NDs	PLD	Magnetic hysteresis analysis[273]
C	GaN NPs	CVD, EBE and RIE	Multiple-quantum-well[274]
A	Ag, Au/TiO_2 (ITO) NDs	EBE and ALD	Plasmonic-metal semiconductor nanostructures[31]
C	CdS-CdTe (ITO) NWs	TE and ECD	Solar cells[275]
–	Au, Ag, Pt, Ni, Pd NRs and Au-Ni-Pt NTs	ECD	Plasmonic nanostructure[276]
A	Acrylonitrile-Butadiene-Styrene nanostructures	Polymerization	Biofilm development[277]
A	Graphene NDs and Si NPs	CVD, plasma etching	Graphene assisted chemical etching[278]

Abbreviations: A = A-UTAMs; C = C-UTAMs; CNT = carbon nanotube; NT = nanotube; NP = nanopillar; NW = nanowire; NR = nanoring; ND = nanodot; NS = nano-sphere; NM = nanomesh; NC = nanocones; EBE = E-beam evaporation; VE = vacuum evaporation; TE = thermal evaporation; SP = sputtering; MBE = molecular beam epitaxy; PLD = pulsed laser deposition; IM = ion milling; RIE = reactive ion etching; PE = plasma etching; II = ion implantation; EP = electroplating; ELP = electroless plating; ECD = electrochemical deposition; VLS = vapor–liquid–solid; MOCVD = metalorganic chemical vapor deposition; PVD = physical vapor deposition; TCV = thermal chemical vapor; FAB = fast atom beam; FIB = focused ion beam; SC = spin coating; MaCE = metal-assisted chemical etching; ALD = atomic layer deposition

It should be mentioned that the preparation of nanostructures using the UTAM requires highly controllable deposition techniques (on the atomic scale) to synthesize the precise dimensions of the nanostructures. Each type of nanostructure (including nanoparticles, nanowires, and nanotubes) can be grown through UTAMs if a precise deposition technique is employed; e.g. a typical nanoparticle array has been prepared using PVD, nanowire arrays have been prepared using wet-chemical processes (electrochemical or electroless depositions) and most nanotube arrays are prepared using non-line-of-sight vapor-phase deposition processes such as atomic layer deposition and microwave plasma enhanced chemical vapor deposition (PECVD).[279-281]

The credit for atomic layer deposition (ALD) as a monolayer coating technique goes mainly to Tuomo Suntola who established it in August 1974 as atomic layer epitaxy (ALE).[282] Commercially, F-120 sold by Microchemistry in 1988 was the first ALE device; the first series of ALD was sold in 2001. ALD has materialized as a significant technique for thin film deposition with precise thickness control (~Angstrom), ALD has excellent conformality and homogeneity, even on complicated 3-D substrates with high aspect ratio.[70, 283, 284] To date, a wide range of materials has been grown by ALD including metals, semiconductors and insulators.[285, 286]

Generally, the ALD process is based on binary reactions as well as chemical vapor deposition (CVD). In CVD, two reactants are presented at the same time to form the thin film constantly on the substrate. For ALD, the reactants (precursor materials) hit the substrate individually and each reaction occurs between the substrate surface and reactant with precision and in a self-limiting manner.[283, 287-289] After each reaction, the unreacted material purges to start the second surface reaction with the other reactant. The schematic outline in Figure 2-8 shows the steps in each ALD cycle.

It should be mentioned that recently developed analytical methods such as transmission electron microscopy (TEM) and field emission scanning electron microscopy (FE-SEM) for the study of the morphology of the nanostructures have enabled the nanostructure directed AAO template technology to leap forward so that it is now a major technology (~ 10%) in the nanotechnology field. Figure 2-9 shows the expansion in the past 60 years of the number of articles published on the AAO template. In it, the articles combining ALD with the AAO template are distinguished.

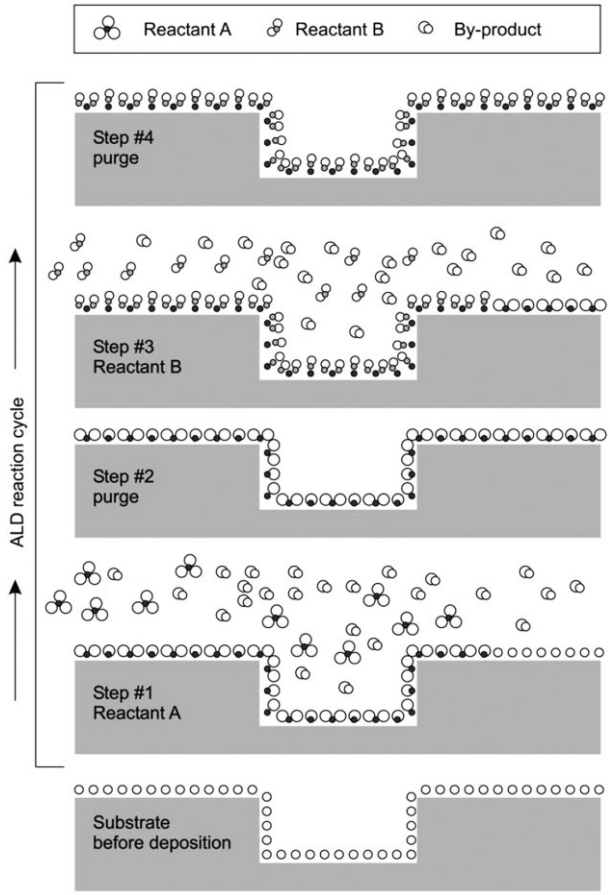

Figure 2–8. Schematic outline of the ALD cycle, Step 1: pulse of the reactant A leading to its absorption on the surface. Step 2: purge of the unreacted precursor A and of the byproducts. Step 3: pulse of the reactant B, which react with the surface species created by precursor A. Step 4: purge of the unreacted precursor B and of the byproducts. (*Adapted from ref.*[288]).

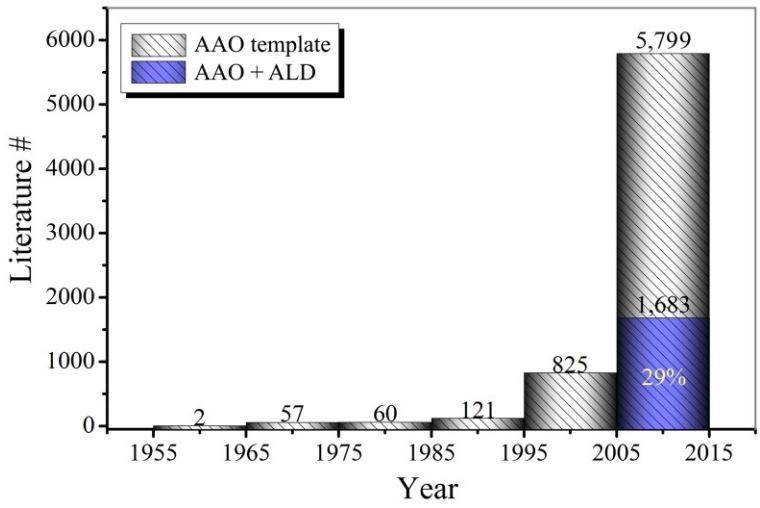

Figure 2–9. Evaluation of the articles published on AAO template, the blue column is the related articles combined the AAO template with ALD. (Source: ISI Web of Science, status end December 2015).

2.1. TiO_2 nanotube arrays by atomic layer deposition

In 1967, Shevjakov et al. described the ALD of TiO_2 using $TiCl_4$ and H_2O precursors,[290] and from that time on $TiCl_4$ has become the most common precursor used.[291-295] However, many other precursors have been successfully used to grow TiO_2 (see Table 2-3). TNTs have been prepared by using AAO and ALD in combination to enhance the wall thickness of the TNT.

Table 2-3. Some of the main reactants for TiO_2 deposition using ALD processes.

Reactant A	Reactant B	Ref. No.
TiCl4	H2O	[31, 295-300]
TiCl4	H2O2	[301-304]
TiCl4	MeOH	[305]
TiCl4	O2	[294, 306]
TiF4	H2O	[307]
TiI4	H2O	[308-310]
TiI4	H2O2	[311-313]
TiI4	O2	[314]
Ti(NMe2)4	H2O	[315, 316]
Ti(NMe2)2	H2O	[317]
Ti(OMe)4	H2O	[287, 318-320]
Ti(OEt)4	H2O	[321, 322]
Ti(OEt)4	H2O2	[323, 324]
Ti(O*i*Pr)4	H2O	[325-327]
Ti(O*i*Pr)4	H2O	[328, 329]
Ti(O*i*Pr)2(dmae)2	H2O	[330]
Ti(O*i*Pr)3(N*i*Pr-amd)	H2O	[317]
TiCp2((iPrN)2C(NHiPr))	Not required	[331]
Ti(CpMe5)(OMe)3	O2	[332]
Ti(CpMe5)(OMe)3	O3	[333, 334]

2.8. TiO_2 nanotube arrays for solar water splitting

Photoelectrochemistry was started in 1955 by Brattain and Garrett when they studied the interface between germanium and an electrolyte,[335] and has since grown substantially with much other work.[336-338] In 1972 Fujishima and Honda reported the photoanode

activities of TiO_2,[339] Since then, many instances of semiconductor photocatalysis have been intensively studied.[340-342] In 1978 Nozik expected that it would be possible to optimize the basic reaction of a photoelectrosynthetic cell by means of micro- or nanoscale particles that would split water under illumination.[343] Three basic configurations of photocatalytic systems have been proposed. The first is a Schottky junction type, in which a metal-semiconductor junction can absorb more light than a semiconductor alone.[53, 61, 344] The second configuration is a plasmonic effect type; in this system, the direct advantage is to extend the light absorption range in a wide bandgap semiconductor for better charge generation.[345, 346] The third configuration is a semiconductor–semiconductor junction (Z-scheme) system, with two bandgaps the light absorption range of the photoanode is rarely extended to harvest high photogenerated charges.[53, 54]

Generally, a single semiconductor material with a wide bandgap (e.g. TiO_2), conduction band energy and valence band energy can efficiently split water into H_2 and O_2 using photogenerated electrons and holes under illumination.[61, 62] To develop a new photocatalytic system, there are three crucial factors affecting the water splitting performance: 1) A single semiconductor may not offer efficient photocatalytic activities due to the large-bandgap, which can only absorb light in ultraviolet region. 2) To reduce the recombination between the electrons and holes, the charge must be transported in a straight path. 3) Some semiconductor surfaces have low ability for redox reactions at the semiconductor-electrolyte interface; also, the charge mobility in bulk semiconductors will reduce the efficiency of water oxidation.[44, 54]

In order to resolve these problems, nanostructured materials increase the quantum efficiency for water splitting by reducing the recombination states through decreasing the diffusion distance for the minority carrier. In 1-D nanostructures (i. e. nanowire and nanotube arrays), the directions of light absorption and charge carrier collection can be

decoupled through the planar geometries.[296, 347, 348] In addition, the crystal facet of the semiconductor also improves the photocatalysis. If the semiconductor has a single facet, the electron will be directly transferred into single electronic state.[54, 349] On the other hand, heterogeneous photoelectrodes can realize highly efficient solar water splitting. This is because a large solid-solid contact interface promotes the photogenerated electrons from the conduction band of photocatalyst I and holes from the valence band of photocatalyst II, and meantime should facilitate the balanced distribution of incident photons between photocatalyst I and photocatalyst II to maximize the utilization efficiency of solar light.[44-47] Accordingly, two factors will determine the performance of heterogeneous photoelectrodes for solar energy conversion, the components and the configuration. The two components for constructing heterogeneous photoelectrodes must have well-matched energy levels to form the dual bandgap configuration that allows the photogenerated charge carriers in the semiconductors to recombine at the interface. The result will be higher theoretical energy conversion efficiency than a single bandgap configuration achieves. Where the configuration of heterogeneous photoelectrodes is concerned, this is always considered to have significant effect on light harvesting and charge separation, and consequently on the photocatalytic efficiency.[48-50]

2.9. Mechanism and structure of Photoelectrochemical water splitting

Ideally, if the bandgap energy (E_g) of the single semiconductor is large enough and the edges of conduction band energy (CB) and valence band energy (VB) are near enough to the electrochemical potentials E° (H^+/H_2) and E° (O_2/H_2O), the semiconductor can drive the hydrogen and oxygen by using electrons/holes generated under illumination.[61] The simplest photoelectrolysis reaction can be described by the equation:[53, 61]

$$H_2O \Longrightarrow \frac{1}{2}O_2 + H_2;\ \Delta G = +237.2\ \text{kJ mol}^{-1} \quad (2\text{-}13)$$

where ΔG is the free energy change for one molecule of H_2O converted to H_2 and 1/2 O_2. Unfortunately, there is no any single semiconductor material that can satisfy all these requirements (a suitable bandgap energy for efficient solar energy absorption and at the same time the band-edges aligned with both the H_2 and O_2 redox potential of water).[53]

Basic PEC water splitting can be formed by using a single p-type or n-type semiconductor. As a single bandgap device, the semiconductors require a 1.6 – 1.7 eV bandgap to generate the open-circuit voltage (V_{oc}) to split the water, according to catalysis mechanisms which have been calculated for a bandgap above 2 eV.[350] A dual bandgap device (two connected semiconductors) can achieve efficient water splitting because it enhances the light harvesting ability of PEC electrode (photoanode, cathode or photoanode/cathode).[350, 351].

Figure 2-10 illustrates the basic structures with a single n-type semiconductor. The required photon energy (hν) to photogenerate an electron-hole pair depends on the E_g of the semiconductor and only photons with ($h\nu \geq E_g$) can be absorbed by the semiconductor. As shown Figure 2-10, it has been possible to excite the electrons in the VB to the CB, leaving holes in the VB and generating electron-hole pairs. Once the pairs transfer to the surface of semiconductor, the redox reactions can occur. The electrons in the conduction band initiate the reduction reaction with acceptors (A), and the holes in the valence band contribute in the oxidation reactions with donors (D). The reduction and oxidation ability of electron and hole photogeneration in the semiconductor are determined by the positions of the CB and VB edges. Only when the energy levels of the edge of conduction band (E_c) and the edge of valence band (E_v) of the semiconductor are lower and higher than the reduction redox potential and oxidation half reactions, respectively, can the total photocatalytic reaction occur.[352] In the case where the band edges do not fulfill the requirement, one of the electron acceptors or donors will be lost, to continue with the half

reaction. If the reactions pass to the surface, the charge consumption rates are still highly affected by the differences between the position of the band edges and the redox potential levels, without considering the band-bending at semiconductor-electrolyte interface.[54]

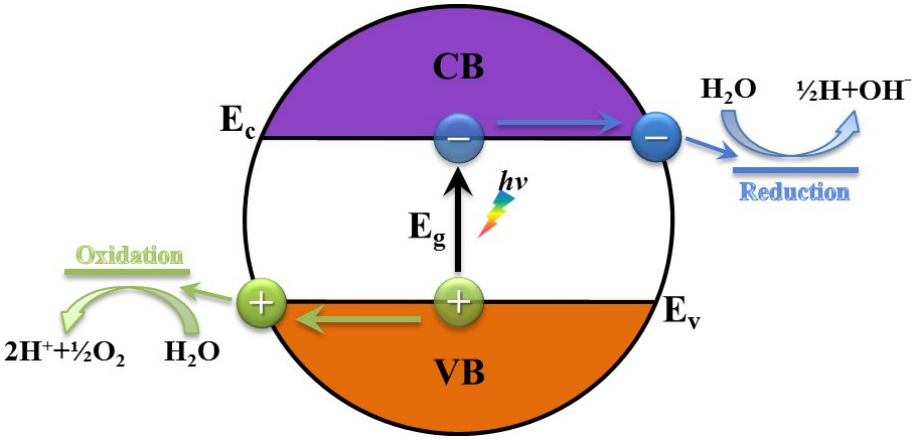

Figure 2–10. Schematic illustration the basic mechanism of a single semiconductor photocatalytic process.

The basic PEC system contains an n-type semiconductor and a metal counter electrode, with an electrolyte between them (Figure 2-11a). The system also includes a reference electrode with a known electrode potential. By measuring the difference between the semiconductor potential and the reference electrode potential, the reduction or oxidation power of the semiconductor electrode can be identified. The Fermi level (E_f) of the electrolyte (E_{redox}), of the semiconductor and of the metal will be kept in an equilibrium state (Figure 2-11b). Because there are two redox couples in the electrolyte, the E_{redox} of the electrolyte will be between the potentials of the redox couples and will depend on the relative concentrations of oxidation and reduction products in the electrolyte. Basically, for the n-type semiconductor with $E_f \geq E_{redox}$, the semiconductor surface bends upward due to the charge redistribution, forming a layer of charge space on the semiconductor side.[52] Once the light excites the semiconductor, the internal electric field formed in the charge space layer will separate the photogenerated holes and electrons. These electrons will drift to the counter electrode through conducting wires, while the holes transfer toward the

electrolyte. Accordingly, the internal photovoltage will be formed, and the E_f levels of the metal and the semiconductor will bend upward to form a quasi-Fermi level (E_f^*) of the semiconductor. When the E_f^* becomes higher than the reduction of half reaction potential, the holes on the semiconductor and electrons on the counter electrode can contribute to the reduction and the oxidation reactions, respectively (Figure 2-11c). This condition is fixed for the n-type semiconductor with a large band gap, whose flat-band potential ($U_{f\text{-}b}$) is higher than the reduction potential of the electrolyte. The $U_{f\text{-}b}$ is the minimum potential applied to the semiconductor to reduce the band-bending to zero (Figure 2-11d).[54]

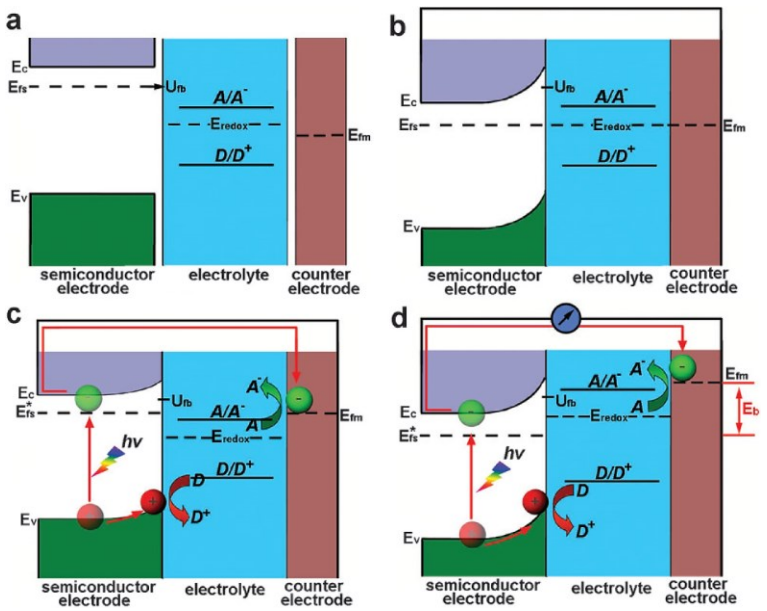

Figure 2–11. Schematic band diagrams illustrating PEC processes: (a) before contact for an n-type semiconductor; (b) after contact for an n-type semiconductor in the dark; (c) n-type semiconductor under light irradiation without external bias; (d) n-type semiconductor under light irradiation with external bias. (*Adapted from ref.*[54])

3. Transferring of Wafer-Scale UTAM onto Si Substrate

3.1. Introduction

In this chapter, a facile method is developed, where highly ordered UTAMs over wafer-scale (4-inch) can be transferred onto substrates without any twisting, folding, cracking of UTAMs, as well as no contamination to the substrate. The treatment of the UTAM surface and reasonably fixing the UTAM onto the substrate before the removal of backside Al foil are essential to transfer large scale UTAMs successively. By using the transferred UTAMs as templates, various nanostructuring patterns were achieved over wafer scale, including nanoparticle, nanopore (nanomesh) and nanowire arrays with tunable and uniform dimension. Technically, there is no limit for the size of UTAM and no required prerequisites for UTAMs, substrates and the materials of the UTAM-prepared nanostructures (metals, insulators and semiconductors can be patterned), which will extremely extend the application of highly ordered nanostructure arrays. It should be noted that this method also can be used to prepare nanostructures with other symmetries in addition to hexagonal arrays, after prepatterning the Al surface prior to the anodization process. [14, 20, 31, 353]

3.2. Experimental

3.2.1. UTAM Preparation

Self-ordered nanoporous UTAM was prepared by two-step anodization of high purity Al foil (99.999%) under a potential of 40 V in 0.3 M oxalic acid at 7 ºC. Before anodization, the foil was degreased in acetone, ethanol and rinsed by deionized (DI) water, and then electrochemically polished under a potential of 30 V at 0 ºC in a mixed solution

contain ($HClO_4$:C_2H_5OH, v:v = 1:7) with a constant stirring for 2-3 min. Two-step anodization was carried out in lab-made cell which can hold a 4-inch (Figure 3-1). Al foil. After removing the irregular nanopores obtained by 7 h first anodization (using 6 wt % H_3PO_4 + 1.8 wt % H_2CrO_4 at 60 ºC for 8 h), highly ordered nanohollow arrays are left on the top surface of the Al foil. These hollows were adopted as a template for the second anodization, which was carried under the same conditions but using different anodization time (1-8 min) to prepare different thicknesses of UTAMs. The pore diameter of UTAM was tuned by using 5 wt % H_3PO_4 at 30 ºC in different time (5-45 min). Then the surface of UTAM was smoothed by using Ar ion milling for 5 min to remove the sharp edges of the nanopores, which can improve the adhesion between the UTAM and the substrate.

3.2.2. UTAM Transferring

The prepared UTAM was transferred onto a standard 4-inch p-Si (100) wafer. In order to improve the adhesion between the UTAM and Si substrate, the wafer was cleaned by Piranha solution (H_2SO_4:H_2O_2, v/v = 3/1) and HF (2%) for 30 and 5 min, respectively, and then thoroughly rinsed by DI water. As showing in Figure 3-1, the UTAM was transferred onto Si wafer by using the same cell unit that was used for anodization, keeping UTAM side connected with the substrate. To get better adhesion, several drops of DI water were dropped between the UTAM and the substrate before placing the UTAM. Finally, the backside Al and the barrier layer of UTAM were completely removed by using aqueous $CuCl_2$ and 5 wt % H_3PO_4, respectively.

3.2.3. Au Nanomesh Fabrication

About 20 nm Au was deposited (deposition rate of 0.2 Å/s) onto the top surface of the UTAM (wafer scale) by electron-beam deposition before removal of the backside Al and

the barrier layer. The sharp edges on the surface of the prepared UTAM also were smoothed by using argon ion milling to get a smooth and a uniform UTAM. Then the Au nanomesh was transferred onto the substrate according to the similar step of the transferring of UTAM, followed by 2 s etching in a mixed solution of ($HF:H_2O_2:H_2O$, v/v/v = 50/25/175) to remove the UTAM completely.

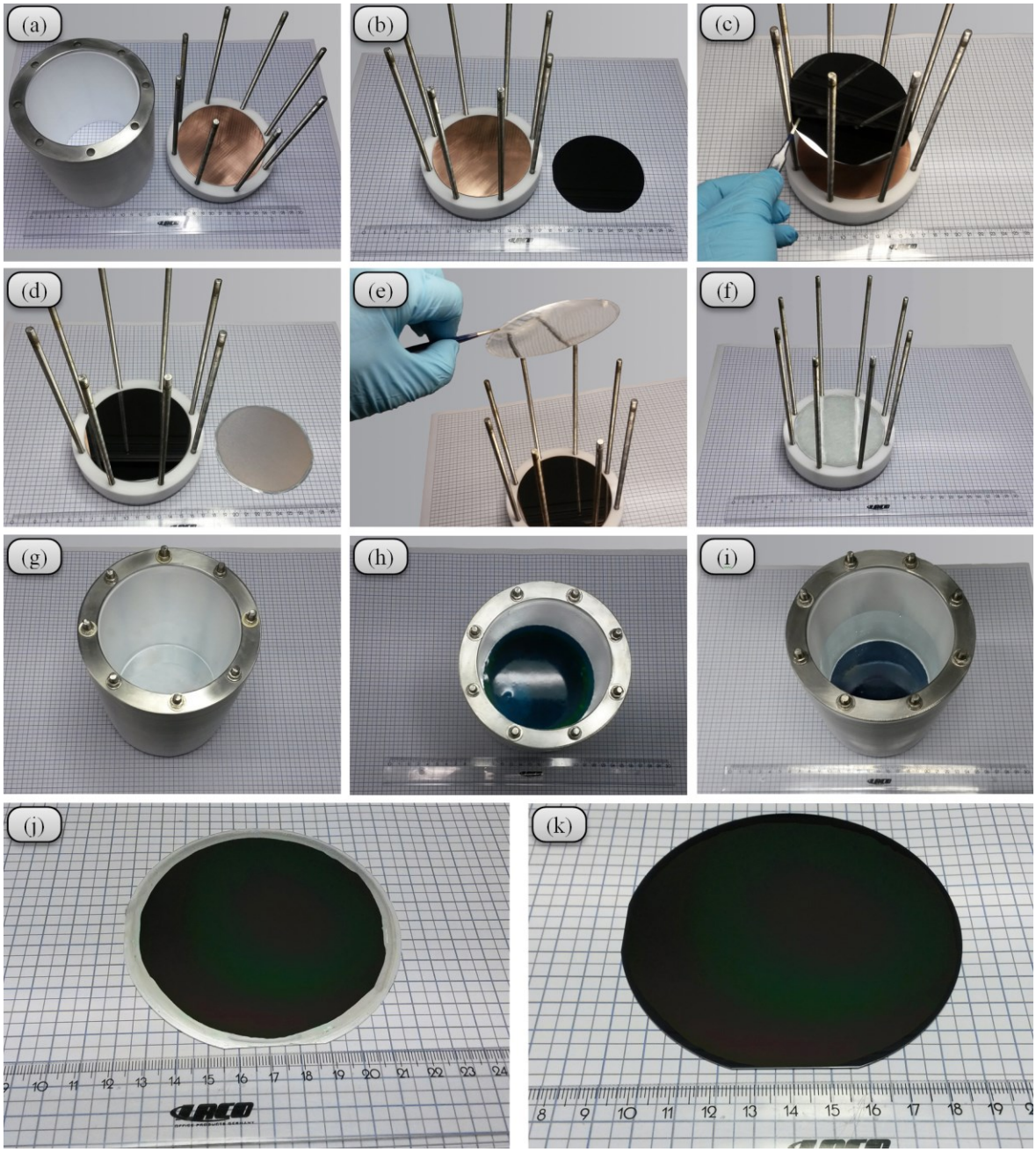

Figure 3–1. Photographs of transferring a 4-inch UTAM onto Si wafer by using the innovative anodization and transferring cell. (a-g) Fixing the Si wafer and the prepared UTAM (with Al backside and barrier layer) inside and assembling the cell. (h) Removing the Al backside in mixture solutions of $CuCl_2$ (85 wt %) and HCl (15 wt %) for 10 min. (i) Removing the barrier layer by using H_3PO_4 solution (5 wt %) at 30 ºC. After dissembling the cell, the attached UTAM on Si wafer is obtained (j) before and (k) after removing the residual Al frame.

3.2.4. Au Nanoparticle Arrays Fabrication

After transferring the UTAM onto Si wafer, Au nanoparticle arrays were prepared by deposition of about 20 nm Au (deposition rate of 0.2 Å/s) on this transferred UTAM which acts as a shadow mask for Si wafer. Finally, the UTAM was removed by using a commercial tape.

3.2.5. Silicon Nanowire Arrays Fabrication

After placing the Au nanomesh onto Si wafer, Si nanowire arrays were fabricated by immersing Si wafer with Au nanomesh in the etching solution ($HF:H_2O_2:H_2O$, v/v/v = 50/25/175). The growth of the nanowires was controlled by the etching times.

3.3. Results and discussion

Highly ordered UTAMs are obtained by using a two-step anodization for polished Al foils according to the literature.[37] Figure 3-2a shows the schematic diagram of the anodization and template-transferring cell for realizing 4-inch sized UTAMs. A long time anodization is necessary to form a regular hexagonal packed nanopore arrays with uniform shapes,[354] which is the reason that a two-step anodization is adopted for achieving highly ordered UTAMs. This also explains that irregular nanopore arrays are obtained in the aforementioned connected UTAMs because it is not physically feasible to deposit a rather thick Al film (at least dozens of micron) for a long anodization. After removal of the alumina obtained from the first anodization, a highly ordered nanohollow arrays are formed on the surface of the Al foil (Figure 3-2b, c). These highly ordered nanohollow arrays serve as a nucleation site for the development of a pore in the early stage of the second anodization,[29, 37] which results in the eventual growth of the UTAM with highly ordered pore channels (Figure 3-2d). In order to form a good attachment between the

UTAM and substrate for following steps, the top surface of the UTAM is polished by ion milling before transferring. Figure 3-2d' shows a scanning electron microscopy (SEM) image of the top surface before polishing, which exhibits clear sharp edges at the triangle joint points of pore walls. After polishing, a smooth top surface of the UTAM is obtained, as shown in Figure 3-2e, e'. Because of increasing adhesion between the UTAM surface and substrate, this process of surface smoothing is indispensable for transferring UTAMs with large area on substrates without twisting and folding.

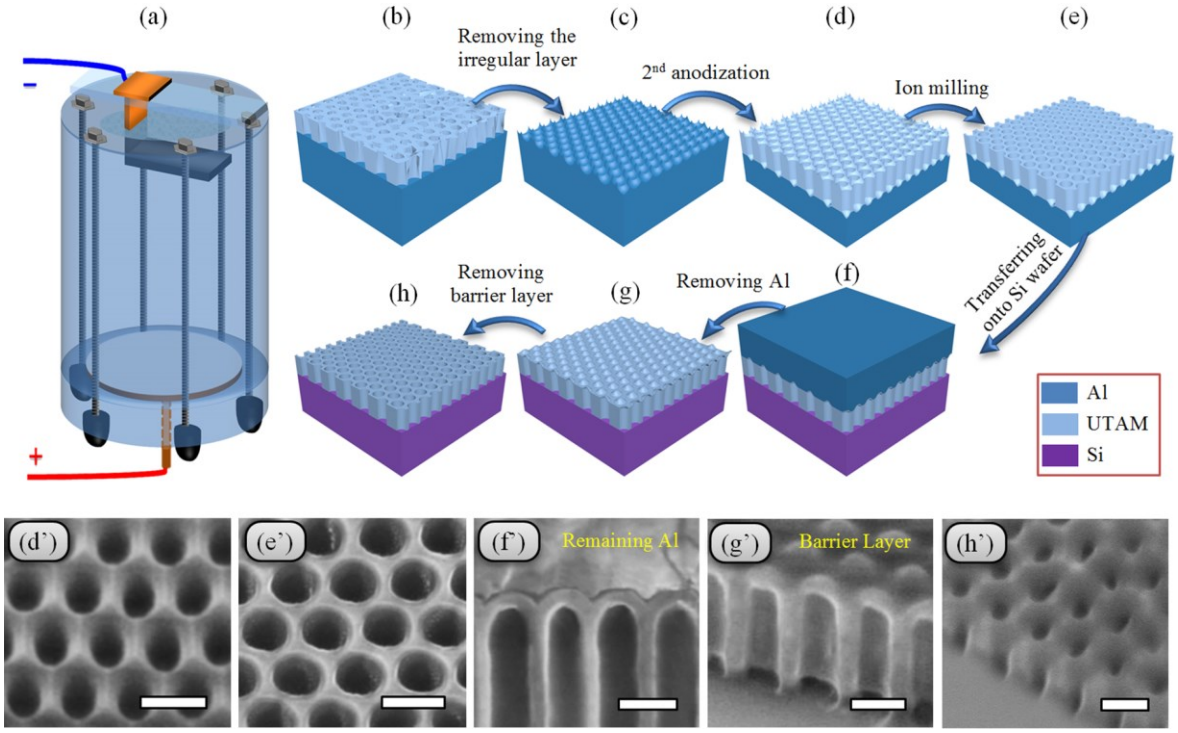

Figure 3–2. (a) Schematic diagram of the anodization and transferring cell for fabricating and transferring 4-inch sized UTAMs. (b-h) Schematic diagram and (d'-h') SEM images of the fabrication and transferring process of UTAM: (b) Al foil with irregular nanopores resulted from first anodization, (c) removing the irregular nanopores generated in first anodization, (d and d') regular nanopore arrays with sharp edges at the surface of the UTAM after second anodization, (e and e') regular nanopore arrays after ion-milling to smooth the surface of UTAM, (f and f') transferring of UTAM onto a Si wafer, (g and g') removing the residual Al at the backside, and (h and h') removing the barrier layer, leading to the UTAM on the Si wafer. (Scale bars in d'-h' are 100 nm).

Because of the ultrathin and fragile nature of UTAMs, it is rather difficult to transfer an intact UTAM over large area on substrate. In the present process, the UTAM is placed

onto the desired substrate before removing the backside Al and the barrier layer (Figure 3-1). To avoid the moving of the UTAM during the following cleaning, pore opening and widening processes, the template is fixed on the substrate by using the anodization and transferring cell, which is crucial for keeping the membrane from twisting, folding and cracking. Several drops of DI water were dropped on the substrate before attaching the UTAM, in order to further improve the contact of the membrane and the substrate. After these processes, the removals of backside Al and barrier layer were conducted successively (as shown in Figures 3-1 and 3-2f-h), which resulted in a UTAM with highly ordered nanopore arrays attached on the substrate. Typical SEM images of UTAMs with backside Al, barrier layer and after removing the barrier layer are shown in Figures 3-2f'-h', respectively.

Figure 3-3 shows the successful transferring of a wafer-scale UTAM onto a Si substrate. It is clear that there is no any twisting, folding and cracking for the transferred UTAM. Because the membrane is fixed on the substrate during the whole process, the possible twisting or folding which may happen in the use of flexible polymeric supporting layer can be excluded. These twisting or folding will affect not only the final packing of the nanopores but also the uniformity due to the nonhomogenous contact with the pore-widening solution.[8] The pore diameter of the obtained UTAM is about 70 nm, as shown in Figure 3-4a. The excellent contact of the UTAM and substrate, and the fixed UTAM during the following cleaning, pore-opening and -widening processes are two critical factors for transferring highly ordered UTAMs on the substrate with large area. It should be noted that there is no special requirement for the sizes (the cell and the substrate) in this process. Therefore, larger UTAMs also can be transferred successfully.

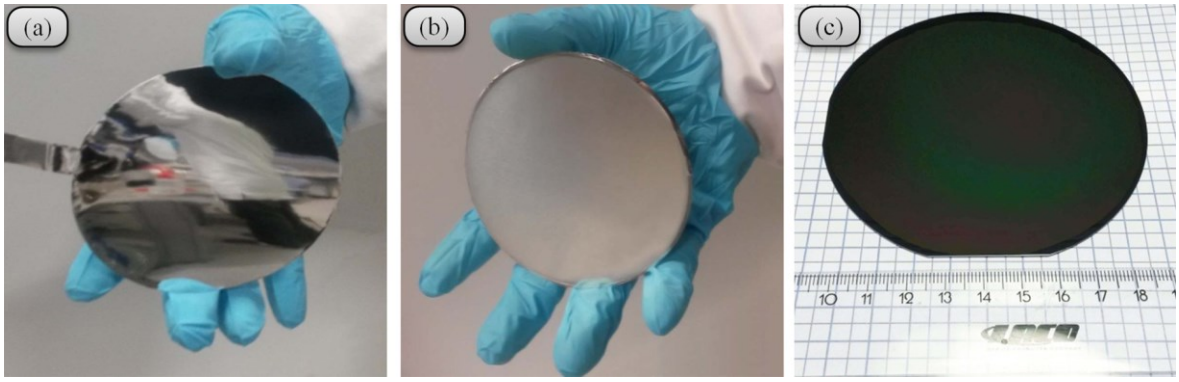

Figure 3–3. Photographs of a 4-inch wafer-scale Al foil after surface polishing for UTAM preparation (a), as-prepared UATM on the Al foil (b), and the UATM transferred on a Si wafer (c).

The successful transferring of UTAMs is dependent on their thickness and the diameter of the nanopores because thinner membrane with larger diameter of the nanopores means more fragile. If the thickness of the membrane is too thin, it will be broken even utilizing this method. Thick UTAM is beneficial for transferring but cannot pattern substrates successfully.[43] For further finding a suitable thickness that can guarantee an intact UTAM with a wafer scale during transferring onto the substrate, the dependences of the UTAM thickness on the anodization time and the diameter of nanopores in UTAMs on the pore-widening duration were systematically studied. Figure 3-4b shows the dependence of the UTAM thickness on anodization time. Table 3-1 shows two kinds of relationships, the relationship between the maximum intact areas and the thicknesses of UTAMs by controlling the anodization times, and the relationship between the pore diameters and the pore widening durations, which clearly exhibits the tunability of the pore diameter (also see Figure 3-5). It is clear that, in this condition, 8 min anodization (about 320 nm thickness of UTAM) is necessary for achieving an intact UTAM over 4-inch wafer scale. Furthermore, an intact freestanding 4-inch wafer scale UTAM with thickness about 500 nm can be fabricated, as shown in Figure 3-6.

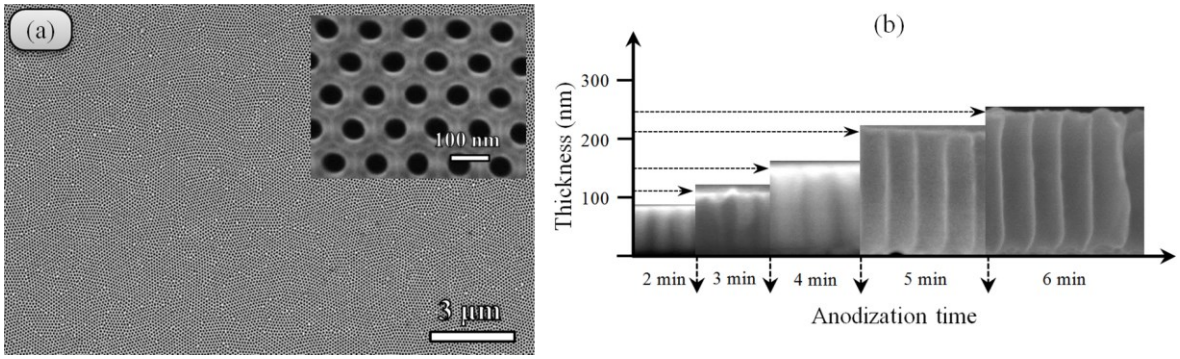

Figure 3–4. (a) Regional and high-resolution (inset) SEM images of the wafer-scale UTAM on Si substrate (top-view). (b) The dependence of the UTAM thickness on the second anodization time.

Table 3-1. The relationship of the maximum intact area with the thickness of UTAMs, and the dependence of the nanopore diameter in UTAMs on the pore widening duration.

Relationship between the maximum transferable area and the thickness of UTAM			**Relationship between the pore diameter and the pore widening duration**	
Second anodization time (min.)	**Thickness of UTAM (nm)**	**Area of UTAM (cm^2)**	**Pore widening duration (min.)**	**Pore diameter (nm)**
1	40-50	1	5	40
1.5	70-80	7	10	45
2	80-100	12	15	52.5
3	110-120	28	20	62
4	150-160	35	25	67
5	190-200	51	30	75
6	230-240	60	35	83.5
7	270-280	72	40	90
8	310-320	78 (~ 4-inch)	45	93.5

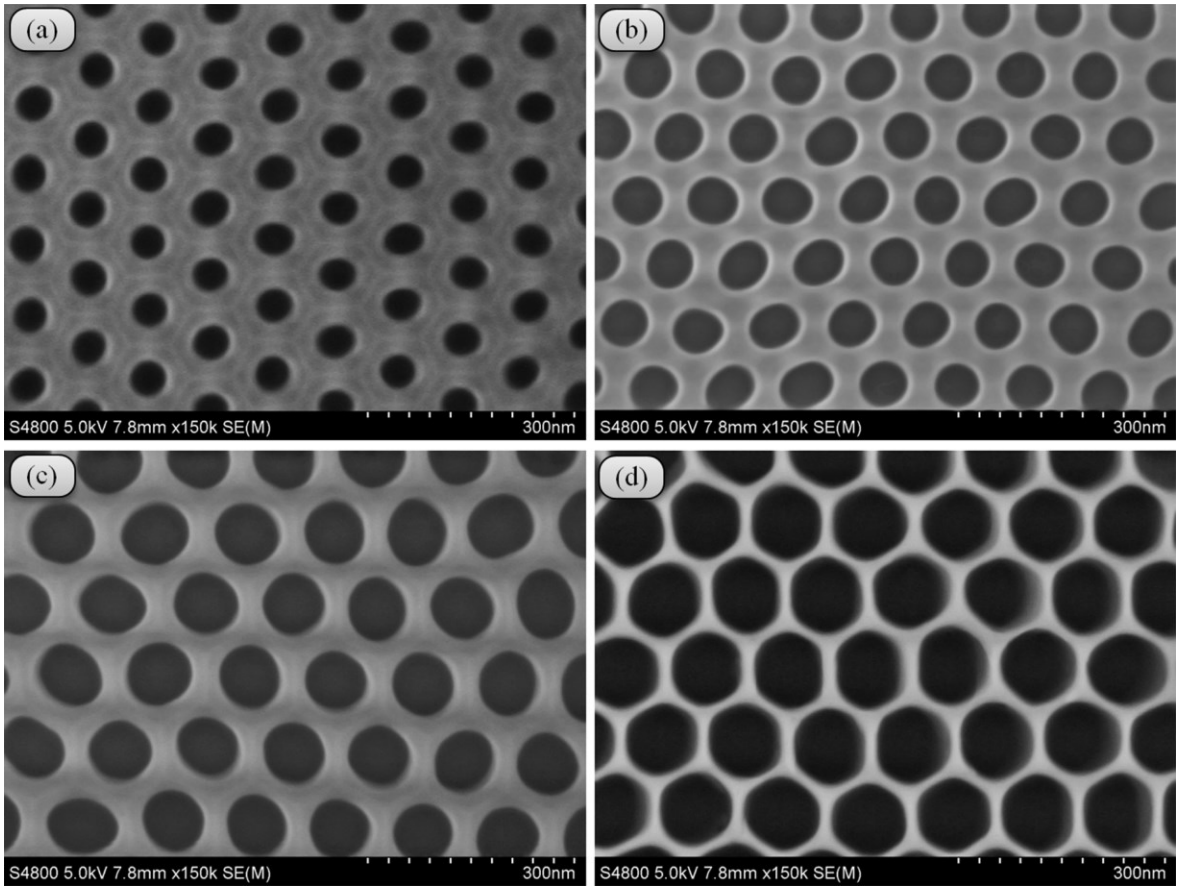

Figure 3–5. SEM images of prepared UTAMs with average nanopore diameters of about (a) 45 nm, (b) 60 nm, (c) 75 nm, (d) 90 nm.

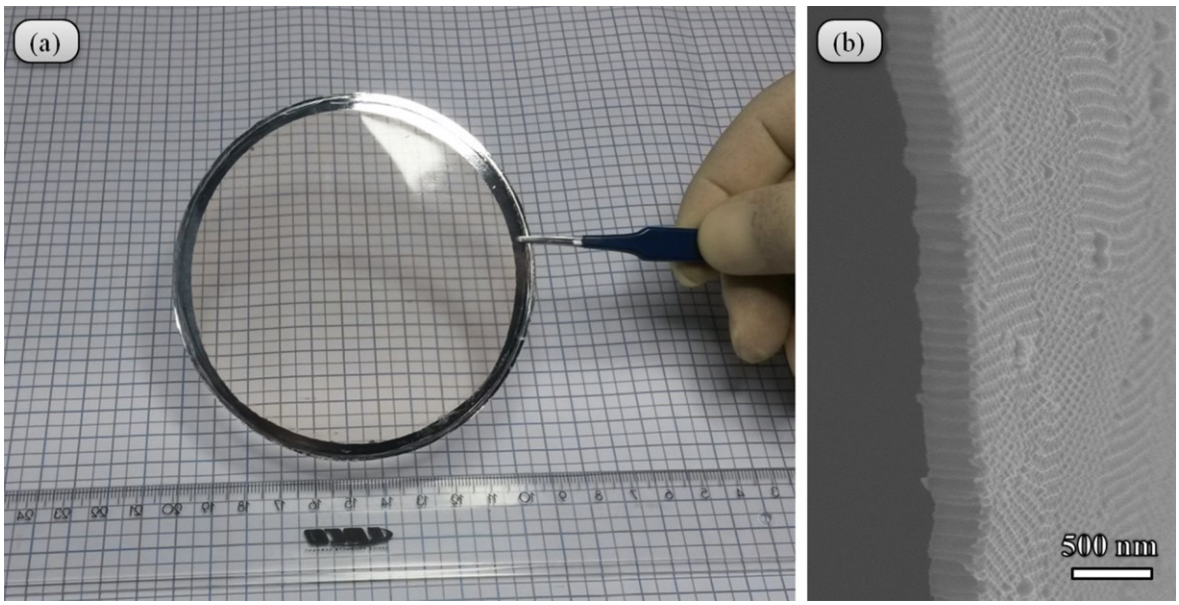

Figure 3–6. (a) Photograph of a free standing 4-inch wafer scale UTAM with the residual Al frame. (b) Large area SEM image of the free standing UTAM with thickness about 500 nm.

To demonstrate the important applications of this novel method, nanoparticle arrays on a Si wafer were fabricated by using this UTAM as mask. Figure 3-7a outlines the fabrication of highly ordered nanoparticle arrays on large area substrate, including the transferred UTAM onto Si wafer, Au deposition and UTAM removing. After these steps, highly ordered Au nanoparticle arrays are prepared on the substrate. As UTAMs are fixed during the removal of backside Al and alumina barrier layer, and no polymeric layers are used to support the UTAMs, highly ordered nanoparticle arrays with uniform diameters are obtained over a large area. Figure 3-7b shows the large-scale highly ordered Au nanoparticle array with a uniform diameter of about 50 nm. By controlling the pore-widening duration, the diameter of the nanopores can be adjusted, which results in nanoparticle arrays with different size as showing in Figure 3-8. In addition, the diameter of the nanoparticles also can be tuned by controlling the thickness of the UTAM (i.e., the anodization time).[37] Because there is no particular requirement for UTAMs in this transferring process, UTAMs with different thicknesses and nanopore diameters can be transferred by using this method. The diameter of nanoparticles can be tuned in the range from sub-10 nm to submicron over large area.[37, 354-356] Also, there is no special requirement in the deposition step, which means many methods can be used to fabricate the nanoparticle arrays such as vapor sublimation, vapor evaporation, electron-beam deposition and sputtering. Furthermore, any material that can pass the nanopores of UTAMs can be fabricated into nanoparticle arrays with tunable dimension by using the present method, which shall extensively extend the application of nanoparticle arrays.

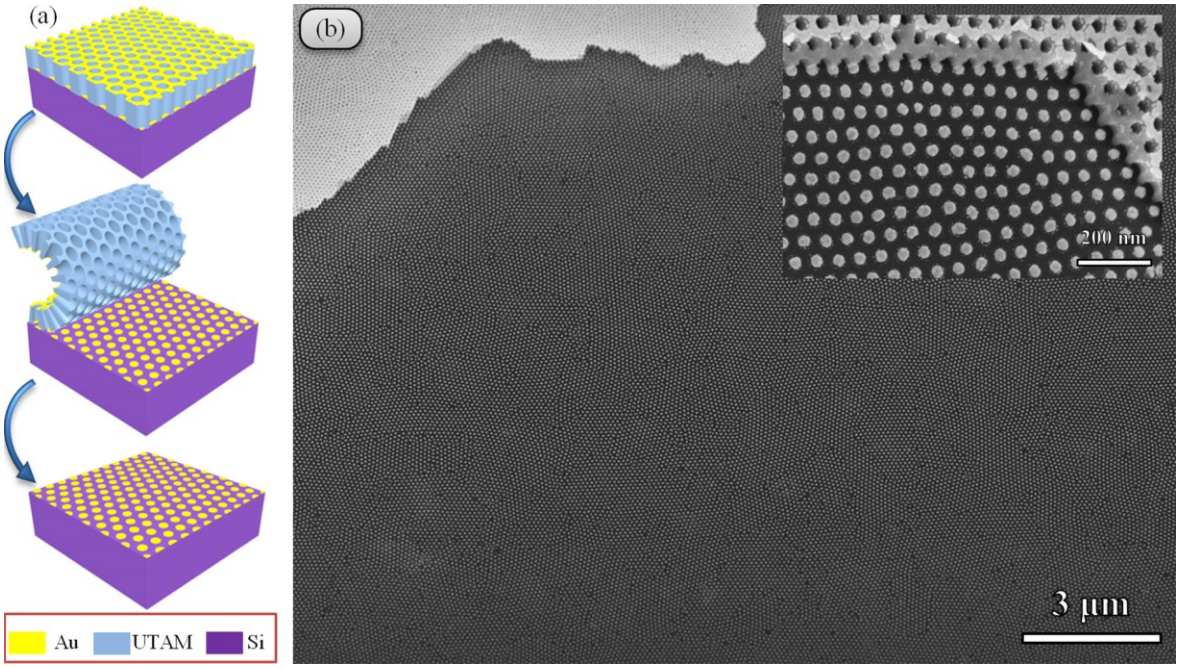

Figure 3–7. (a) Schematic diagram of the fabrication process of Au nanoparticle arrays on Si wafer by using the UTAM as a shadow mask. (b) Regional and high-resolution (inset) SEM images of Au nanoparticle arrays fabricated on Si wafer with large area, in which parts of the UTAM are remained intentionally.

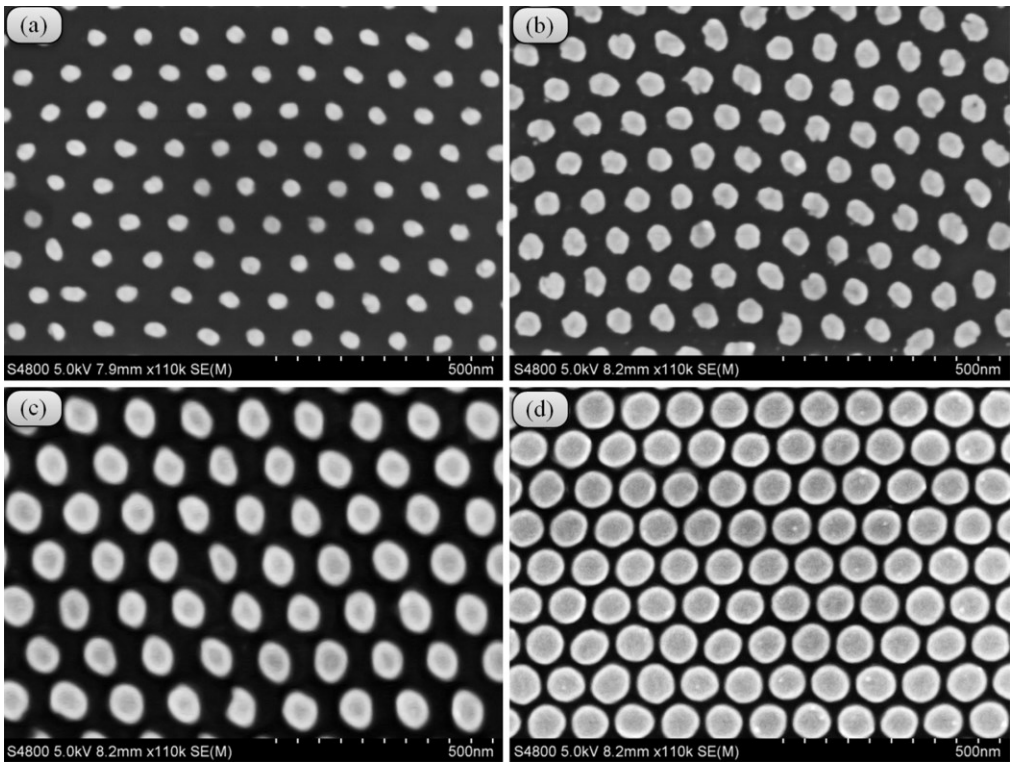

Figure 3–8. SEM images of Au nanoparticle arrays with average diameters of about (a) 45 nm, (b) 60 nm, (c) 75 nm, (d) 90 nm.

Besides nanoparticle arrays, the fabrication of nanomesh with highly ordered nanopore arrays can be realized over large area, just by reversing the procedures of Au deposition and UTAM transferring. Nanomeshes also attracted much attention due to their various applications, such as plasmonics, photovoltaics, metal-assisted chemical etching (MaCE) of Si and shadow mask for etching or transmission of light at subwavelength scale.[217, 229] Figure 3-9a-e shows the schematic diagram for fabrication of Au nanomesh with thickness of about 20 nm on Si wafer. Figure 3-9d', e' are the typical SEM images of Au nanomeshes on Si wafer before and after removing UTAM, respectively. By using this method, many materials can be fabricated into nanomeshes over large area.

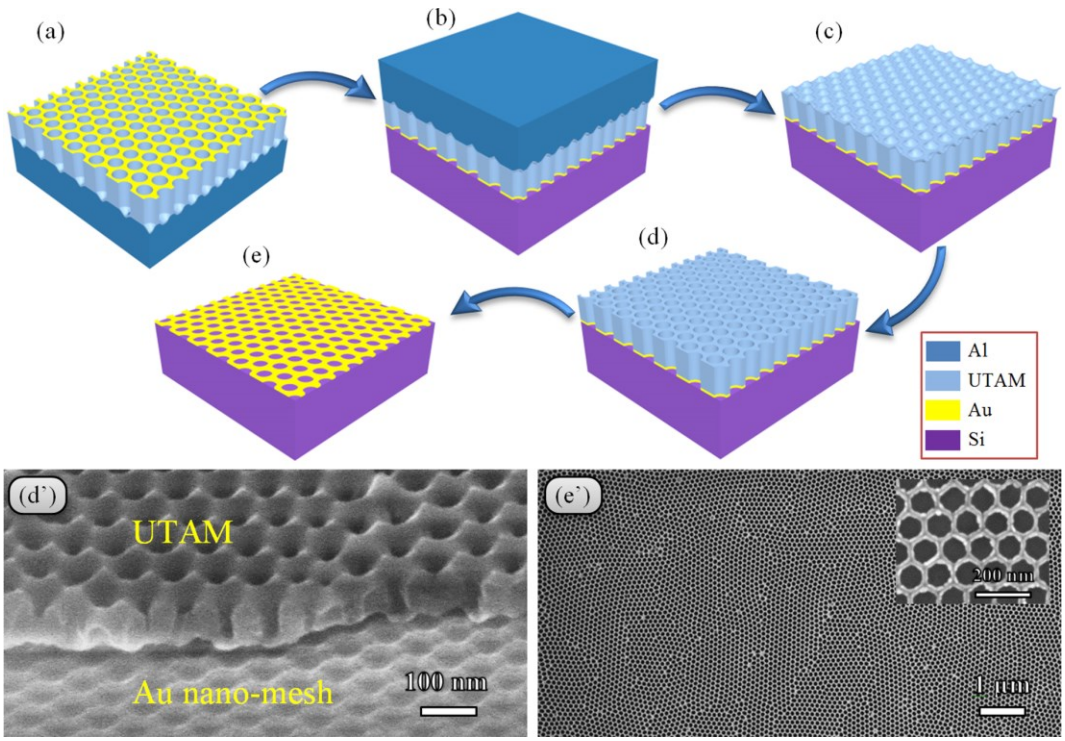

Figure 3–9. Schematic diagram (a-e) and SEM images (d'-e') for the fabrication of Au nano-mesh on Si wafer: (a) deposition of Au on UTAM, (b) transferring the Au nano-mesh onto Si wafer, (c) removing the residual Al at the backside, (d and d') removal of the barrier layer, and (e and e') Au nano-mesh on Si wafer after removing UTAM (the inset of (e') is the enlarged view).

As a proof to demonstrate the applications of metal nanomeshes fabricated by this UTAM technique, Si nanowire arrays are fabricated by MaCE method using the obtained Au nanomesh as catalyst to etch Si wafer. Figure 3-10a outlines this process, in which the whole Si wafer with Au nanomesh (4 in.) is dipped in the etchant ($HF:H_2O_2:H_2O$). After the MaCE process, highly ordered Si nanowire arrays are obtained on the surface of Si wafer. During the etching process, the HF in the etching solution dissolves the oxidized Si that formed by oxidation of Si beneath the metal (Au) catalyst with the presence of H_2O_2. The length of Si nanowires can easily be controlled by monitoring the etching time, as shown in Figure 3-10b-d.

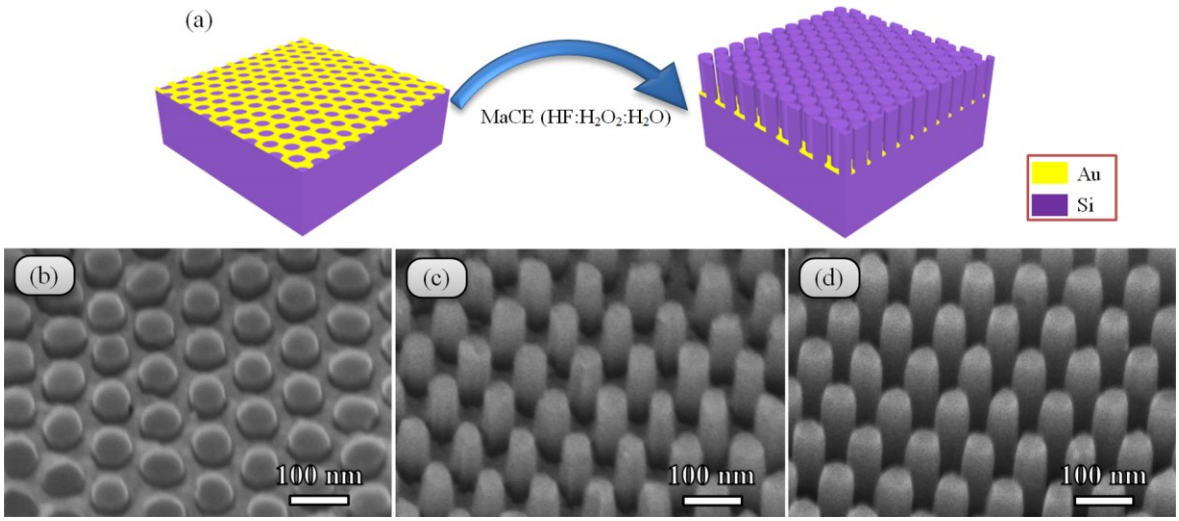

Figure 3–10. (a) Schematic diagram for the fabrication of Si nanowire array by using Au nano-mesh as catalyst. SEM images of Si nanowires by etching for (b) 3, (c) 5 and (c) 10 min.

3.4. Conclusions

Here, a facile and cost effective method for the effective transferring of wafer-scale UTAMs onto substrates was demonstrated. This method guarantees the uniformity and regularity of the nanopore arrays and prevents the UTAM from external contaminations, due to not using a polymeric supporting layer, the good contact between the UTAM and the substrate, and the fixed UTAM during the entire process. By controlling the thickness

of the UTAM, wafer-scale UTAM can be transferred on the desired substrates without any twisting, folding, or cracking, and various nanostructure patterning are achieved over large area by using these transferred UTAMs as templates. Because there is no requirement for the UTAMs, substrates and materials for deposition, various nanostructures including nanoparticle, nanopore (nanomesh) and nanowire arrays can be fabricated on different substrates with tunable and uniform dimension. This work shall pave a way to achieve large-scale nanostructure patterning and provide a platform for various applications of highly ordered nanostructure arrays.

4. Dimensional Dependence of the Optical Band Edge of TiO_2

4.1. Introduction

In consideration of the attractive property of TiO_2 that has been broadly utilized in dye-sensitized solar cells,[357, 358] photocatalysts,[359] and photonics, [360, 361] this chapter focuses on the optical bandgap modulation of TNTs which were fabricated by the approach combining anodic aluminum oxide templates and atomic layer deposition (ALD). The subsequent absorption spectroscopic measurements demonstrated that the absorption band edge of the arrays exhibited a red shift when the diameter tuned bigger and kept the wall thickness (W_t) of TNTs constant. Finite-difference time-domain (FDTD) simulations supported the observations and illustrated a large near-field enhancement around the outer space of the nanotubes as the distance between two nanotubes to a small value is manipulated. Therefore, an alternative possibility obtained by tuning the optical bandgap of nanostructure arrays without concerning quantum confinement effects.

4.2. Experimental

The AAO template was prepared by anodic oxidation of high-purity aluminum foil (99.999%) according to the previous reports.[36, 37, 115] The AAO template thickness and pores diameters were fixed by well controlling the time of anodization and pore widening processes. Seven samples of AAO with different diameters were placed inside the chamber of the ALD, followed by the increase of temperature to 250 ºC. $TiCl_4$ and H_2O were selected as Ti and O_2 sources, and N_2 gas was used as both carrier gas and purge gas. The typical pulse time used to introduce the $TiCl_4$ and H_2O precursors was 0.1 s, and the N_2 purge time was 5 s. The initial depositing cycles were 40 cycles to generate a 1.84 nm TiO_2 continuous layer that covered the entire surface of template. Thereafter, samples were

annealed inside the ALD chamber at 480 ºC for 1 h to create a crystalline seed layer for next 160 cycles of TiO_2 deposition at 400 ºC. The total deposition cycles were chosen as 200 cycles to produce a specific TiO_2 nanotube wall thickness (9.2 nm). The as-prepared TNTs were examined using a scanning electron microscope (SEM, Hitachi S 4800) and transmission electron microscopes (Philips TECNAI and FEI Titan 80-300). X-ray diffraction (XRD, Siemens D5000) was utilized to analyze the crystal structure of the TiO_2 nanotubes. A UV−vis spectrometer (Varian) was adopted to measure the absorption characteristic of the TNTs. The optical properties of TNTs were simulated using three-dimensional full-field finite difference time domain methods (Lumerical FDTD Solutions Inc. 8.9). The dielectric constants were obtained from a fit to the experimentally recorded refractive index data of the ALD deposited TiO_2 thin films which were used in nanotubes fabrication. Broad-band linearly polarized plane waves were perpendicularly incident onto individual nanotube arrays with periodic in-plane boundary conditions. Seven TiO_2 nanotubes with the same geometric parameters as those in the real samples were used for all set of the simulations in a hexagonal geometry. Meshing size as small as 1 nm was used in the regions containing TiO_2, which was proven fine enough in convergence tests. The field vectors were monitored in three dimensional grid points to extract transmittance spectra of TiO_2 nanotubes and to generate field distribution maps at wavelengths of interest.

4.3. Results and discussion

The geometrical modulation of the TiO_2 nanotubes arrays begins with the precise tuning of the AAO templates. Figure 4-1 shows SEM images of the AAO templates with a series of diameters (D: 30, 40, 50, 60, 70, 80 and 90 nm) and inter-pore distances (the distance between the edges of two neighbor pores, d_S: 80, 70, 60, 50, 40, 30 and 20 nm).

The length is controlled as 1 μm by choosing the same anodization time for the samples as shown in Figure 4-1a. All these templates exhibit a uniform porous profile and perfectly ordered pore distribution, supplying us a good platform to fabricate well-controlled TNTs.

The subsequent procedure for attaining TNTs is depicted as the schematic in Figure 4-2a. Procedure 1 represents the growth of TiO_2 in AAO templates by ALD method and 200 cycles of deposition result in a thickness of 9.2 nm. Herein, the samples kept at same thickness to focus on the other factors and rule out the impact of quantum confinement effects. Procedure 2 describes the removing of TiO_2 surface layer by Argon ion milling, which is necessary to make the nanotube with a uniform pore size and to remove the 2-D layer of TiO_2 from the surface. Procedure 3 shows the removing of aluminum in the backside to facilitate the optical absorption measurements. Finally, well ordered TNTs are prepared and schematically shown in Figure 4-2b, where the distributing of the nanotubes is purposely depicted to be hexagonal to match the real samples and FDTD simulation parameters.

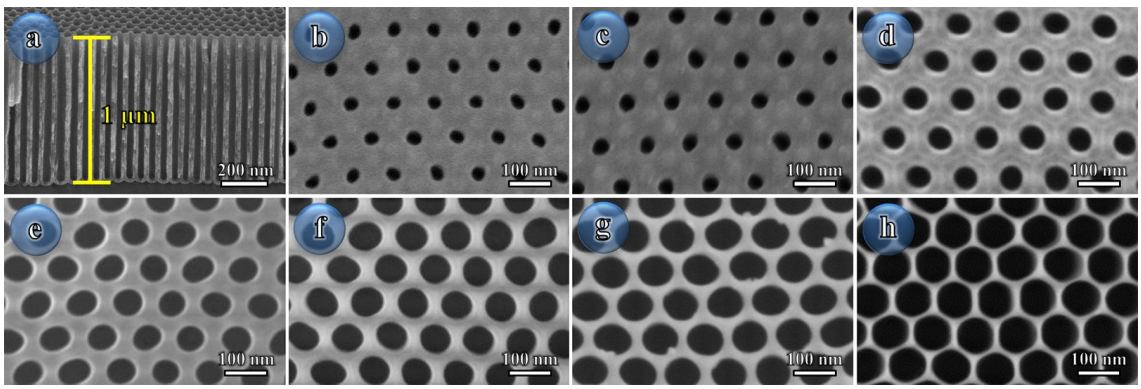

Figure 4–1. SEM images of the prepared AAO templates: (a) Cross-sectional image of AAO prepared by anodizing aluminium foil for 25 min at 7 ºC. The fabricated samples have different pore diameters as well as inter-pore distances: (b) D=30 nm, d_S=80 nm. (c) D=40 nm, d_S=70 nm. (d) D=50 nm, d_S=60 nm. (e) D=60 nm, d_S=50 nm. (f) D=70 nm, d_S=40 nm. (g) D=80 nm, d_S=30 nm. (h) D=90 nm, d_S=20 nm.

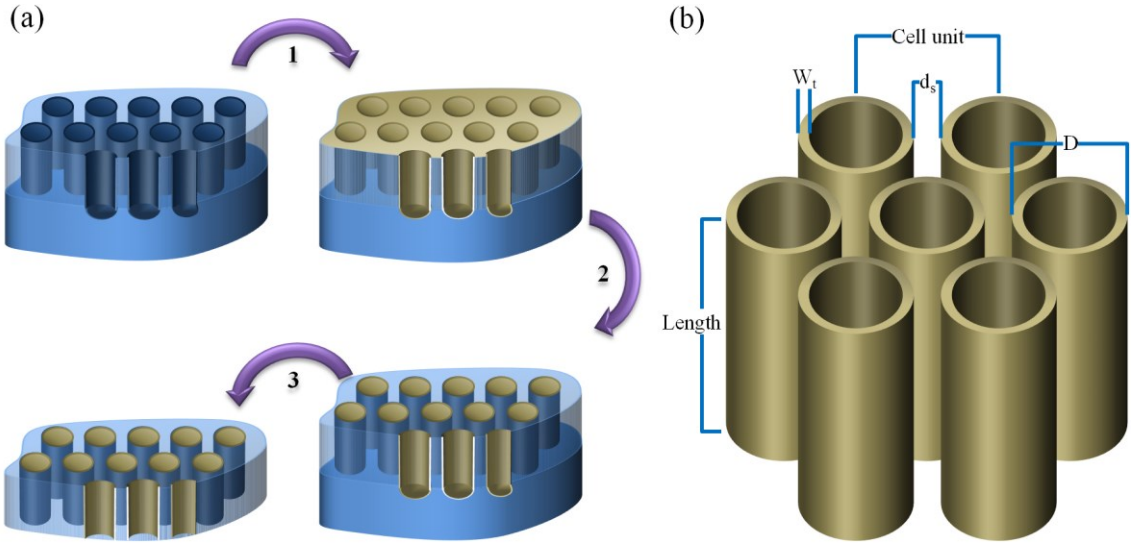

Figure 4–2. Schematic diagram of: (a) Preparation procedures of TNTs: (1) TiO_2 deposition via ALD, (2) Removing the surface layer of TiO_2 by Argon ion milling, (3) Removing aluminum in the backside. (b) Geometric illustration of the hexagonal nanotube arrays.

Particularly in the procedure of ALD deposition, temperature was controlled at 250 ºC. After deposition of the initial 40 cycles, the samples were purposely annealed at 480 ºC for 1 h to improve the crystalline quality. The resultant 1.84 nm thick layer was utilized as the seed layer for the growth of the rest 160 cycles. Figure 4-3a shows the representative SEM images of the TiO_2 nanotube array in the AAO template after Ar ion milling. The entire AAO pores surface is covered by a thin layer of TiO_2. To check the infiltration of TiO_2 to pores, different regions of the image have been resolved: the top view, cross-sectional view near the top and the bottom of the array. All these images illustrate a uniform TiO_2 thickness running through the entire pores, indicative of a great advantage of ALD technique to grow thin film uniformly without concerning the roughness of the substrates. After AAO template removal by soaking the samples in acidic solution, freestanding nanotubes arrays have also been attained even in a large scale as shown in Figure 4-3b.

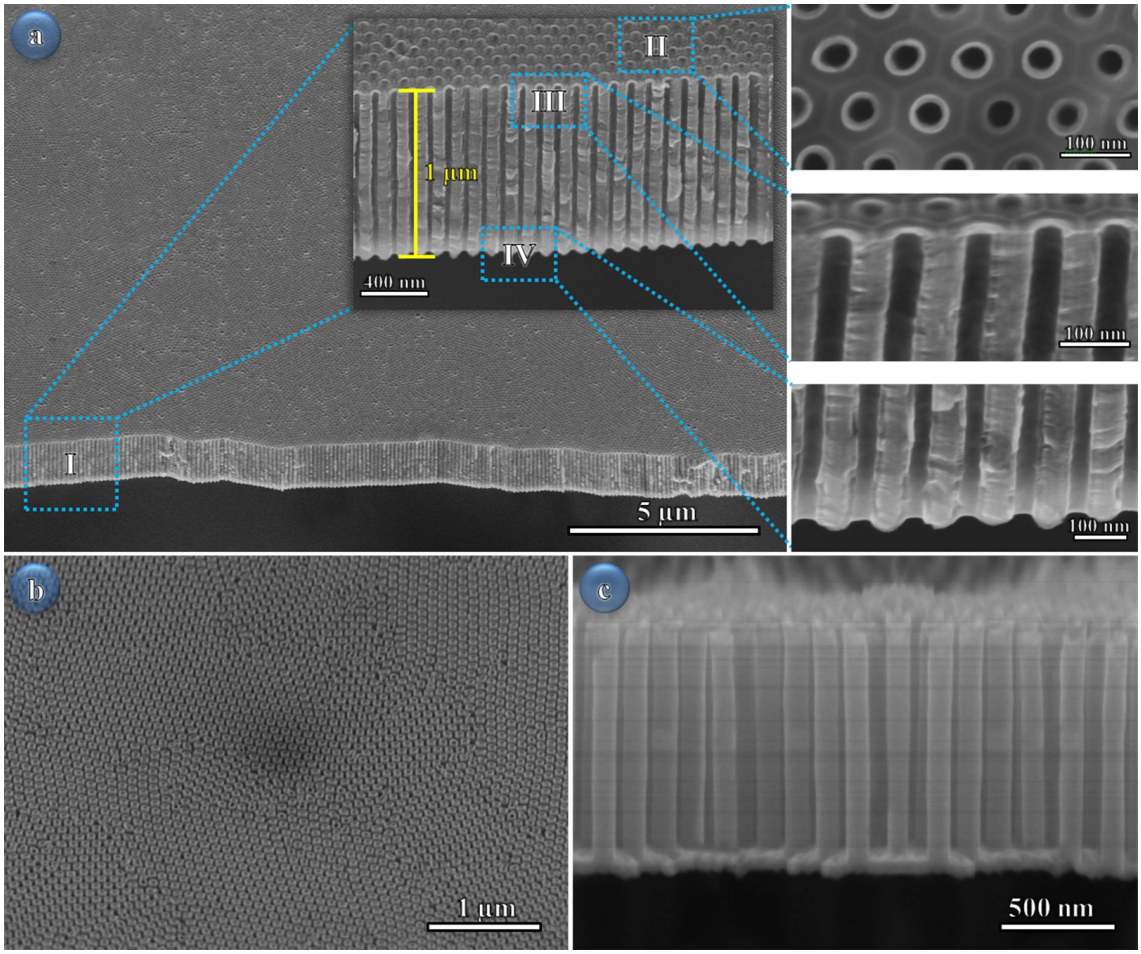

Figure 4–3. SEM micrographs of the prepared TNTs, (a) Uniform TiO_2 layer covered entire surface of AAO template pores, the magnified SEM image of the region (I) shows the uniformity of TiO_2 layer on surface of AAO template pores, while the magnified SEM images of the regions (II, III and IV) show the uniform layer of TiO_2 at the top view, cross-sectional view around the top and the bottom of the arrays, respectively (b) SEM image for the prepared TNTs after removing the rest of aluminium and AAO template. (c) Cross-sectional view of the freestanding TNTs.

Figure 4-4a shows the TEM images for a representative TiO_2 nanotube. As expected, the specific two-step ALD procedure results in a good crystalline quality for the grown nanotubes, which can be evidenced by the HRTEM image and selected area electron diffraction (SAED) pattern shown at the bottom. The crystal lattice fringes are clearly observed in the HRTEM image of region II and the average distance between the adjacent lattice planes is 0.35 nm, corresponding to the (101) plane distance of anatase TiO_2. Liu *et al.*[362] have proven that the crystallinity of TiO_2 can be improved by controlling of the growth temperature to 400 ºC. In this approach, such good crystalline quality of the as-

grown material is obtained by two-step deposition without any additional annealing procedure for the second layer. During the deposition of second layer at 400 ºC, due to the slow ALD deposition process, TiO_2 is favorable to grow in an epitaxial way on the TiO_2 seed layer with high crystallinity. The thickness of the wall of nanotube is around 9.2 nm and the diameter is around 80 nm, as gauged by the intensity profile across the nanotubes shown in the inset of Figure 4-4a.

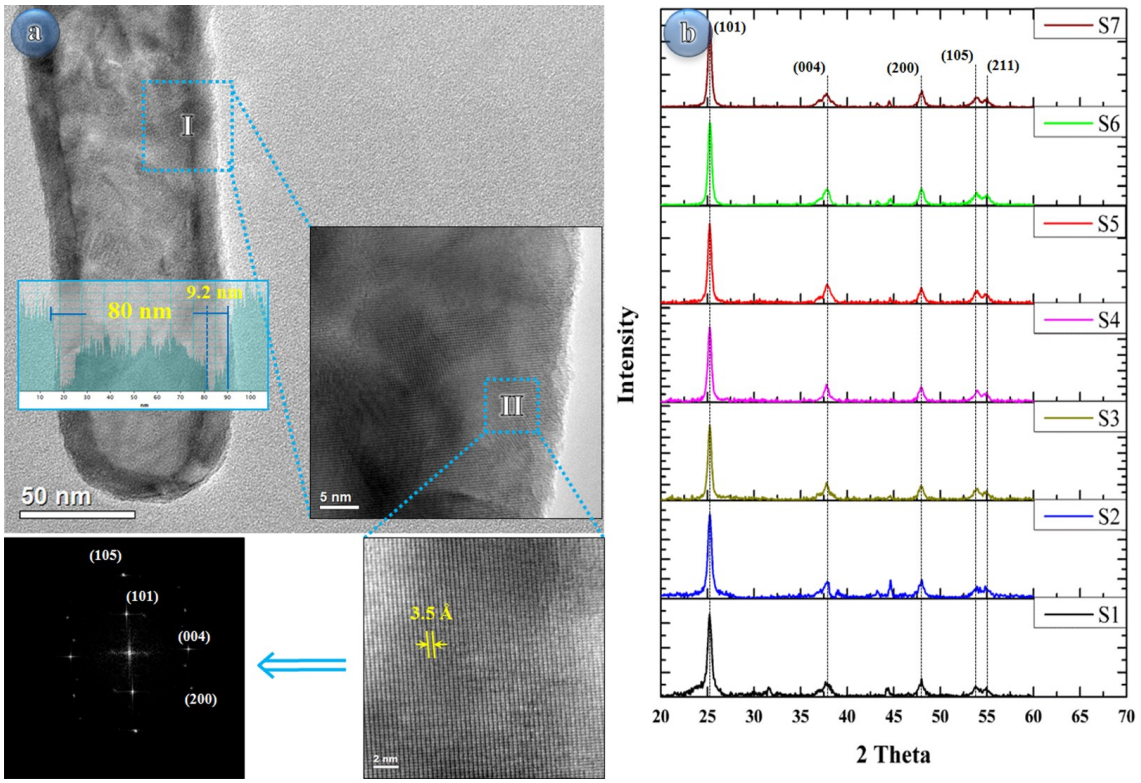

Figure 4–4. (a) TEM micrographs of a representative TiO_2 nanotube with thickness (W_t) of 9.2 nm and diameter (D) of 80 nm. The inset image of the region II shows the crystalline TiO_2 nanostructure, and the HRTEM image of the region II shows a single crystalline structure of anatase TiO_2 nanostructure with a lattice spacing of 0.35 nm. SAED pattern is given on the left side. (b) XRD patterns showing the structure evolution of all the prepared samples of TNTs (S1-S7).

Figure 4-4b presents the XRD patterns of the series of prepared TNTs with different diameters but same thickness, where a crystal structure of anatase TiO_2 could be easily concluded. The main diffraction peak belongs to the (101) planes, in good agreement with HRTEM analysis. To investigate impact of the geometric parameters on the absorption

properties of the nanotube arrays, the nanotube arrays with a constant wall thickness of 9.2 nm but different diameters are prepared. The relevant TEM images are given in Figure 5-5, where the purposely controlled diameter is measured as 30 nm, 40 nm, 50 nm, 60 nm, 70 nm, 80 nm and 90 nm, respectively

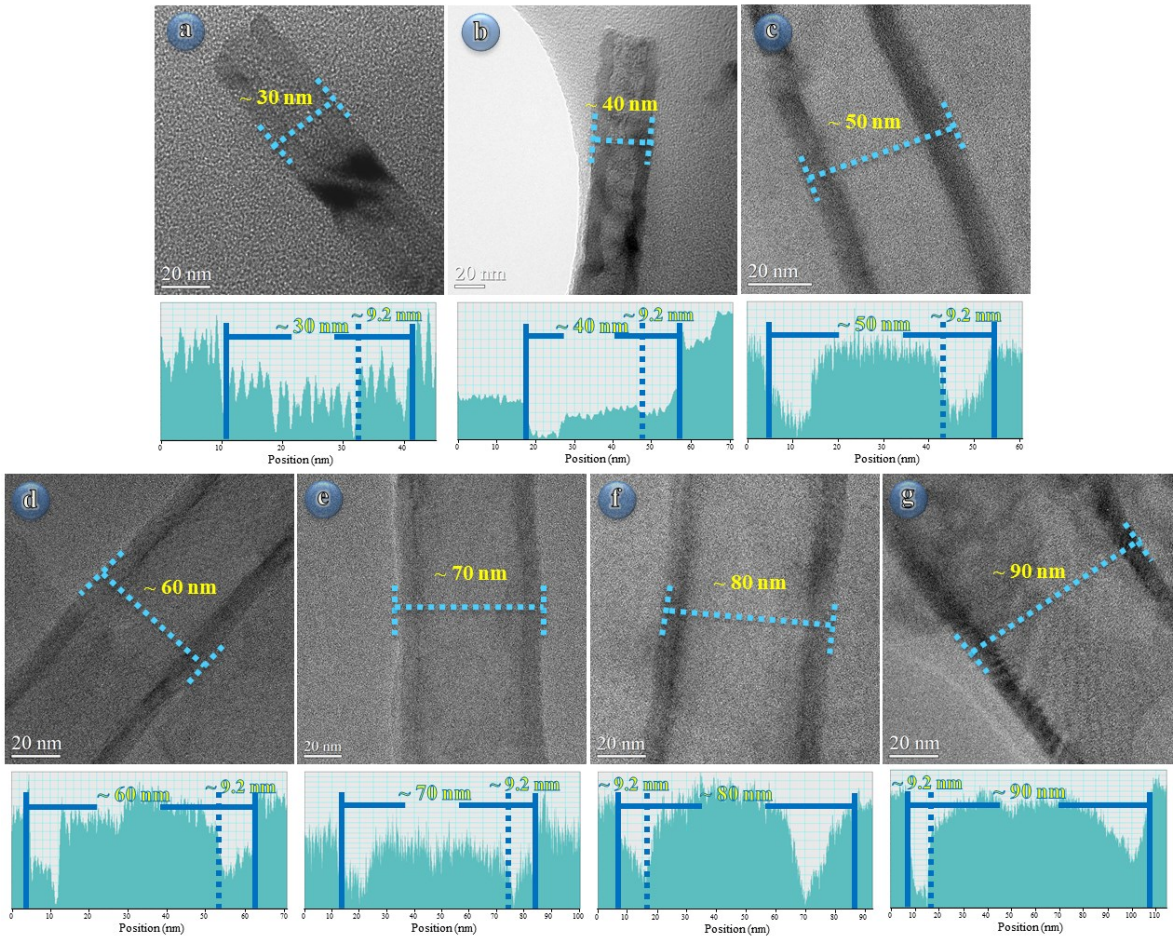

Figure 4–5. TEM images of the prepared TiO_2 nanotubes with the same wall thickness but different diameters. The figure under each TEM image shows the the intensity profile across the nanotube.

Figure 4-6a shows the absorbance spectra of TNTs after subtracting the AAO template effect during the measurement. All these absorbance curves show an absorption band edge in the range of 350-400 nm, consistent with the absorbance spectrum of anatase TiO_2.[8, 363] Though the thickness of these specimens is kept in the same value as 9.2 nm and the quantum effect should not render specificity among the resulted spectra, an obvious red

shift for absorption edge can still observed according to the increase of diameters of the relevant nanotubes. In order to understand the interaction of photons with TNTs more deeply, FDTD simulations were performed and the simulated absorbance spectra for the same series of nanotube arrays are presented in Figure 4-6b. The same tendency of red shift with the widening of the nanotubes could also be prominently discerned in these simulated curves, revealing that there must be some other factors causing the shift of absorption edge beyond quantum confinement effect. To make the observation more convincing, the experiment and simulations have repeated in multiple times and the according spectra with calculated error bars in the resolved range are shown as the insets of Figure 4-6a, b. All of these spectra indicate a clear red-shifted tendency of optical absorbance onset of the TNTs with the enlarging of the diameters.

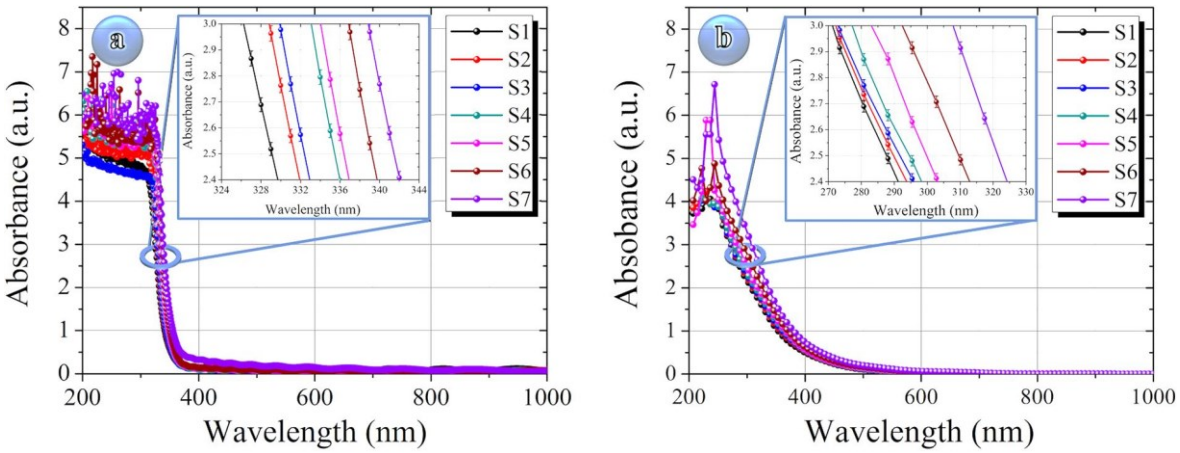

Figure 4–6. (a) Experimental absorbance spectra of the prepared TNTs, the inset shows the red-shift of the absorbance spectra for a specific region. (b) Simulated absorbance spectra of the proposed TNTs using FDTD simulation, the inset shows the red-shift of the absorbance spectra for a specific region.

More resolved spectra focused on the absorption edge in the form of Tauc plots are given in Figure 4-7 and it can be clearly observed that the absorption onset is determined by the geometrical parameters like the diameters (D) and internal distance (d_S) of the nanotubes. Regarding that TiO_2 is classified as a standard indirect semiconductor, an

indirect transition model is preferentially used, to estimate the optical bandgap (E_g) values.[8, 363]

$$\alpha = \left(h\nu - E_g\right)^2 / h\nu \tag{4-1}$$

where α is the optical absorption coefficient near the absorption edge, $h\nu$ is the incident photon energy.

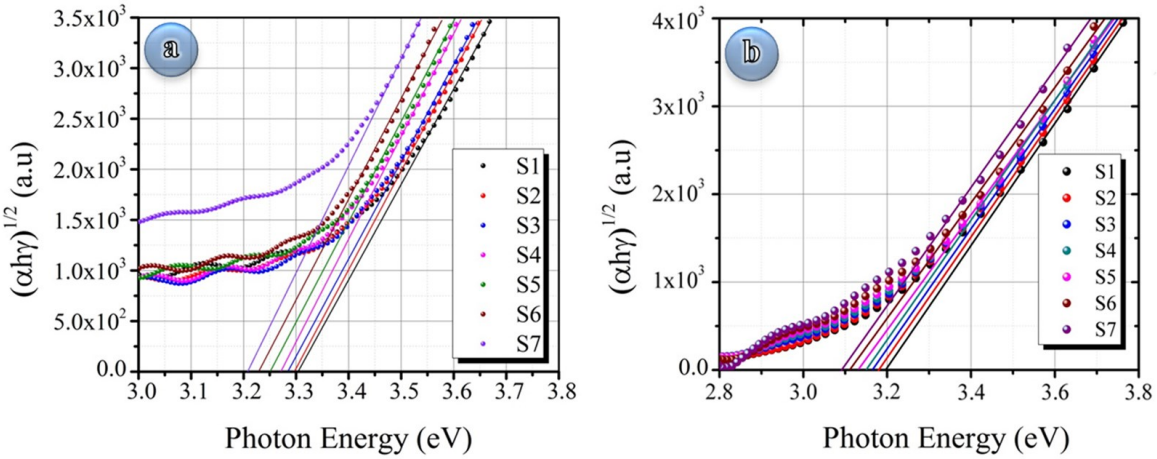

Figure 4–7. Calculations of the indirect optical bandgaps of TNTs, (a) Experimental, (b) FDTD simulation.

As the size of the nanostructure decreasing, indirect transitions could not explain all the findings and direct transitions begin to be influential. Thus, the same analysis based on the direct transitions and the according results are also given in Figure 4-8. The direct optical bandgap calculated from equation:[8, 363]

$$\alpha = \left(h\nu - E_g\right)^{1/2} / h\nu \tag{4-2}$$

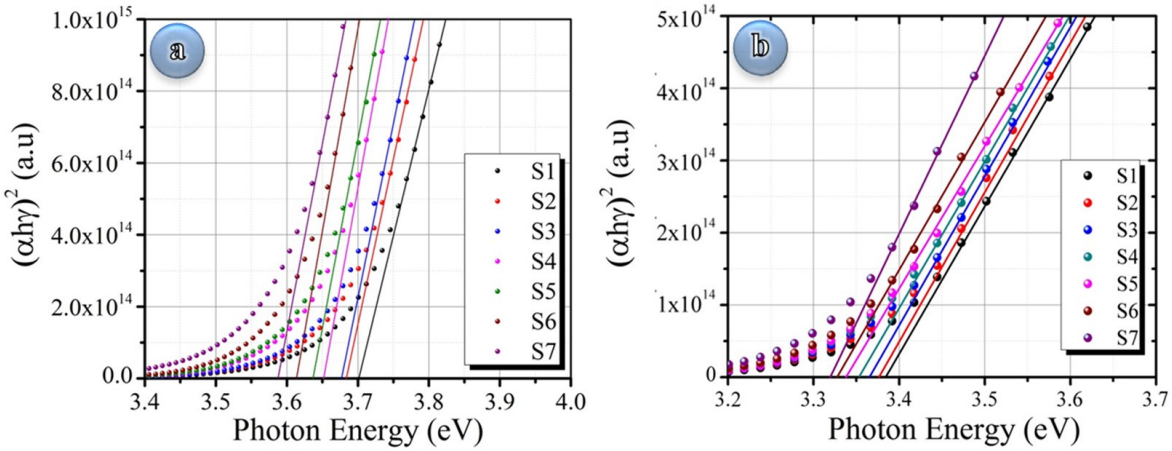

Figure 4–8. Calculations of the direct optical bandgaps of TNTs, (a) Experimental, (b) FDTD simulation.

As exhibited in Figure 4-9a, the indirect optical bandgap values from both the experimental and simulated data as the function of nanotube diameters are plotted. Though the estimated optical indirect bandgap values from experiment and simulation present somewhat deviations probably because of the unavoidable roughness of the real samples, the narrowing of optical indirect bandgap relevant to widening of the nanotube diameters for the two sets of data could be straightforwardly concluded. Moreover, considering the reversely proportional relationship of nanotube diameter and the internal distance between the nanotubes, the plots of optical indirect bandgap vs. internal distance is also presented in Figure 4-8. These curves can confirm the observations in another aspect. To establish a universal analysis, the normalization of two geometrical parameters using D/d_S and the corresponding correlations with indirect optical bandgap change are shown in Figure 4-9b. With the increase of D/d_S, $\Delta E_g/E_g$ presents a decay feature that could be interpreted by a single-exponential model. Using the equation:

$$\Delta E_g/E_g = Ae^{-\omega/\tau} \tag{4-3}$$

where A is the constant and ω is the ratio of the nanotube diameter to internal distance of nanotubes $(\omega = D/d_S)$.

To fit the curves, decay constants (τ) for the experimental and FDTD simulated results are attained as 1.885 ± 0.122 and 1.067 ± 0.26, respectively. Though the two values show a little variation probably due to the surface roughness from the real samples, thus it can still conclude that the geometric parameters cause the bandgap shift without including the quantum effects.

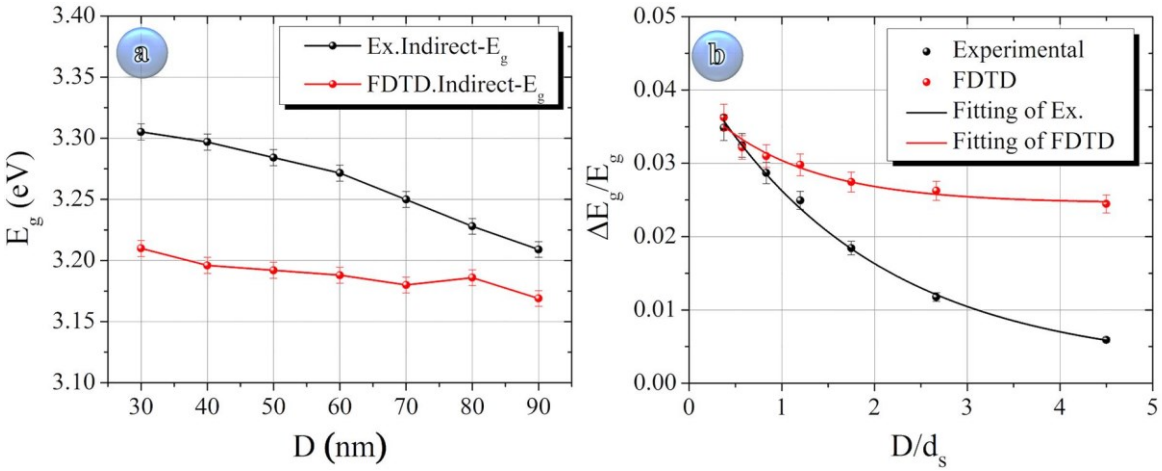

Figure 4–9. (a) Optical bandgap of the TNTs with different diameters, (b) Plots of $\boldsymbol{\Delta E_g/E_g}$ vs $\boldsymbol{D/d_S}$ for experimental and FDTD simulated results.

As demonstrated in Figure 4-10, like the indirect transitions, the direct optical shows the same dependence on the nanotube diameters and distance between two nanotubes. In conclusion, all these data point out that the geometrical parameters could also cause an obvious change in optical bandgap, apart from quantum effects. To investigate it more deeply, the interaction of the incident radiations with the nanostructure should be considered.

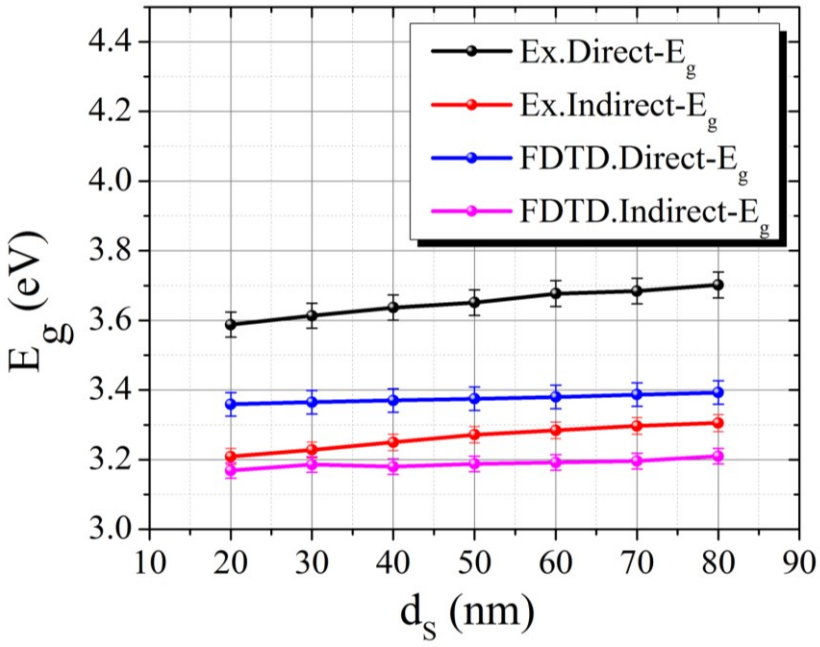

Figure 4–10. Bandgap value as a function of internal distance of TiO_2 nanotubes.

Figure 4-11 shows the simulated electric field distribution around the nanostructures in both top and cross-sectional views, when the samples are illuminated by the photons at 300 nm, 500 nm and 900 nm, respectively. The intensity decays as the spot moves from the surface of the nanotubes to the void space, implying that the interaction of photons and the nanostructure occurs on the outer surface of the nanotube, and the geometric property of such nanostructure could impact the interaction. By comparing the electric field of the samples with different geometrical parameters, it is easy to discover that the field intensity around the outer surface of nanotubes becomes higher as the diameter increases, implying a stronger coupling of the electric field for the sample with a smaller gap. This could be observed straightforwardly in the cross-sectional views of these structures by showing standing waves in between the nanotubes. Careful observations indicate a series of antinodes distributed along the longitudinal direction of the one side open tubes via a Kundt's tube experiment. These high intense spots are very similar to the plasmon hot spots on the surface of metallic nanoparticle arrays.[361] Though the electron density in TiO_2 is much lower than that in nano-metals,[361, 364] the interaction of incident radiations

with the well distributed TNTs could indeed impact the corresponding absorption around the bandgap edge, rendering a promising application in optical sensors.

It has been observed that, when the internal distance (d_S) between two TiO_2 nanotubes becomes smaller, the near-field coupling oscillation strength produces a strong confinement of the local electric field which enhances the spectroscopic signals as showing in Figure 4-12. Such impact from the distributing of the nanotubes is consistent with the observations in nano-metallic particle arrays. Jain *et al.*[365] derived a plasmon ruler equation for Au nanoparticle arrays and explained that within the dipolar coupling model, the distance decay of plasmon coupling was independent of the nanoparticle shape, the metal type and the medium of dielectric constant. To make a further analysis, the curve for the near field intensity enhancements ($|E_x^2|$) at the top surface of the nanotubes versus the distance of the nanotubes is plotted.[366, 367] The $|E_x^2|$ presents a fast decay with the increase of the gap of the nanotubes, indicating that the coupling of the electric field becomes weak when the nanotube distribution is tuned sparse. Such weakened coupling could be responsible for the corresponding bandgap shift of TNTs.

As to the bandgap shift of TiO_2 nanotube arrays, Chang et al.[363] claim that such bandgap shift could be realized by adjusting the wall thicknesses of TiO_2 nanotubes in the range of 2.7 nm to 37.8 nm, which is based on the conventional quantum confinement effect. However, the results indicate that the bandgap shift can also be acquired only by adjusting the diameters and the distances between nanotubes, even these parameters are larger than the Bohr radius of TiO_2 and quantum effects are not responsible for this observation, since the thicknesses of these nanotubes are in the same value. This specific optical bandgap shift can be attributed to the interaction of the incident radiations with the highly ordered nanostructure arrays and the tunability of bandgap is related to the strength of the near-field enhancement of light. Thus, the results broaden the tuning range of optical

properties of nanostructure arrays and the according possibilities for photo-electronic applications.

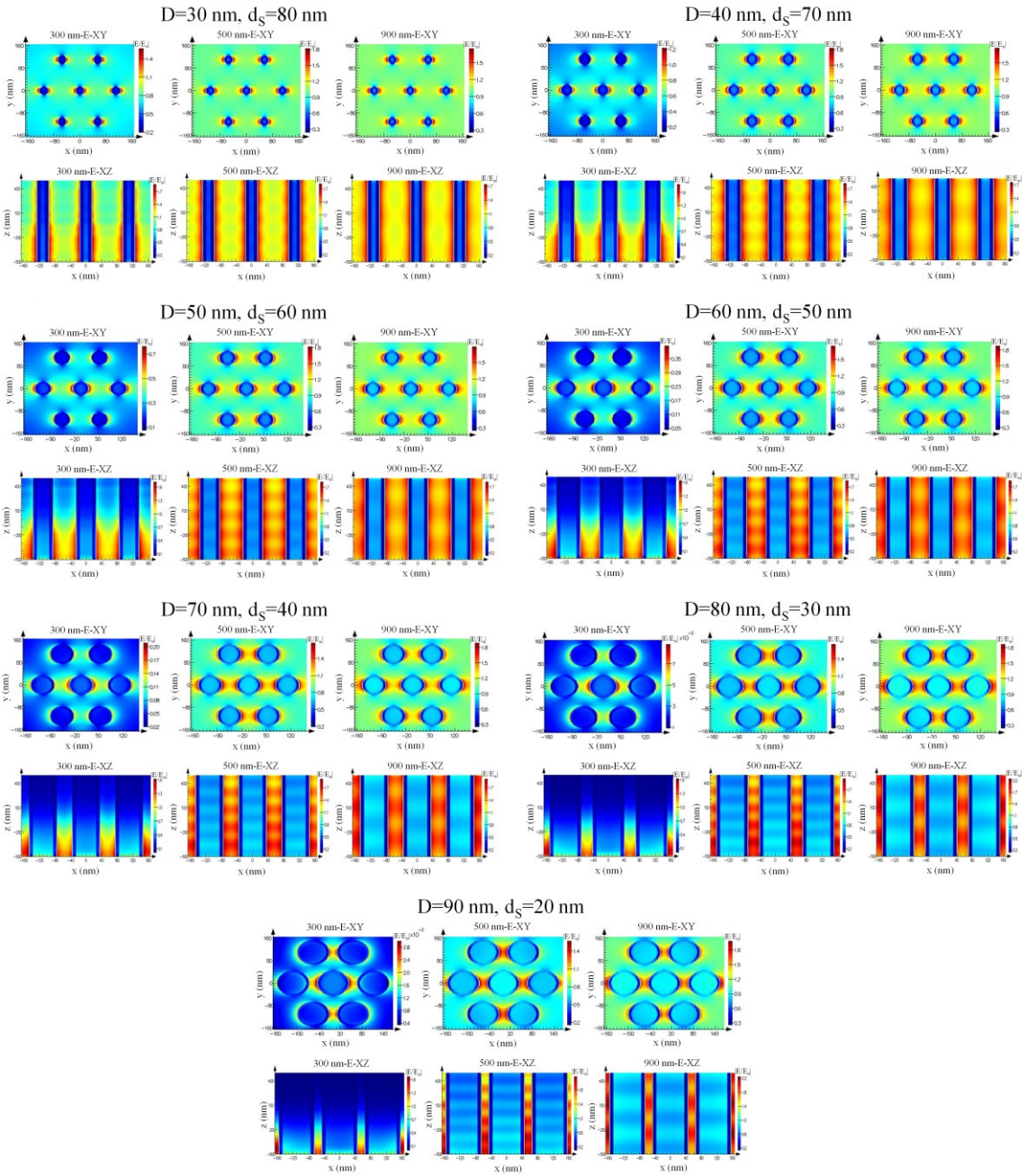

Figure 4–11. FDTD simulation of E-field amplitude distribution under illumination at 300 nm, 500 nm and 900 nm, respectively, showing the top and the cross-sectional views of: S1=(D=30 nm, d_S=80 nm), S2=(D=40 nm, d_S=70 nm), S3=(D=50 nm, d_S=60 nm), S4=(D=60 nm, d_S=50 nm) S5=(D=70 nm, d_S=40 nm), S6=(D=80 nm, d_S=30 nm) and S7=(D=90 nm, d_S=20 nm).

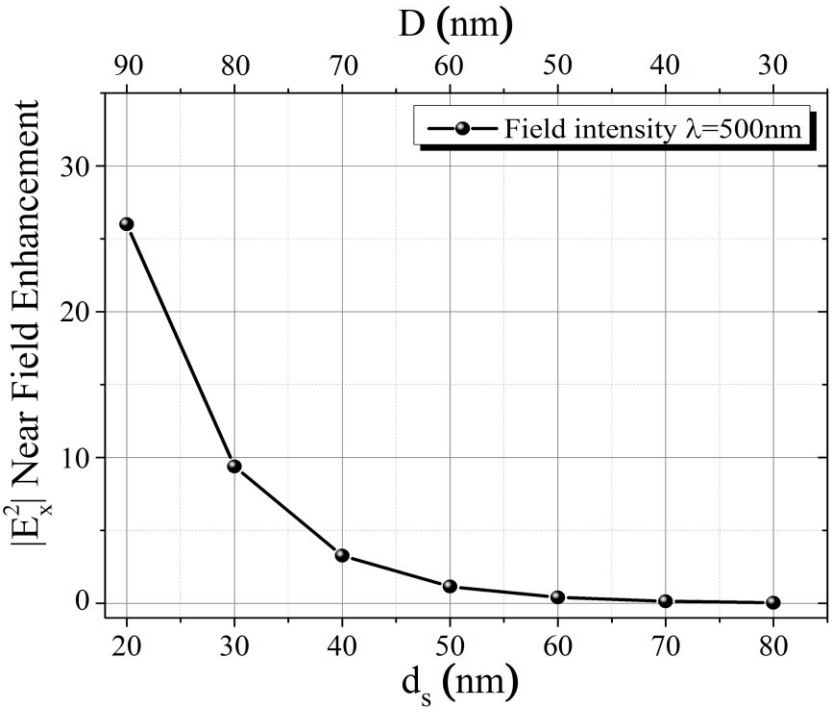

Figure 4–12. FDTD calculated $\left|\mathbf{E_x^2}\right|$ enhancement at the top surface of TNTs as a function of internal distance of TiO_2 nanotube under 500 nm illumination.

4.4. Conclusions

Well-ordered TiO_2 nanotube arrays have successfully prepared by combining ALD technology with AAO template. The crystalline quality of deposited TiO_2 was enhanced using a two-step ALD procedure. By tuning the nanotube arrays with different diameters and internal distances but the same wall thickness, the resulted absorption band edge showed a red shift with the decrease of the internal distances. This phenomenon was proven by the FDTD simulation. The calculated decay constant of the optical bandgap over the ratio of nanotube diameter/internal distance demonstrated that the tunability of bandgap was related to the strength of the near-field enhancement of light. Thereby, these results supply a new perspective for the optical bandgap shift of semiconductor nanostructure arrays.

5. CdTe/TiO_2 Core-Shell Nanowire Arrays

5.1. Introduction

As an application of the previous chapter, this chapter will include preparing of well-ordered CdTe/TiO_2 nanorod arrays by using the AAO template in a combination with electrodeposition and atomic layer deposition techniques. The resultant structure possesses a decent crystal quality, beneficial for improving the performance of the corresponding photoelectrochemical electrodes. The structural optimized photoanode and solar cell based on CdTe/TiO_2 core-shell nanowire arrays.

5.2. Experimental Section

5.2.1. Preparation of AAO template

High ordered pores of AAO templates with different diameters were prepared by using high-purity (99.99%) aluminum foil with a thickness of 0.2 mm according to the previous reports[40, 87, 368-370]. Al foils were first deeply cleaned with acetone, ethanol and DI water respectively before the electrochemical polishing process in a 1:7 solution of perchloric acid and ethanol. The anodization of the Al foil was performed under a constant voltage of 40 V in 0.3 M oxalic acid at 7 ˚C for 7 h and 30 min for first and second anodization, respectively. The obtained AAO templates were put in 5 wt % H_3PO_4 solution at 30 ˚C to realize desirable pore diameter. After 20, 30 and 40 min of the pore-widening process, the resulted AAO template presented a pore diameter of about 60, 75 and 90 nm, respectively.

5.2.2. TiO_2 deposition

A smooth layer of TiO_2 was deposited using a Picosun SUNALETM R150 ALD System. The AAO template was placed in the chamber of the ALD system. Two-step ALD procedure[368] was adopted to deposit 200 cycles of TiO_2 by using $TiCl_4$ and H_2O as Ti and O sources under 25 ˚C. The typical pulse/purge time for $TiCl_4$ and H_2O precursors was 0.1 s/5 s and the carrier gas flow was set at 200 sccm.

5.2.3. CdTe deposition

After the continuous layer of TiO_2 was deposited on the entire surface of the structure including the top (AAO) and the bottom (Al) surfaces, the working electrode (TiO_2/AAO) was fixed in the prepared cell to contact the electrolyte from the TiO_2/AAO side. Using conventional three-electrode configuration with 1 cm^2 of a Pt foil as a counter electrode and an Ag/AgCl (3 M NaCl) as a reference electrode, the deposition was performed at 85 ˚C in a mixed solution (1 M $CdSO_4.8/3H_2O$ and 300 μM TeO_2) with the pH being adjusted to 2.0 using dilute H_2SO_4. In order to eliminate any photoinduced effects during the growth of CdTe, the vessel was covered by a light resistant box.[371, 372] The electrolyte was agitated at 300 rpm with a magnetic stirring unit. By using BioLogic SP 150 Potentiostat, the CdTe layer was deposited at –0.37 V. The deposition time was 10, 20 and 30 min, respectively.

5.2.4. Analyzing the HRTEM of CdTe/TiO_2

By using Gatan-DigitalMicrograph software 2015 version 2.32.888.0, two masks are applied at the peaks inside the FFT pattern of the interface of CdTe/TiO_2. One is to mark the CdTe region and the second for TiO_2 region and then the inverse FFT and the obtain images for each region alone is performed.

5.2.5. Photoelectrochemically water splitting device assembling

To finalize the PEC water splitting device, 30 nm thick gold layer was deposited onto CdTe by electron beam deposition (Kurt J. Lesker PVD225) with deposition rate 0.2 Å/s, and then a thick layer of Ni was deposited electrochemically to support the sample during the photoelectrochemical experiment. The electrodeposition of Ni was carried out in Ni plating solution including 8.41×10^{-2} M $NiCl_2$, 1.59 M $(H_2NSO_3)_2.4H_2O$ and 0.33 M H_3BO_3 under a typical current density 10 mA cm^{-2}. Thereafter, the rest of Al in the backside was removed using a mixture solution of $CuCl_2$ (90 wt %) + HCl (10 wt %). Finally, the AAO template was selectively removed by immersing the samples in a 5 wt% H_3PO_4 solution for 3 h.[32, 35, 369]

5.2.6. Characterization and photoelectrochemical performance measurement

Surface morphologies of the prepared samples were examined by a scanning electron microscope (SEM, Hitachi S4800) and a transmission electron microscope (TEM, Philips TECNAI). X-ray diffraction (XRD, Siemens D5000) was utilized to analyze the crystal structure of the $CdTe/TiO_2$ core-shell nanowire arrays. The UV−vis spectrometer (Varian) was adapted to measure the absorption characteristic of the $CdTe/TiO_2$ core-shell nanowire arrays. The photoelectrochemical performance of the electrodes was evaluated in a three-electrode configuration using BioLogic SP 150 Potentiostat. The electrolyte was 1 M NaOH. The reference electrode was Ag/AgCl in 3 M KCl and a 1 cm^2 Pt foil was used as a counter electrode. The light source (Oriel solar simulator, 300 W Xe lamp, AM 1.5 global filter) was calibrated to 1 sun (100 mW cm^{-2}) by a Si photodiode (Model 818, Newport). The IPCE was measured without applying bias using QEPVSI-b Quantum Efficiency Measurement System (Newport).

5.2.7. Al doped ZnO (AZO) layer deposition

The AZO layer was deposited as a transparent conductive layer on TiO_2 side of the CdTe/TiO_2 nanoheterostructure arrays. the enhanced procedure were used for AZO deposition by ALD at 200 °C including in wich one typical growth cycle consists of: DEZn-N_2 purge-H_2O-N_2 purge (20 cycle ZnO)-TMAl-N_2 purge-H_2O-N_2 purge. The growth rate of ZnO and Al_2O_3 is about 1.0 nm per cycle. After 30 cycles, the CdTe/TiO_2 nanoheterostructure arrays were totally covered by AZO.

5.2.8. Performance of CdTe/TiO_2 nanoheterostructure solar cell

The open circuit performance of the CdTe/TiO_2 nanoheterostructure arrays is evaluated using BioLogic SP 150 Potentiostat. The light source (Oriel solar simulator, 300 W Xe lamp, AM 1.5 global filter) was calibrated to 1 sun (100 mW cm^{-2}) by a Si photodiode (Model 818, Newport). The external quantum efficiency is measured without applying bias voltage by using QEPVSI-b Quantum Efficiency Measurement System (Newport).

5.2.9. Impedance spectra of CdTe/TiO_2 nanoheterostructure arrays

The impedance spectroscopy measurements were performed using CdTe/TiO_2 nanoheterostructure arrays with variable diameters of 60, 75 and 90 nm. The measurements were carried out in dark condition in 1 M NaOH solution at zero potential bias over a frequency range from 1 MHz to 200 Hz. The impedance data are analyzed by EC-Lab® Express v5.53.

5.3. Results and Discussion

Figure 5-1 demonstrates the schematic outline of the fabrication stages of CdTe/TiO_2 nanoheterostructure arrays. Based on highly ordered AAO template (Figure 5-2a), TiO_2 nanotube arrays with desirable wall thickness (9 nm) could be achieved by two-step of

atomic layer deposition (Figure 5-2b). Thereafter the CdTe as the active material for photon absorption is selected, to combine together with TiO_2 as heterojunction in the highly-ordered nanostructure arrays (Figure 5-2c). The resulting freestanding CdTe/TiO_2 nanoheterostructure arrays show a vertical dimension around 1.5 µm after selectively removing the AAO template as depicted in Figure 5-2d, e. The surface of the arrays of CdTe/TiO_2 nanoheterostructure with various diameters (D1=60 nm, D2=75 nm and D3= 90 nm) is demonstrated to be quite smooth by Figure 5-3.

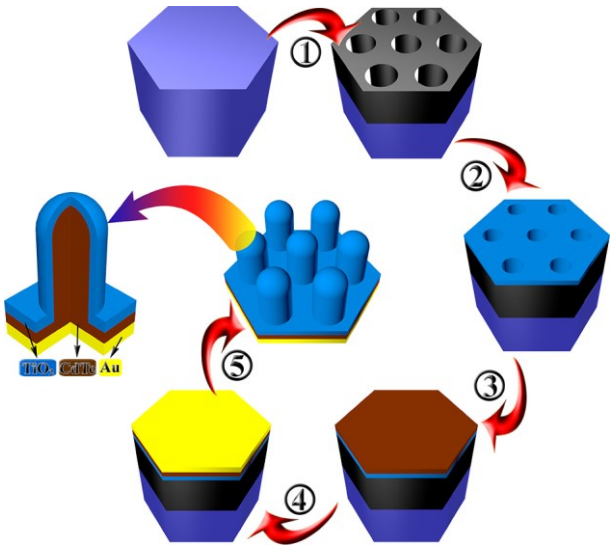

Figure 5–1. Schematic outline of the fabrication processes of CdTe/TiO_2 heteronanostructure (processes 1 to 5 are anodization of Al foil, TiO_2 deposition by ALD, electrochemical deposition of CdTe, Au deposition by PVD, removing the rest of Al in the backside and AAO template).

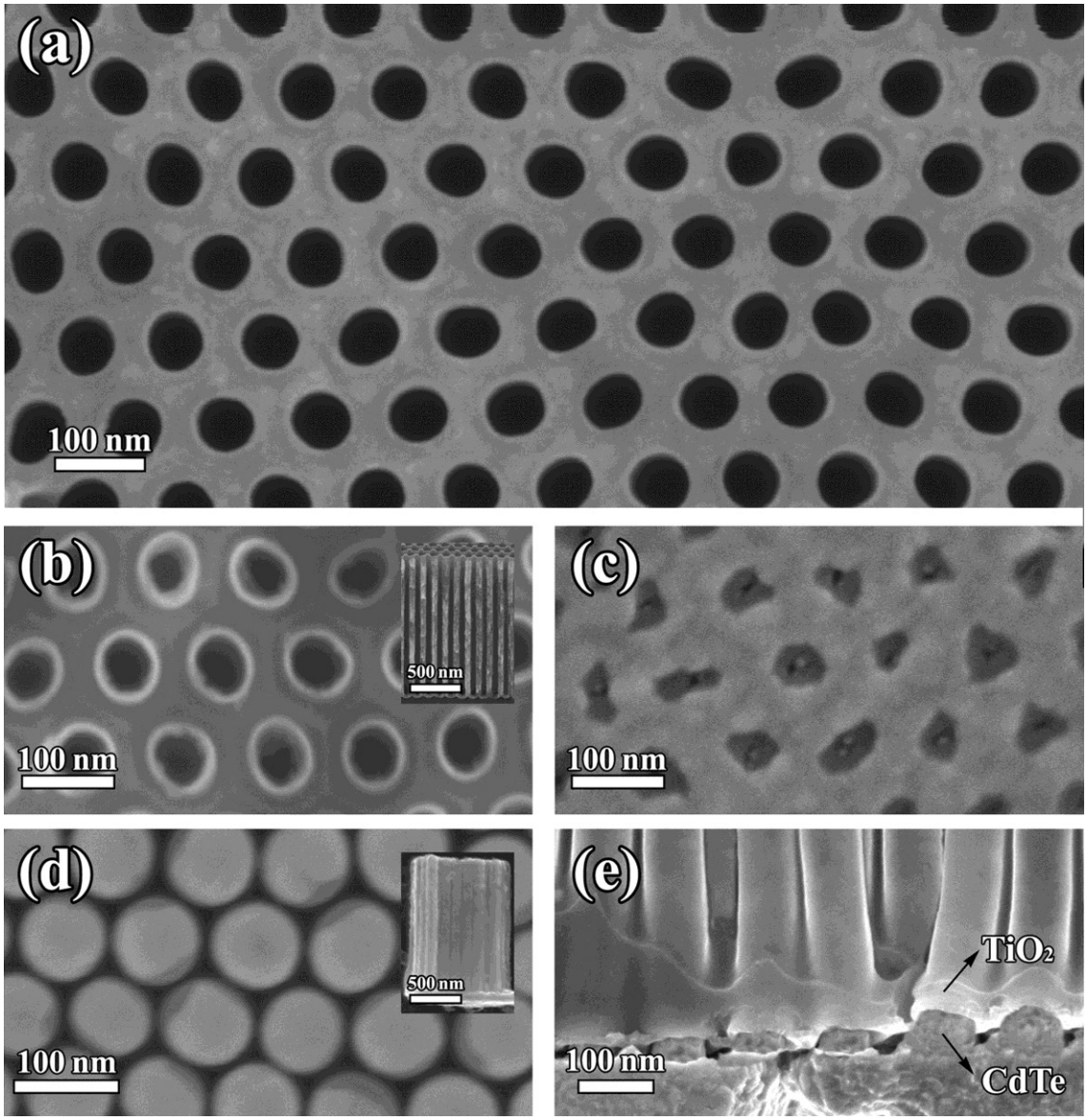

Figure 5–2. SEM images of the preparing process. (a) The prepared AAO after widening process. (b) TiO_2 deposition by ALD (the surface was etched for more clarity), the inset cross-sectional view shows the length of TiO_2 nanotube arrays around 1.5 μm. (c) Electrochemical deposition of CdTe. (d) Top view of the CdTe/TiO_2 heteronanostructure arrays after removing the AAO template, the inset shows the cross-sectional image of the freestanding CdTe/TiO_2 heteronanostructure arrays. (e) Cross-sectional view of the edge after breaking the sample to expose the both material as core-shell nanostructure.

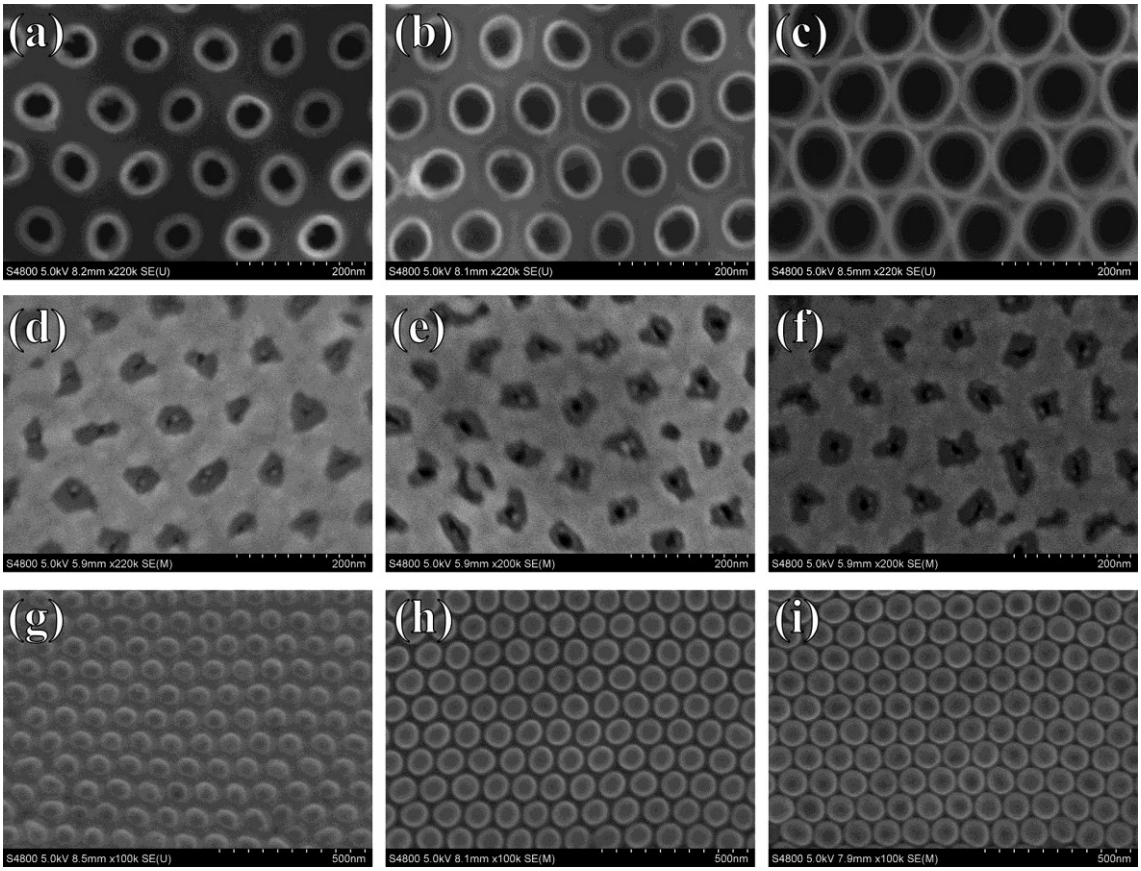

Figure 5–3. Scanning electron microscopy of the prepared samples, (a-c) 200 cycles of TiO_2 deposition by ALD, for more clarity the surface of TiO_2 layer was etched by Ar ion milling for 2 min. (d-f) Electrochemical deposition of CdTe for 10, 20 and 30 min, respectively. (g-i) The top view of the CdTe/TiO_2 nanoheterostructure with diameter around 60, 75 and 90 nm, respectively.

In the prepared CdTe/TiO_2 heterojunction, the high crystallinity of TiO_2 and CdTe can reduce the defects at the interface and inside the materials, thus leading to a minimized possibility of charge recombination for improvement in photoelectrochemical performance. In order to investigate the structure characterization of the CdTe/TiO_2, TEM measurements were performed and the according image is shown in Figure 5-4a, where the core-shell structure of CdTe/TiO_2 can be distinctively observed. The diameter of CdTe core is gauged as 72 nm and that of the TiO_2 shell is measured as 9 nm. The HRTEM image in Figure 5-4b gives zoom-in image at the interface of CdTe and TiO_2, where two sets of crystal lattices with an obvious boundary could be easily discerned. The estimated spacing for one set of lattices is about 3.7 Å, which is close to the interplanar spacing of the (111) planes of

CdTe with zinc blende structure. Furthermore, the resolved spacing of the other set of lattices is about 3.5 Å, which is close to the interplanar spacing of the (101) planes of TiO_2 anatase structure. For more detail Figure 5-4c indicates the fast Fourier transform (FFT) calculation of the HRTEM (Figure 5-4b), the FFT pattern presents two sets of different crystal lattices which belong to TiO_2 (anatase) and CdTe (zinc blende), respectively, in good consistency with the results from HRTEM analyses.

The analyzing of HRTEM image in Figure 5-4b shows three different regions (patterns) and it is very clear that the region around the marked yellow line represents the interfacial layer between region A (TiO_2) and region B (CdTe). The thickness of the interfacial layer is around 0.5-1 nm. In the other side, the FFT pattern in the Figure 5-4 d, e can confirm that the regions A and B belong to TiO_2 and CdTe, respectively. Two masks are applied at the peaks inside the FFT pattern of the interface in Figure 5-4c. The first one is marked with blue circle and the second one is in red circle and then the inverse FFT was performed to obtain the images in the Figure 5-4f, g. By calculating the lattice space of the peaks in these figures (5-4f, g), the spacing of the first one is 3.5 Å and of the second one is 3.7 Å, these belong to TiO_2 (101) and CdTe (111) planes, respectively.

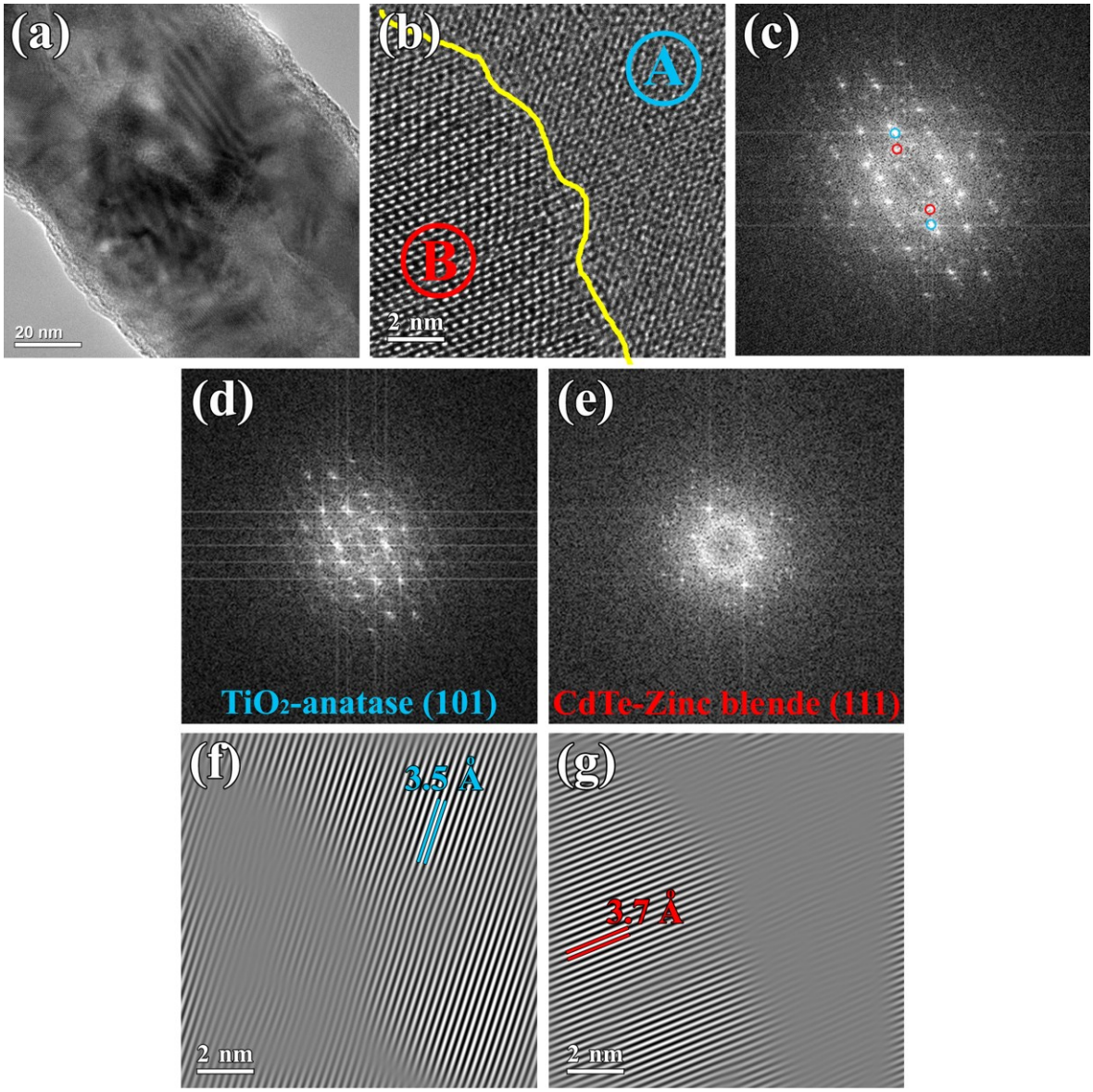

Figure 5–4. (a) TEM of a typical CdTe/TiO_2 heteronanostructure (D ≈ 90 nm) with HRTEM of the interface between CdTe and TiO_2 (top left) and fast-Fourier transforms of the interface between CdTe and TiO_2 (bottom right). (b) HRTEM showing the interfacial layer between TiO_2 and CdTe. (c) The FFT pattern of entire image (b). (d) The FFT pattern of area A in image (b), displaying the crystalline structure of the TiO_2. (e) The FFT pattern of area B in image (b), displaying the crystalline structure of the CdTe. (f, g) The inverse FFT images calculated from the peaks in the image (c).

To identify each element separately, Figure 5-5a shows the line-scan profile of energy-dispersive X-ray spectroscopy (EDX) from the cross-section of a typical CdTe/TiO_2 nanoheterostructure made from AAO template with a pore size of 90 nm. It is very clear that a core-shell nanostructure consisting of TiO_2 nanotube as the shell and a CdTe nanowire as the core, has been realized. Besides the located line-scan profile shows the

exact dimension (~thickness) of each material, accordingly the thicknesses of TiO_2 and CdTe are around 9 and 72 nm respectively. Furthermore, the resulting intensities of Cd and Te suggest that the composition ratio of both materials is around 50% in an excellent agreement with the reported results of a similar deposition technique of CdTe.[372] Figure 5-5b shows the X-ray diffraction (XRD) pattern of the prepared core-shell nanostructure arrays after removing the AAO template. The TiO_2 nanotube belongs to anatase phase and the highest diffraction peak at 25.3° can be indexed to face (101). The highest diffraction peak of CdTe nanowire is located at 24° that can be assigned to face (111). These high intensities of the XRD patterns suggest that the both materials are highly crystalline.

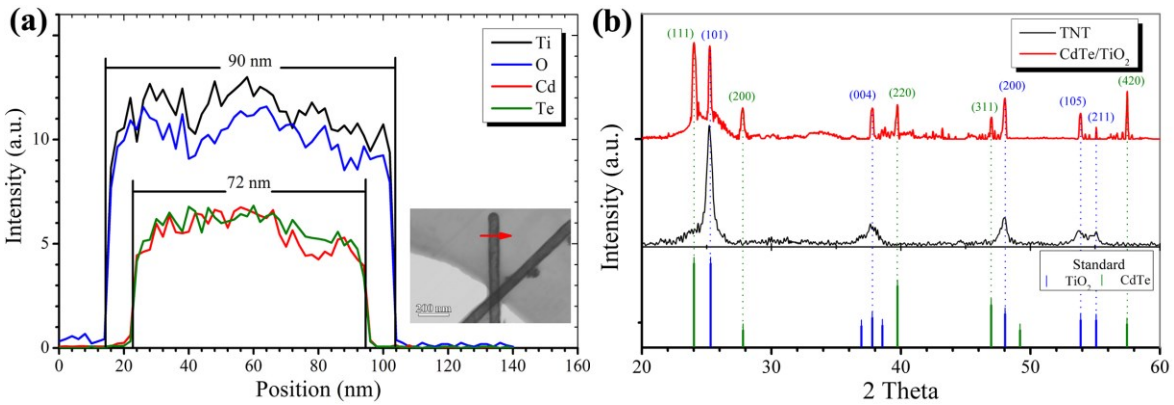

Figure 5–5. (a) Line-scan profile of individual CdTe/TiO_2 heteronanostructure as shown in the inset image. (b) XRD patterns for TiO_2 nanotube and CdTe/TiO_2 heteronanostructure arrays with standard bulk diffraction peaks for TiO_2 (anatase) and CdTe (zinc blende).

Figure 5-6 exhibits the absorption spectra of the as-grown nanostructure arrays with different diameters. All these spectra present an absorption onset beyond 800 nm, indicating the presence of CdTe that enhances the absorption of the system in the visible range. By investigating the difference of these spectra, It can be observed that with the increase in the diameters, this nanostructure array presents an improved absorption

capability by showing a redshift of the absorption onset and enhanced intensities, in good agreement with the recorded results in chapter 4.[75]

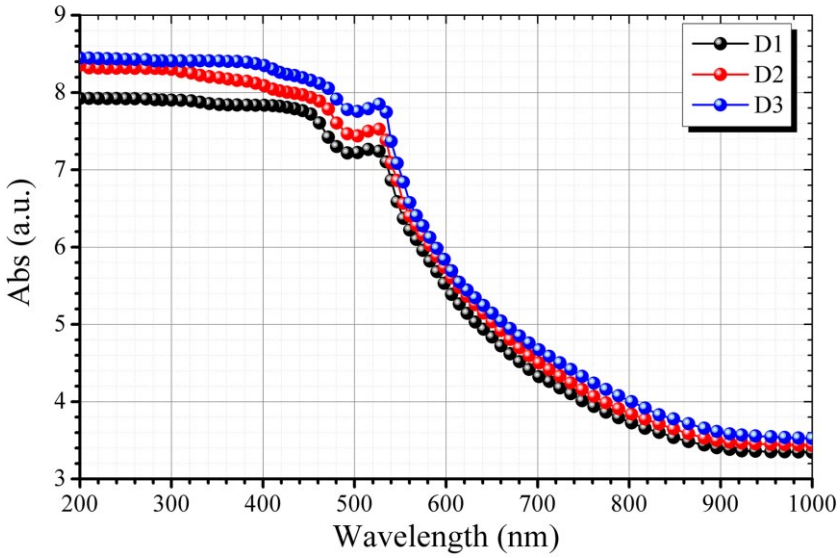

Figure 5–6. Absorbance spectra of CdTe/TiO_2 core-shell nanowire arrays with different diameters.

Consequently, the incident photon-to-electron efficiency (IPCE) spectra of the photoelectrodes equipped with these nanostructure arrays shows a prominent photocurrent signal in the visible range (Figure 5-7a), which matches the absorption region of the according structures. This indicates that the presence of CdTe contributes to the improvement in PEC performance. For reference, the IPCE spectrum is also measured for bare TiO_2 electrode, which shows an ignorable signal in the visible region, due to the large bandgap. To be noted, the CdTe/TiO_2 electrode shows a remarkable enhancement in IPCE with the increase in diameter, consistent with the absorption spectra.

Figure 5-7b shows the photocurrent density as a function the applied potential to the reversible hydrogen electrode (RHE) for CdTe/TiO_2 electrodes under white light illumination (AM 1.5G, 100 mW cm^{-2}) was calculated from:[295]

$$E_{RHE} = E_{Ag/AgCl} + E^{\circ}_{Ag/AgCl} + 0.059\,pH \qquad (5\text{-}1)$$

where the E_{RHE} is the converted applied potential versus RHE, the $E_{Ag/AgCl}$ is the measured applied potential versus the Ag/AgCl reference, electrode, and the $E^{\circ}_{Ag/AgCl}$ is the standard potential of Ag/AgCl reference at 25 °C (0.1976 V) and pH for 1 M NaOH is 13.6.

In comparison with the bare TiO_2 electrode, all the composite electrodes deliver a dramatic improvement in photocurrent that also exhibits an increasing feature with the enlargement in the diameter of the nanostructures. The photocurrent could be increased more than 70% in the entire potential scanning region when the diameter of CdTe/TiO_2 is manipulated from 60 nm to 90 nm. Consequently, the highest photocurrent has been realized was 1.16 mA cm^{-2} for sample D_3, ~10 times of the bare TiO_2 electrode. Figure 5-7c confirms these results by current response under chopped illumination, suggesting that the light-driven water splitting at 0 V vs. RHE is conceivable for CdTe/TiO_2 nanoheterostructure. Furthermore, the photoconversion efficiency (η) of PEC electrodes with an applied bias, which is so-called applied bias photon-to-current efficiency (ABPE), is calculated from J-V data using the following equation:[61, 373-375]

$$\eta = J_{ph}(1.23 - V_{app})/P_{in} \quad (5\text{-}2)$$

where J_{ph} (mA cm^{-2}) is the measured photocurrent density, V_{app} (V) is the applied bias between the photoanode and photocathode, and P_{in} (mW cm^{-2}) is the power density incident light intensity (here is 100 mW cm^{-2}). The plotted photoconversion efficiency as a function of the V vs. RHE is shown in Figure 5-7d, where the sample D1 exhibits photoconversion efficiency about 0.49 % at 0.15 V vs. RHE. Significantly, samples D2 and D3 achieve higher photoconversion efficiency about 0.68 % at 0.13 V vs. RHE and 0.85 % at 0.09 V vs. RHE. These results are consistent with the analyses on J-V curves and IPCE spectra.

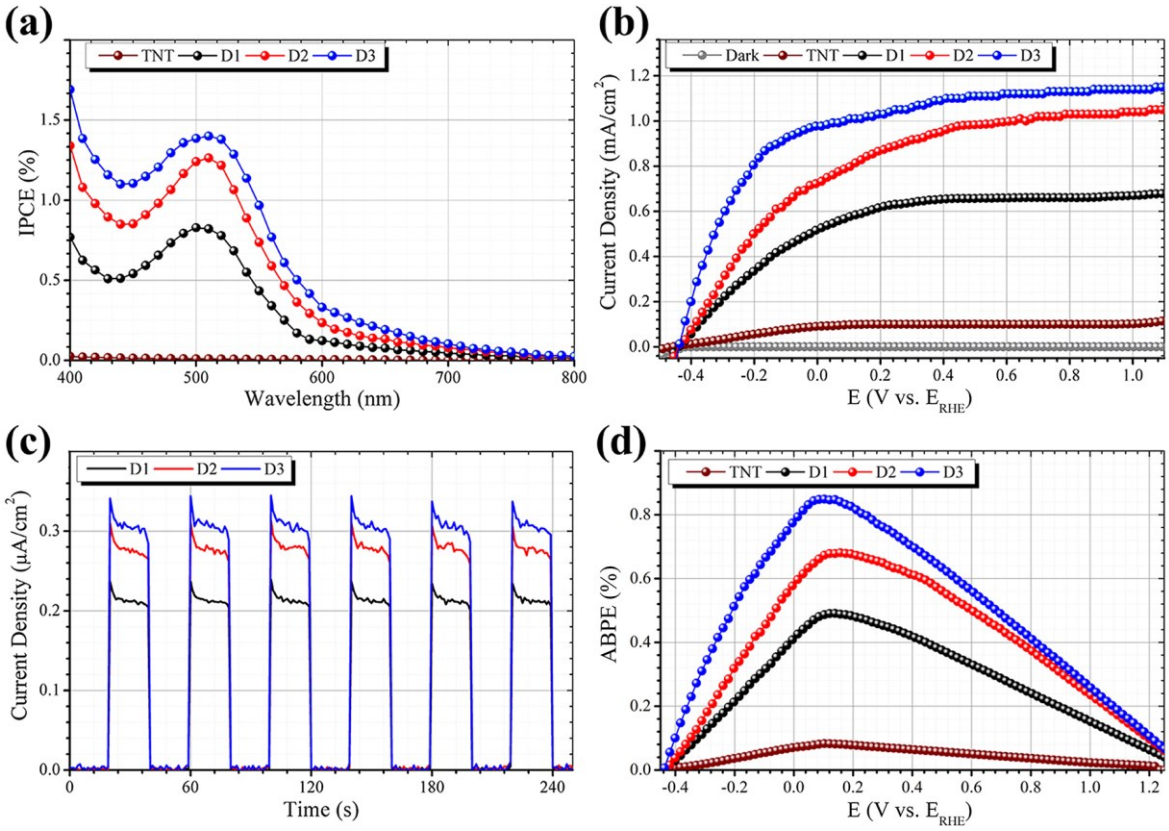

Figure 5–7. (a) IPCE spectra of the prepared samples (without applying external bias). (b) Photocurrent densities of CdTe/TiO_2 heteronanostructure arrays for the prepared samples under white light illumination (AM 1.5G, 100 mW cm^{-2}) from −0.5 to 1.0 V versus RHE. (c) Current density of externally short-circuited of the prepared samples measured at zero bias voltage under the same illumination conditions as at (b) with using chopped light exposure. (d) The calculated ABPE for the prepared samples, as a function of applied potential vs. RHE.

In order to get a full understanding of the impact of the geometrical factors on the device performance, electrochemical impedance spectra were measured and the related Nyquist plots covering the frequency of 1 MHz to 200 Hz at the bias of 0 V vs. Ag/AgCl are given in Figure 5-8. These plots demonstrate that the systematic resistance could be obviously reduced by increasing the diameters of the according nanostructures, due to the fact that the semicircle in a Nyquist plot at high frequencies is characteristic of the charge transfer process and the semicircle diameter is directly proportional to the charge transfer resistance.

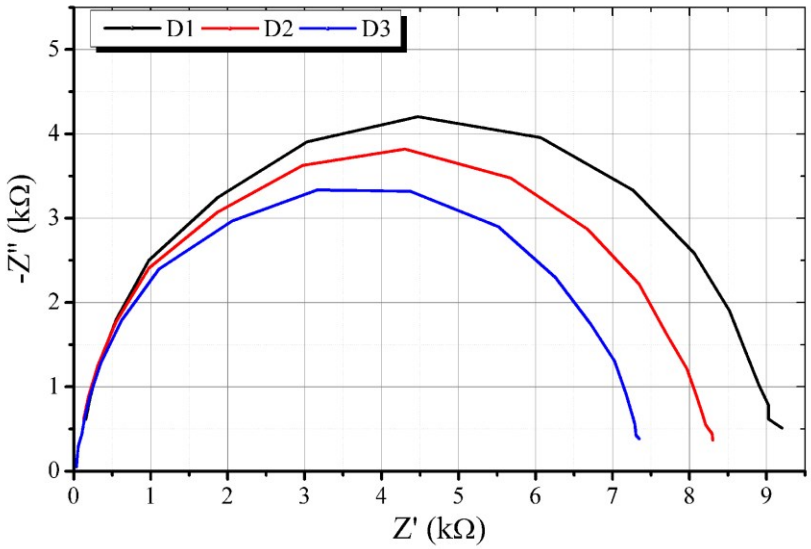

Figure 5–8. Electrochemical impedance spectra of CdTe/TiO_2 nanoheterostructure arrays with different diameters (D1=60 nm, D2=75 nm and D3=90 nm).

This particular heterojunction design is of similarity to the configuration of Si/Fe_2O_3 and Si/TiO_2 heterojunctions.[58, 376] All these structures show a typical semiconductor–semiconductor configuration, as illustrated in Figure 5-9. The shell material, TiO_2, is designed as a typical photoelectrode that absorbs short-wavelength photons for water photooxidation and the core CdTe (could be consider as n-CdTe according to the similar deposition conditions)[372] is to absorb long-wavelength photons for water reduction. The interface of CdTe would behave as the recombination centers for the excited holes in CdTe and the electrons in TiO_2, which is helpful for keeping the electrode with high photocatalytic activities due to the fact the reverse current of electrons in CdTe and that of holes in TiO_2 are both energetically prohibited. Moreover, the Z-scheme (all-solid-state) architecture of is beneficial for reducing the onset potential of the composite electrode.[61, 63] The TiO_2 shell is also good for preventing CdTe core from corrosion by avoiding the direct contact of CdTe with the electrolyte.[377]

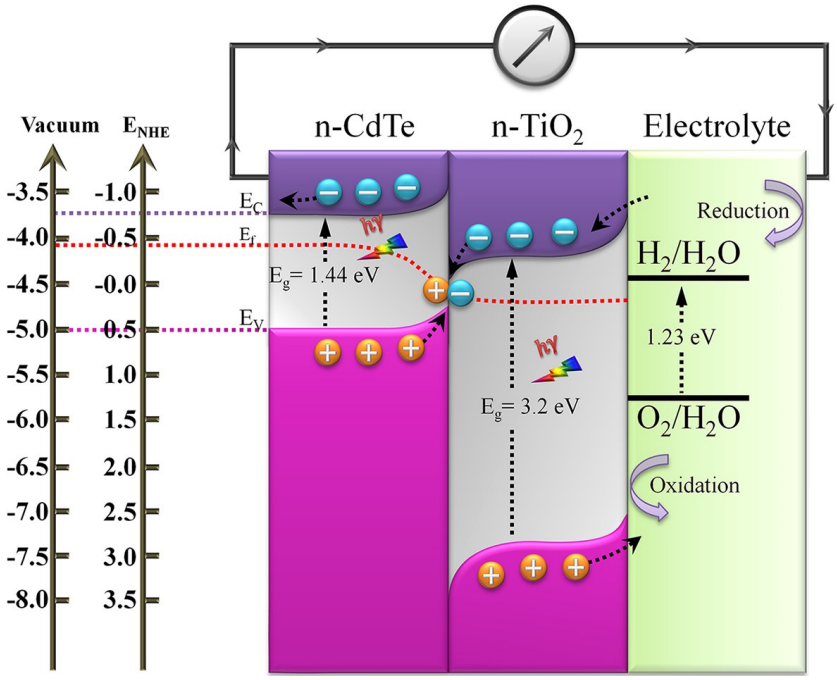

Figure 5–9. Schematic outline of the charge carrier transfer at $CdTe/TiO_2$ heteronanostructure interface as a Z-scheme model under a visible light irradiation.

Furthermore, the $CdTe/TiO_2$ nanostructure arrays is also used to construct solid-state solar cells with the structure of $Au/CdTe/TiO_2/AZO$ and the corresponding performance is shown in Figure 5-10. The J-V curves show a decent short circuit current that could be improved from 7.612 to 9.374 mA cm^{-2} when the diameter of nanotube enlarged from 60 nm to 90 nm (Figure 5-10a). The external quantum efficiency (EQE) spectra in Figure 5-10b show a similar profile with those in the PEC measurement, indicating that $CdTe/TiO_2$ behaves as the core component in the solid-state solar cells.

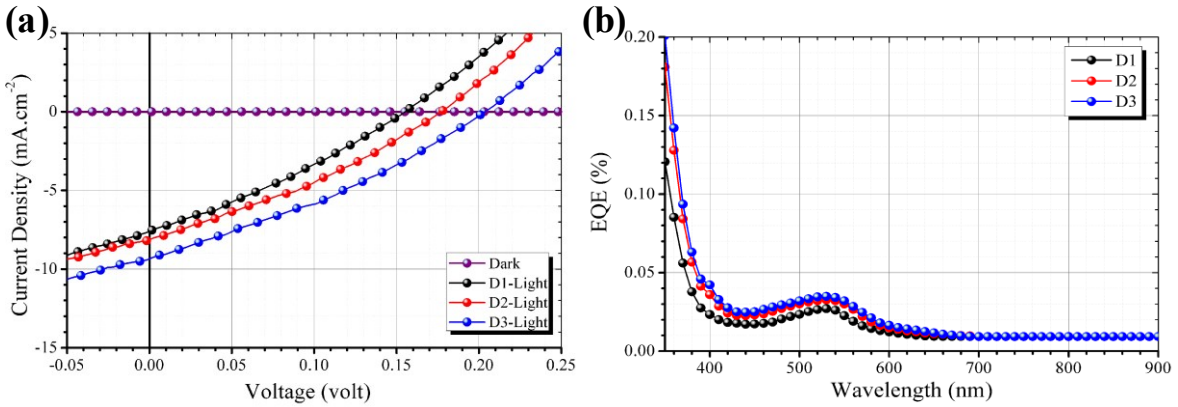

Figure 5–10. (a) J–V characteristics under white light illumination (AM 1.5G, 100 mW cm^{-2}) of CdTe/TiO_2 nanoheterostructure arrays. (b) The external quantum efficiency of CdTe/TiO_2 nanoheterostructure at zero bias voltage.

5.4. Conclusion

In conclusion, well-ordered core/shell structure nanostructure arrays, CdTe/TiO_2, were fabricated by the convenient AAO template-directed method and applied to solar energy conversion. Extensive data show that the enlargement in the diameters of the nanostructure arrays could not only improve the absorption efficiency of the structure but also could reduce the resistance of the system; both are beneficial to the performance improvement. Thus, these results provide a good nanostructure to the community of water splitting and solar cells.

6. Novel TiO_2/Si Heterostructure Arrays

6.1. Introduction

In this chapter, as a unique configuration for solar energy applications, new heterostructures have been developed. Four different nanostructure arrays were fabricated from TiO_2/Si heterojunction and investigated their potential applications depending on the performance photoelectrochemical water splitting and solid-state solar cell.

6.2. Experimental Section

6.2.1. C-UTAM preparation

Ti/Al (8 nm and 1.2 μm, respectively) layer was deposited on 4-inch p-Si wafer (100) by using PVD-E-beam Cluster (Ardenne LES 250) with a deposition rate of 0.3 nm s^{-1}. Ordered C-UTAM template was prepared by two-step anodization of the obtained Al thin film under a potential of 40 V in 0.3 M oxalic acid at 7 ºC for 20 min for first and 15 min for second anodization, respectively, using lab-made cell (Figure 3-1a). The obtained UTAM templates with thickness around 500 nm were immersed in 5 wt. % H_3PO_4 solution at 30 ºC to realize desirable pore-diameter. After 30 min of the pore-widening process (as described in Chapter 4), the resulted UTAM template has a pore diameter of about 70 nm. The B_L of the pores of the connected UTAM template and the deep etching of the Si through the pores of the UTAM template was carried out by using surface technology systems-advanced silicon etch system (STS Multiplex ASE) under standard condition (20 mTorr, Ar flow 20 sccm, 250 W ICP power and 90 W CCP power). 2 min and 30 min of etching process were applied for B_L and deep etching of the Si, respectively. The resulting

samples one UTAM/Si without barrier layer and the second UTAM/Si with the pores of Si below the pores of UTAM template were obtained.

6.2.2. Fabrication of TiO_2/Si heteronanostructures

The deposition of TiO_2 was conducted in a Picosun SUNALE^{TM} R150 ALD System. The prepared samples of UTAM /Si were placed in the chamber of the ALD system. Two-step ALD procedure was adapted to improve the crystallinity of TiO_2 (as described in Chapter 4).[75] Before removing the UTAM template, the surface layer of the TiO_2 was etched by inductively coupled plasma (ICP) using STS Multiplex ASE under a standard condition for 5 min. The removing process of the UTAM was achieved by immersing the samples in 5 wt. % H_3PO_4 solution at 30 ºC for 6 h. To separate the Si from the electrolyte in the photoelectrochemical experiment, 3 nm of TiO_2 was further deposited to cover the unprotected area of Si.

6.2.3. AZO layer deposition

AZO layer was deposited as a transparent conductive layer on TiO_2 side of the TiO_2/Si heteronanostructure arrays. According to similar procedure were used in chapter 5 for AZO deposition by ALD, 30 cycles of AZO deposition were utilized to cover the TiO_2/Si nanoheterostructure arrays.

6.2.4. Characterization and Measurement

Surface morphologies of the prepared samples are examined by a scanning electron microscope (SEM, Hitachi S4800) and a transmission electron microscope (TEM, Philips TECNAI). X-ray diffraction (XRD, Siemens D5000) was utilized to analyze the crystal structure of the TiO_2 nanotube arrays.

The photoelectrochemical performance of the electrodes in a three-electrode configuration performance are evaluated using BioLogic SP 150 Potentiostat. The electrolyte is 1 M NaOH (pH = 13.4). The reference electrode was Ag/AgCl in 3 M KCl and a 1 cm^2 Pt foil as a counter electrode. The light source (Oriel solar simulator, 300 W Xe lamp, AM 1.5 global filter) was calibrated to 1 sun (100 mW cm^{-2}) by a Si photodiode (Model 818, Newport). The IPCE is measured without applying bias using QEPVSI-b Quantum Efficiency Measurement System (Newport).

6.2.5. Performance of TiO_2/Si nanoheterostructure solar cell

The open circuit performance of the TiO_2/Si nanoheterostructure arrays is evaluated using BioLogic SP 150 Potentiostat. The light source (Oriel solar simulator, 300 W Xe lamp, AM 1.5 global filter) was calibrated to 1 sun (100 mW cm^{-2}) by a Si photodiode (Model 818, Newport). The external quantum efficiency is measured without applying bias voltage by using QEPVSI-b Quantum Efficiency Measurement System (Newport).

6.2.6. FDTD Simulation

A commercial FDTD simulation package (Lumerical FDTD Solutions Inc. 8.9) is used for calculating the cross-sectional electromagnetic wave distributions of TNTs⫫Si, TNTs⫽Si, TNWs⊥Si, TNWs┼Si heterojunctions. The parameters of these heteronanostructure arrays are derived from the SEM image for the simulation.

6.3. Results and Discussion

6.3.1. Fabrication strategy

Template-directed method is a very efficient way to construct functional nanostructures for device applications.[26, 37, 378] For the fabrication of TiO_2/Si

heteronanostructures, C-UTAM was used as template and was assisted with inductively coupled plasma (ICP) etching and ALD process. The fabrication procedure is illustrated in Figure 6-1. UTAM was firstly prepared by anodizing an evaporated aluminum layer on 4-inch p-type (0.01-0.02 Ω cm) Si wafer. After anodization, the barrier layer of C-UTAM was selectively removed through ICP etching process. By precisely controlling the time of ICP etching process, the barrier layer of C-UTAM was totally removed to from through-hole UTAM on Si wafer. Furthermore, the increasing of the ICP etching time results in etching of Si to produce a combined structure of UTAM and Si nanopores on Si substrate.

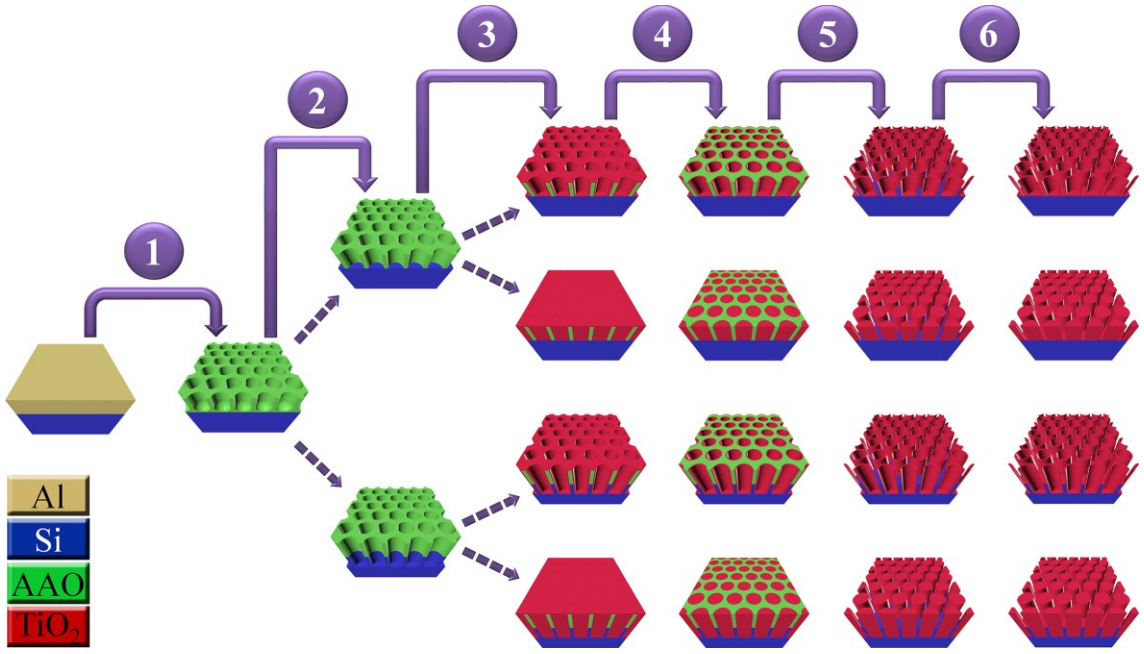

Figure 6–1. Schematic outline of the fabrication processes of TNTs⫫Si, TNTs⫴Si, TNWs⊥Si and TNWs┼Si heteronanostructures: 1) Anodization of Al film on Si; 2) ICP etching of the B_L and Si through the pores of UTAM; 3) ALD deposition of TiO_2; 4) ICP etching to remove the surface layer of TiO_2; 5) Removal of UTAM; 6) ALD deposition of the protective TiO_2 layer.

With this fabrication strategy, all the structural parameters can be easily controlled: the thickness of UTAM depend on the thickness of evaporated aluminum layer; the pore diameter of UTAM relates to the anodization time and wet-chemical etching process; the pore diameter and depth of Si nanopores depend on the diameter of UTAM and the ICP

etching time, respectively. As a result, the structural parameters of the as-prepared TiO_2/Si heteronanostructures should also be able to be precisely tuned, which will benefit to optimizing the photocatalytic performance of TiO_2/Si heteronanostructures. For the fabrication of TiO_2/Si heteronanostructures, the two-step ALD procedure was adopted to deposit TiO_2 into UTAM as well as UTAM/Si combined nanopores (see also chapter 4).[75] This two-step ALD procedure ensures to obtain highly crystalline TiO_2 nanotubes and nanowires since a highly crystalline structure is considered to be helpful to improve the photocatalytic properties of TiO_2. To isolate TiO_2 nanotubes or nanowires from UTAM, the UTAM was removed by wet-chemical etching process after the removal of the top TiO_2 layer by ICP etching. After that, another thin TiO_2 layer (3 nm) was deposited using ALD for the purpose to separate the bare Si surface from the electrolyte. The thin TiO_2 layer could effectively avoid photocorrosion of Si when immersed into solution or the short contact with conductive layer. Finally, four different kinds of TiO_2/Si heteronanostructures were obtained: vertically aligned TiO_2 nanotubes attached onto Si substrate (depicted as TNTs⊥Si), nanotubes embedded into Si substrate (depicted as TNTs╫Si), nanowires attached onto Si substrate (depicted as TNWs⊥Si) and nanowires embedded into Si substrate (depicted as TNWs┼Si), respectively. Notably, the above-mentioned fabrication technique allows to easily produce TiO_2/Si heteronanostructures in large scale (i.e. wafer scale) as shown in Figure 6-2, and this fabrication technique is a universal method to leave enough space for structure optimization and materials selection, thus should be great meaningful for practical applications.

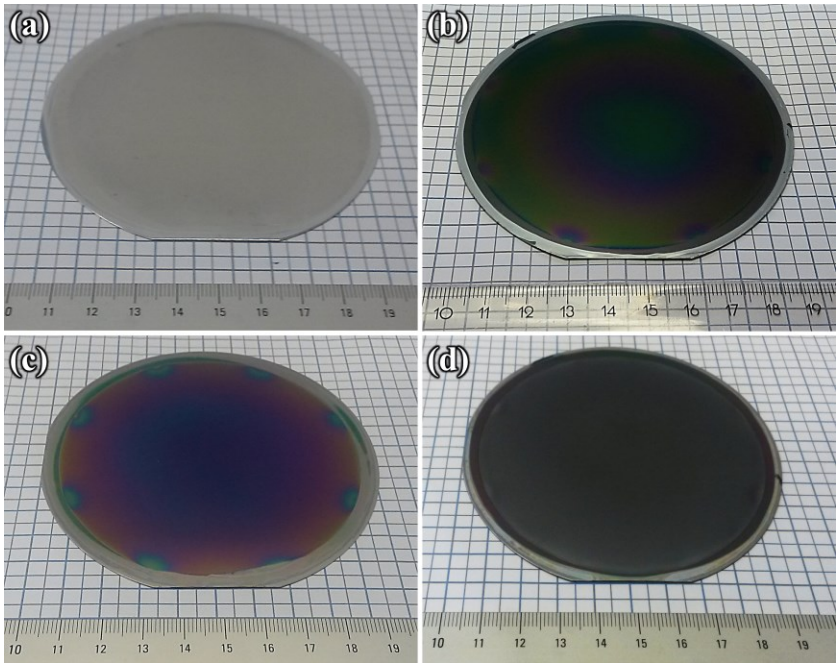

Figure 6–2. Photographs of preparing 4 inches of TNTs╫Si (a) As deposited Al thin film. (b) Etching the Si through the pores of AAO template by ICP. (c) TiO_2 deposition by ALD through the pores of AAO template and Si. (d) 4 inches of TNTs╫Si after removing the AAO template.

6.3.2. Morphology and structural characteristics

Figure 6-3a, b show the SEM images of UTAM and UTAM/Si combined nanopores, respectively. Accordingly, the thickness and pore diameter of the final UTAM are measured to be ~500 nm and ~70 nm, respectively, while the pore diameter and depth of Si nanopores are ~70 nm and ~300 nm, respectively.

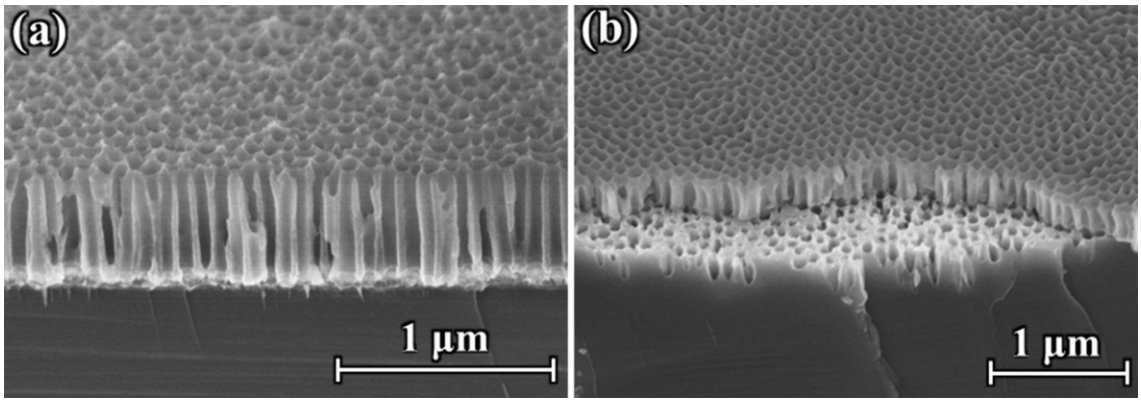

Figure 6–3. (a) Side view SEM image of UTAM/Si after removing the barrier layer. (b) Side view SEM image of a combined structure of UTAM and Si nanopores on Si substrate.

Figure 6-4a, b show the SEM images of TNTs⫫Si that freestanding TNTs with the length of ~500 nm were attached onto Si wafer. In addition, Figure 6-4c, d show the SEM images of TNWs⊥Si that freestanding at the same conditions of TNTs⫫Si. Furthermore, as expected, in the structure of TNTs∥Si, TiO_2 nanotubes were deeply embedded into Si substrate (Figure 6-4e, f). And the structure of TNWs┼Si Show TiO_2 nanotubes were also deeply embedded into Si substrate (Figure 6-4g, h)The total length of TiO_2 nanotube is ~800 nm according to the cross-sectional SEM image (Figure 6-4f), in which ~300 nm long of TiO_2 nanotube was embedded into Si substrate. Accordingly, the contact area of each TiO_2 nanotube or nanowire with Si substrate can be approximately estimated to be 3848.5 nm^2 in TNTs⫫Si or TNWs⊥Si and 69,821.9 nm^2 in TNTs∥Si or TNWs┼Si, respectively. As compared to point contact mode in attached and the embedded mode architecture creates much larger interface between TiO_2 nanotubes or nanowires and Si substrate, where majority carriers can be recombined. On the other hand, TNTs∥Si and TNWs┼Si should have better structural stability than TNTs⫫Si and TNWs⊥Si. The embedded structure feature of TNTs∥Si and TNWs┼Si could efficiently avoid the agglomeration and collapse of TiO_2 nanostructures when increasing the aspect ratio of TiO_2 nanotube.

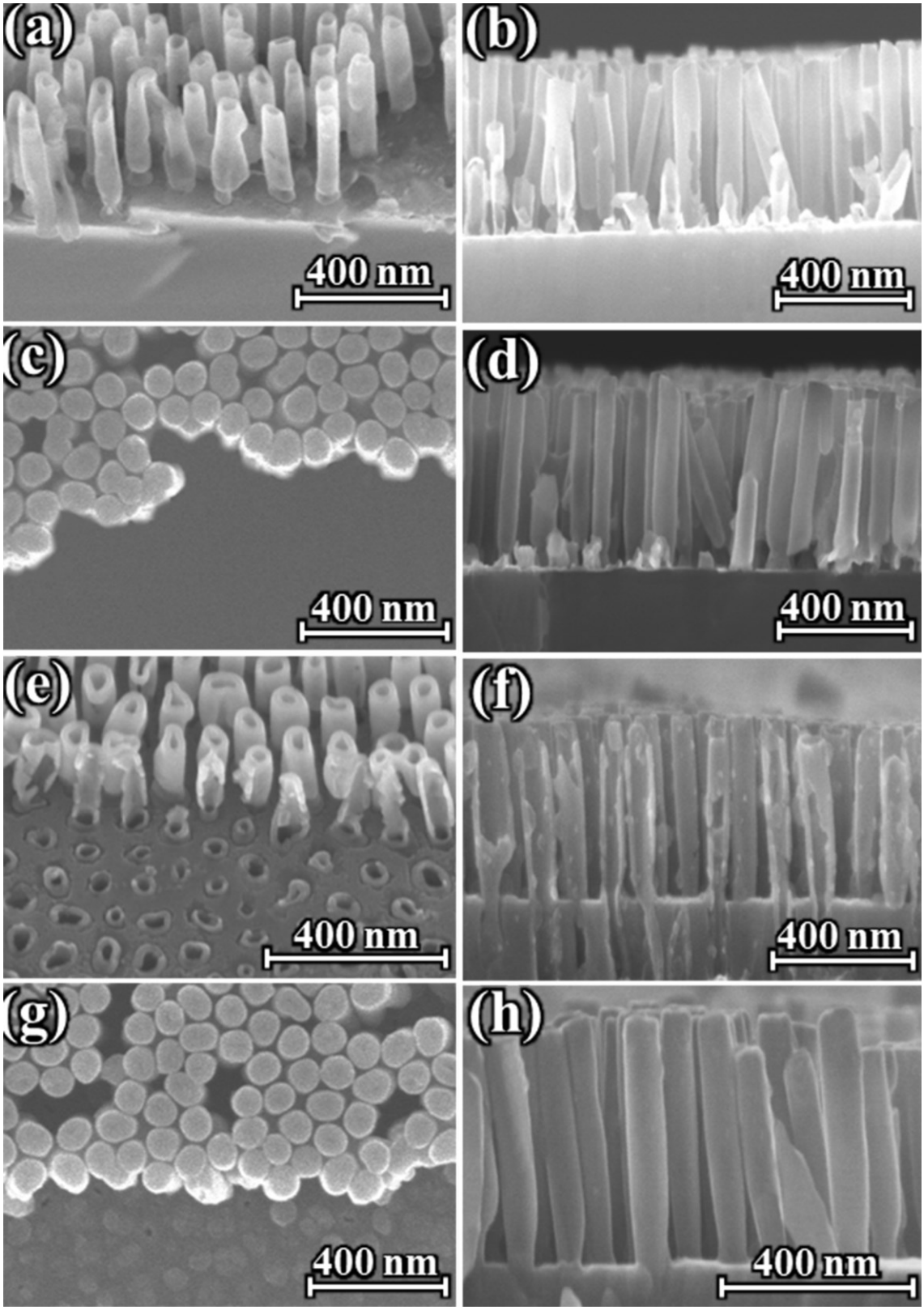

Figure 6–4. SEM image of TiO_2/Si after removing the UTAM, side (a) and cross-section (b) views of TNTs⫫Si heterostructures, respectively, side (c) and cross-section (d) views of TNWs⊥Si heterostructures, respectively, side (e) and cross-section (f) views of TNTs∥Si heterostructures, respectively, side (g) and cross-section (h) views of TNWs┼Si heterostructures, respectively.

High aspect ratio morphology of one-dimensional nanostructures is recommended to overcome the constraint that the charge transport properties within the semiconductor match or exceed the light absorption length scales set by the optical properties of the semiconductor in the solar spectrum, thus could afford a greater attainable photocurrent density.[379] Moreover, longer TiO_2 nanotubes or nanowires enable to achieve larger efficient TiO_2-electrolyte interfacial area that is favorable for the electrochemical reactions. Specially, the asymmetric architecture of TNTs╫Si and TNWs┼Si could be used to simultaneously harvest UV and visible region of the solar spectrum.

Furthermore, in consistent with the recorded results in chapter 4, the as-fabricated TNTs and TNWs exhibited pure anatase phase character as identified by X-ray diffraction (XRD) as shown in Figure 6-5. The XRD pattern shows an excellent agreement with the diffraction peaks for the anatase structured TiO_2.

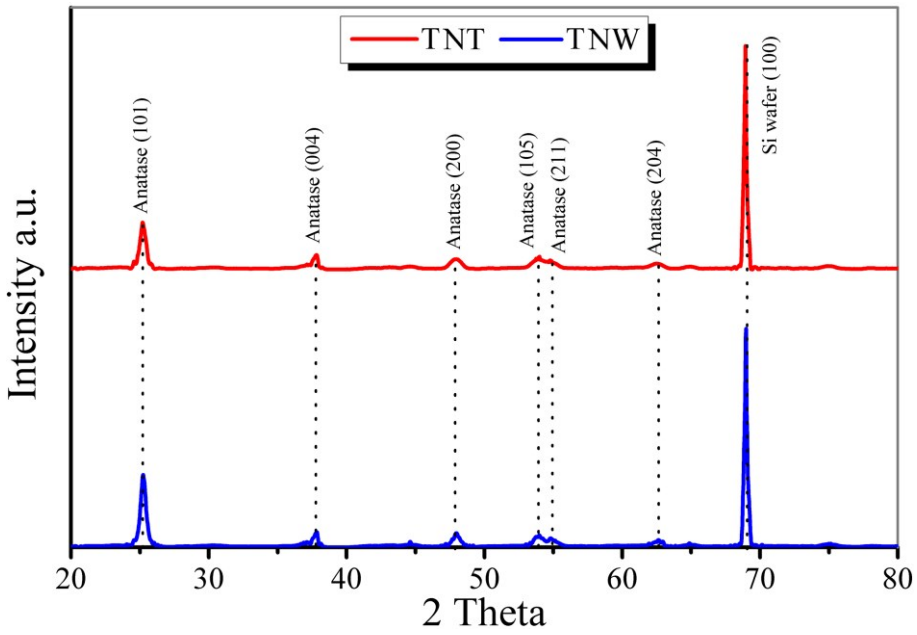

Figure 6–5. XRD patterns for TNTs╫Si and TNWs┼Si heterostructure arrays.

Figure 6-6 indicates a TEM measurements of the prepared TNT and TNW, the HRTEM and selective area FFT further confirmed the crystalline structure of the obtained

TNTs and TNWs (Figure 6-6c-f). The HRTEM image in Figure 6-6c, e demonstrate well-resolved lattice fringes of about 3.5 Å, which corresponds to the (101) crystal plane of anatase TiO_2, which agrees well with the XRD data. The highly crystalline TNTs and TNWs can facilitate charge transfer attributing to the long-range electronic connectivity.[380] Accordingly, owing to all these structural advantages mentioned above for TNTs╫Si and TNWs┼Si nanostructures, i.e., the highly crystalline structure of TiO_2 nanotubes, the vertically aligned and high-aspect ratio TiO_2 nanotubes, the enhanced light harvesting capability, the more contact area between TNTs and Si substrate, and the larger TiO_2-electrolyte interfacial area, improved PEC water splitting performance with TNTs╫Si and TNWs┼Si nanostructures should be highly expected.

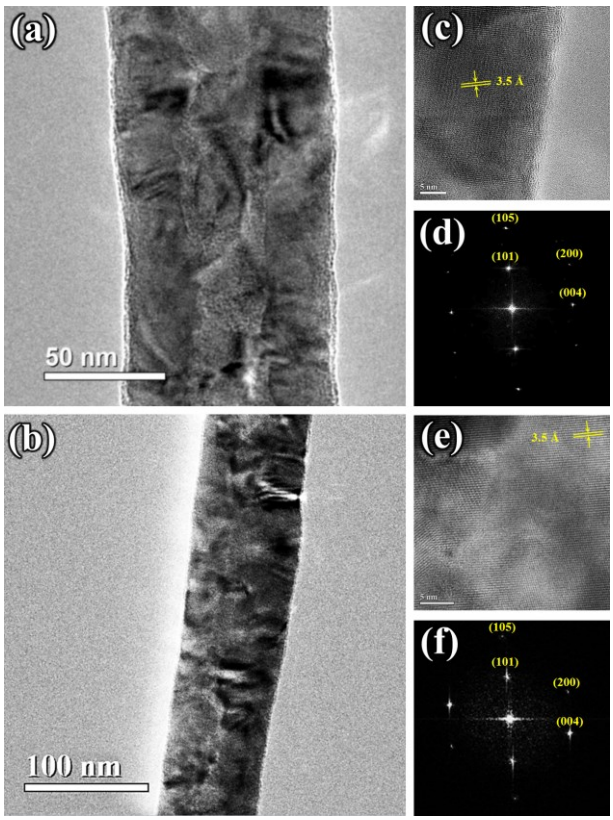

Figure 6–6. (a) TEM of a typical TNT (D ≈ 70 nm), (b) TEM of a typical TNW (D ≈ 70 nm), (c) HRTEM of the TNT edge indicated clear facet distance of TiO_2 (anatase), (d) Fast-Fourier transforms of the selected area of TiO_2 exposed to TiO_2 (101), (e) HRTEM of the TNW indicated clear facet distance of TiO_2 (anatase), (f) Fast-Fourier transforms of the selected area of TiO_2 exposed to TiO_2 (101).

6.3.3. UV-vis spectroscopy

Figure 6-7 represents the reflection spectra of TNTs⫫Si, TNTs⫴Si, TNWs⊥Si, and TNWs┼Si nanostructures. As expected, TNTs⫴Si and TNWs┼Si heterostructures have higher light harvesting efficiency both in UV and visible region than TNTs⫫Si and TNWs⊥Si heterostructures, respectively, which can be attributed to the higher aspect ratio and vertically oriented TNTs in TNTs⫴Si heterostructures and TNWs in TNWs┼Si heterostructures as well as the porous Si structure. The higher light harvesting efficiency would be helpful to achieve higher photocurrent density.

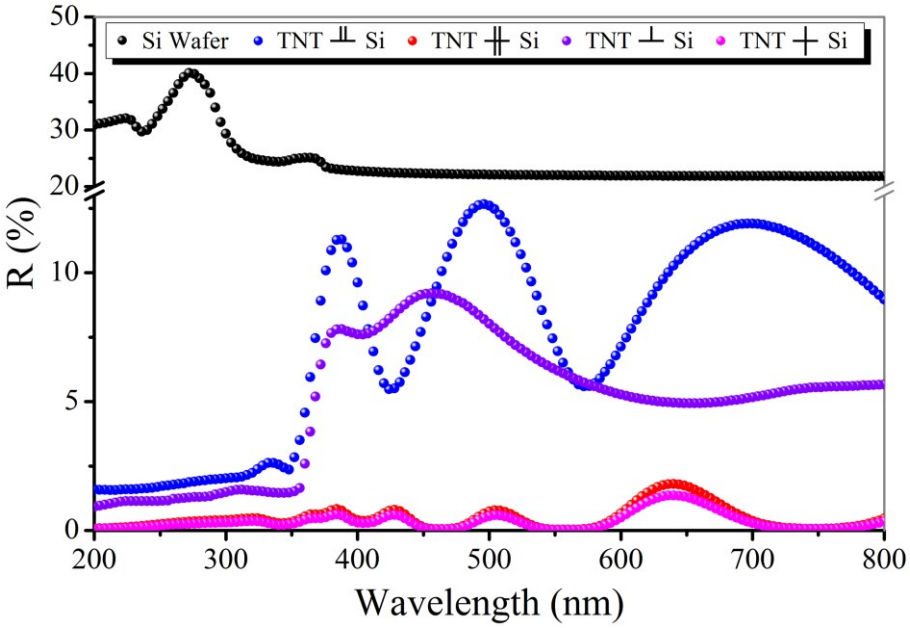

Figure 6–7. Reflectance spectra of the prepared nanostructures (TNTs⫫Si, TNTs⫴Si, TNWs⊥Si and TNWs┼Si) compared with plain Si wafer.

6.3.4. TiO_2/Si heterostructures as photoanode for PEC water splitting

After fabrication of 4-inch of TiO_2/Si with the unique nanostructures arrays confirmations, the photoelectrochemical (PEC) water splitting performance was investigated. Different from previously reported heterogeneous TiO_2/Si photoelectrodes, the as-prepared TiO_2/Si heterostructure has a unique configuration (as illustrated in Figure 6-8a, b), in which TiO_2 nanotubes and nanowires, respectively, are straightly rooted into Si

substrate, respectively. Besides enhancing light harvesting realized through vertically oriented TiO_2 nanotube or nanowire arrays and Si nanopores, the bottom Si/TiO_2 core-shell structure offers large contact area at Si/TiO_2 interface for recombination of majority carriers and the Si substrate also serves as a charge collector for instantaneous charge collection and transport, meanwhile the upper TiO_2 nanotube has large TiO_2-electrolyte interfacial area to provide abundant reactive sites for the water oxidation reactions, thus finally achieved a promising PEC efficiency. Additionally, the configuration of TiO_2 nanotubes and TiO_2 nanowires straightly rooted into Si endows the TiO_2╫Si heterostructure and TiO_2┼Si heterostructure photoelectrodes excellent stability during water oxidation reaction.

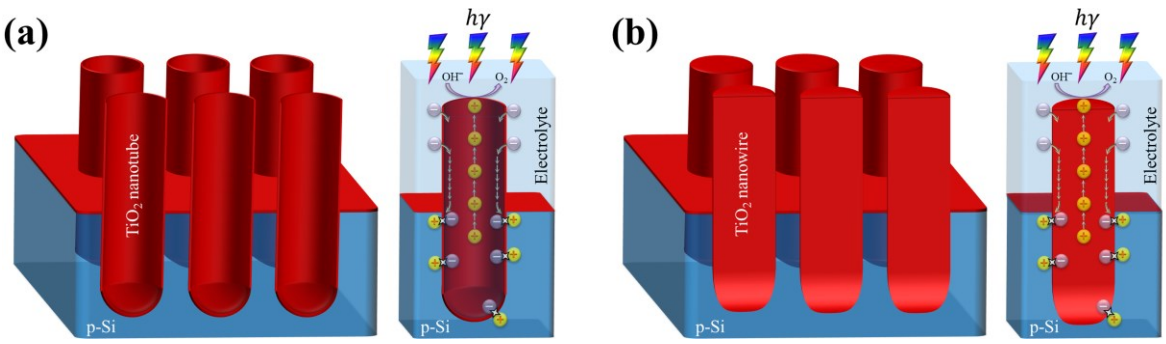

Figure 6–8. Schematic illustration of innovative (a) TNTs╫Si (b) TNWs┼Si heteronanostructures as photoanode for PEC water splitting.

To evaluate the photoelectrochemical activities of these novel TiO_2/Si heterostructured photoelectrodes, PEC cells were fabricated and characterized. All the PEC characterization of TNTs╨Si, TNTs╫Si, TNWs┸Si and TNWs┼Si photoelectrodes were performed using a typically three-electrode electrochemical cell configuration in 1 M NaOH electrolyte under simulated sunlight illumination at 100 mW cm^{-2} from a 150 W xenon lamp coupled with an AM 1.5G filter. Figure 6-9a shows linear sweep photovoltammetry measurements to determine the photocurrent density of TNTs╨Si, TNTs╫Si, TNWs┸Si and TNWs┼Si photoelectrodes. All the four types TiO_2/Si heteronanostructured photoelectrodes achieve

photocurrent densities of a few mA cm^{-2} under light illumination. Compared to TNTs⫫Si photoelectrode with TNTs∥Si photoelectrode and TNWs⊥Si photoelectrode with TNWs┼Si photoelectrode show obviously enhanced photocurrent densities over the entire bias range. Typically, at the bias of 0.7 V vs RHE, the photocurrent density of the TNTs∥Si photoelectrode is 2.86 mA cm^{-2}, which is 1.41-fold of that for TNTs⫫Si photoelectrode, also the photocurrent density of the TNWs┼Si photoelectrode is 2.25 mA cm^{-2}, which is 1.43-fold of that for TNWs⊥Si photoelectrode. Figure 6-9b reveals the transient current response under chopped illumination with applied a bias of 0 V vs RHE under 100 mW cm^{-2} illumination of a full spectrum solar simulator, the TNTs∥Si photoelectrode yields a maximum photocurrent density of 1.84 mA cm^{-2}, 43.75 % higher than that of TNTs⫫Si photoelectrode (1.28 mA cm^{-2}), while the TNWs┼Si photoelectrode yields a maximum photocurrent density of 1.68 mA cm^{-2}, 46.08 % higher than that of TNWs⊥Si photoelectrode (1.15 mA cm^{-2}). The reason might be attributed to the higher light harvesting efficiency and larger TiO_2-electrolyte interfacial area in TNTs∥Si and TNWs┼Si heteronanostructures than TNTs⫫Si and TNWs⊥Si heteronanostructures and subsequently results in higher photocurrent density.[48, 379] It is noted that the obtained photocurrent density of TNTs∥Si photoelectrode is competitive to other reported TiO_2/Si heterostructure PEC anodes (Table 6-1).

Table 6-1. Comparison of PEC water splitting performance of the represented novel nanostructures with previous published researches.

Cell type	η (%)	U (V)	J_{Ph} (mA cm^{-2})	Electrolyte	Technology
TiO_2/Si	Not reported	-0.5 vs. SCE	~0.25	1 M KOH	Wet-etched Si, ALD of TiO_2.[381]
TNW	1.63	0.6 vs. Ag/AgCl	Not reported	1 M NaOH	hydrogen treatment.[375]
α-Fe_2O_3/Si	Not reported	1.2 vs. RHE	~0.95	1 M NaOH	ALD of α-Fe_2O_3 on Si NW.[58]
Hierarchical TiO_2/Si nanowire	Not reported	0.5 vs. Ag/AgCl	2.7	1 M KOH	Wet-etched Si, ALD of TiO_2.[48]
TNT	2.96	−0.4 vs. Ag/AgCl	Not reported	1 M KCl	Anodization, hydrogen treatment.[382]
TiO_2/FTO	Not reported	1.23 vs. RHE	~2.0	1 M NaOH	$TiCl_3$ & flame treatments of TiO_2 nanotube.[47]
TiO_2-SQ	Not reported	0.75 vs. Ag/AgCl	~0.1	0.1 M KPi buffer	TiO_2-catechol complex.[60]
Hierarchical porous TiO_2	0.35	−0.33 vs. Ag/AgCl	Not reported	1 M KOH	F-doped silica template method.[383]
TiO_2/Si	Not reported	2 vs. RHE	0.36	0.25 M Na_2SO_4	Core/shell and branched TiO_2/Si NWs arrays by hydrothermal reaction.[384]
TNTs╫Si	**1.93**	**0.2 vs. RHE**	**2.41**	**1 M NaOH**	**TiO_2 nanotube rooted into porous UTAM/Si using ALD (this study).**
TNWs┼Si	**1.50**	**0.2 vs. RHE**	**1.74**	**1 M NaOH**	**TiO_2 nanowire rooted into porous UTAM/Si using ALD (this study).**

The incident photon-to-electron efficiency plots further claim the substantial enhancements of the photocurrent densities across the entire functional wavelength (Figure 6-9c). The photocurrent densities are considered to greatly rely on the photon utilization efficiency, which depends on the charge kinetics (including charge transfer and surface reactions).[54, 385] Since the diffusion rate of electrons is significantly higher than that of holes, the balance between holes and electrons transfer in TiO_2/Si heteronanostructured photoelectrodes is one of the crucial issues to determine the photocurrent density, thus the

water splitting rate and efficiency. Owing to the unique structure of TNTs╫Si photoelectrode, TNTs possess a shorter carrier diffusion length and a larger surface area that could facilitate holes transport for the oxidation reaction and also better balance electrons transfer in Si for the reduction reaction. On the other hand, the more contact area between the TiO_2/Si interface enable the recombination of majority carriers to largely enhance the charge migration behaviors, thus to achieve higher photocurrent densities; the larger surface area of TNTs creates more TiO_2/electrolyte interface, and finally to promote O_2 evolution kinetics. In addition, to evaluate the capability of actual utilization of the photons more clearly, the ABPE (photoconversion efficiency) was calculated from J-V data using the equation (5-2).

Figure 6-9d reveals the calculated ABPEs as a function of external potential versus RHE from the results in Figure 6-9a. The maximum photoconversion efficiencies for the TNTs╨Si, TNTs╫Si, TNWs┴Si and TNWs┼Si photoelectrodes were 1.37 %, 1.93 %, 1.03 % and 1.50 %, respectively. The promising ABCE results further confirm the unique structure of TNTs╫Si photoelectrode to facilitate charge migration in PEC water splitting. Notably, the TNTs╫Si photoelectrode also has better mechanical stability during water oxidation reaction than TNTs╨Si photoelectrodes. As shown in Figure 6-10, there are almost no structural changes for TNTs╫Si photoelectrode before and after water oxidation reaction, attributing to TiO_2 nanotubes straightly rooted into Si substrate. However, the agglomeration of TiO_2 nanotubes and the detachment of TiO_2 nanotubes from Si substrate are found in TNTs╨Si photoelectrodes.

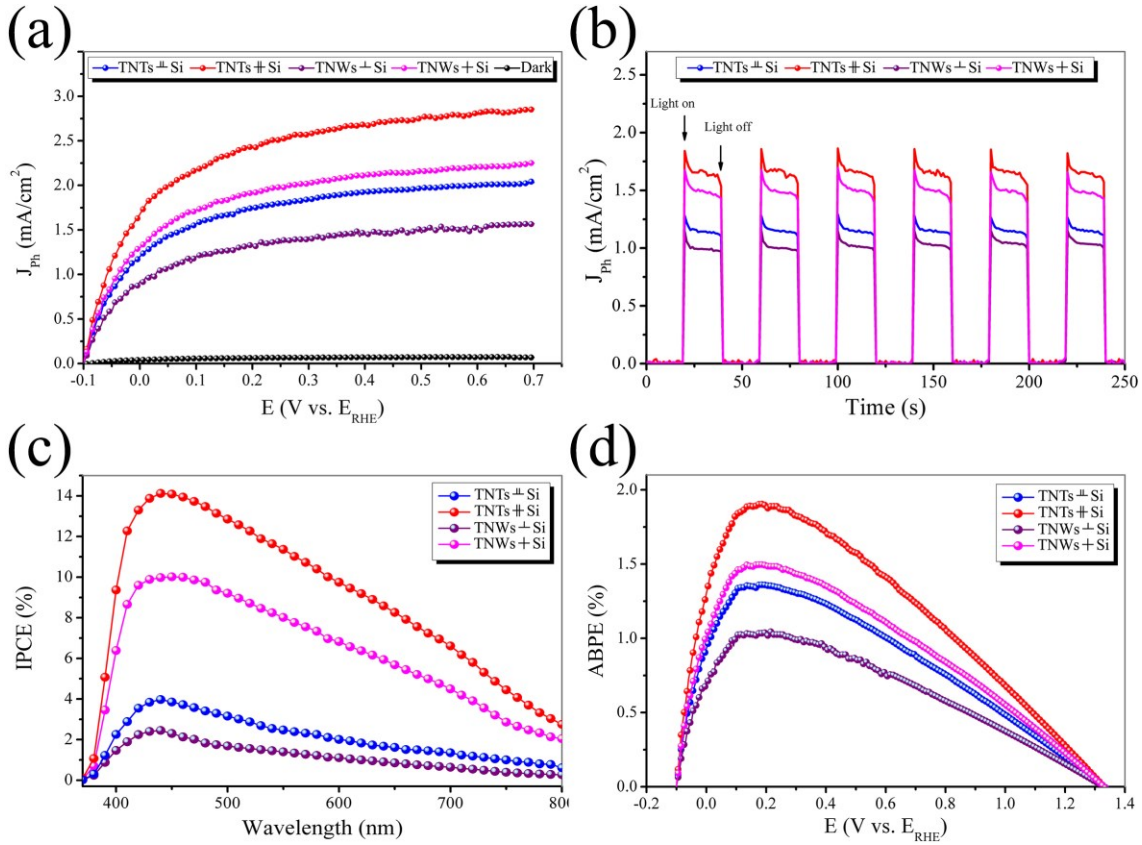

Figure 6–9. (a) Photocurrent densities of TNTs⊥Si, TNTs∥Si, TNWs⊥Si and TNWs┼Si heterostructure arrays under white light illumination (AM 1.5G, 100 mW cm^{-2}) from -0.1 to -0.7V vs. RHE. (b) Current density of externally short-circuited of the prepared samples measured at 0 V vs. RHE under the same illumination conditions as at (a) with using chopped light exposure. (c) IPCE spectra of the prepared samples (without applying external bias). (d) The calculated photoconversion efficiencies for the prepared photoanodes, as a function of applied potential vs. RHE.

A schematic diagram of the predicted equilibrium band alignment and the photoelectrochemical reaction in the PEC cell is shown in Figure 6-11. The unique TNTs∥Si heteronanostructured photoelectrode can be considered as a direct semiconductor-semiconductor all-solid-state Z-scheme structure. Upon illumination, electron-hole pairs are generated in Si and TiO_2, which absorb different regions of the solar spectrum, respectively, because the TiO_2 shell is transparent under visible light and then visible light can be harvested by Si. Due to the band-bending at the semiconductor-electrolyte interfaces, the photogenrated holes in TiO_2 migrate to the surface to oxidize water to produce O_2, and meanwhile the photogenerated electrons in Si deliver to the Pt to

reduce protons to produce H_2. The holes in Si and the electrons in TiO_2 recombine at the interfaces area of the TiO_2/Si, completing the relay of the Z-scheme. Considering the current-matching requirement in a Z-scheme system, the overall rate of water splitting is limited by the photoelectrode that produces the smaller photocurrent output.[61] In the structure of TNTs╫Si, owing to the 1D tube morphology of TNTs, the possibility of electron-hole recombination is lower because the travel distance of the hole is much shorter and thus more holes could reach the TiO_2-electrolyte interface before they are trapped, resulting in high photocurrent density. Furthermore, the larger interface of TiO_2/Si can promote the recombination of photogenerated electrons from the conduction band of TiO_2 and holes from the valence band of Si.[63]

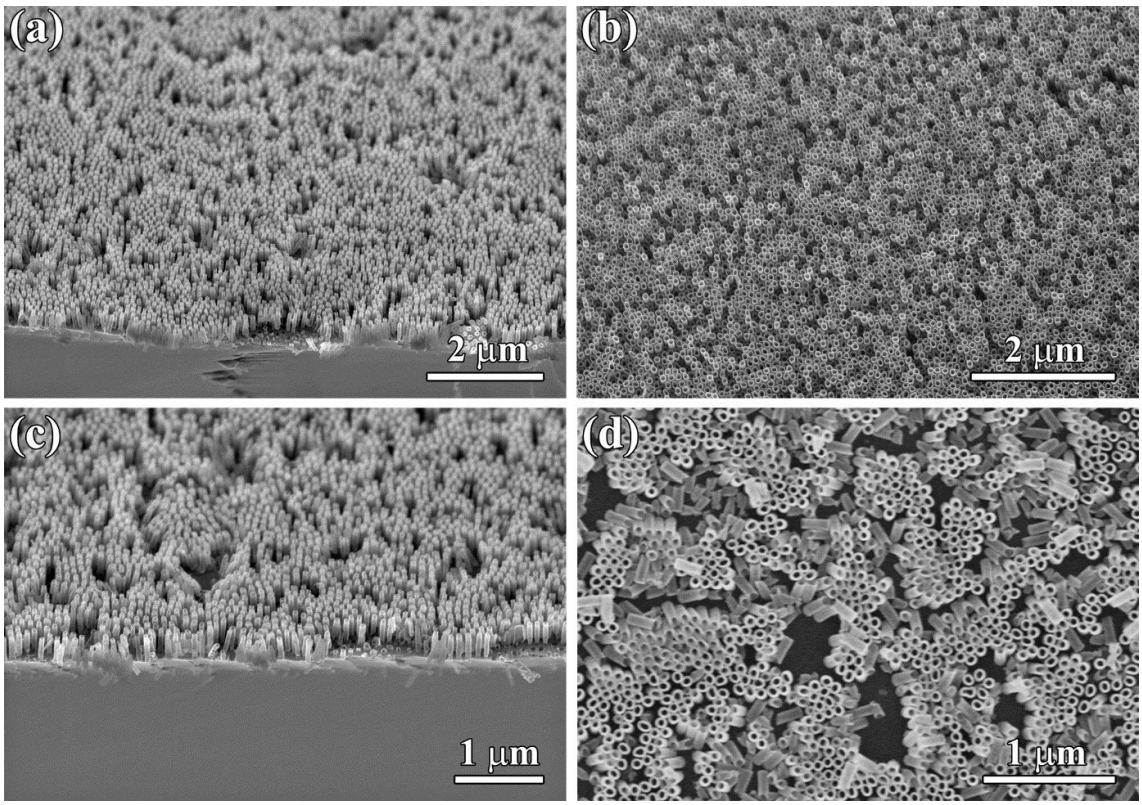

Figure 6–10. SEM images of TNTs╫Si (a) and TNTs╨Si (b) heteronanostructure arrays before water oxidation reaction. SEM images of TNTs╫Si (c) and TNTs╨Si (d) heteronanostructure arrays after water oxidation reaction.

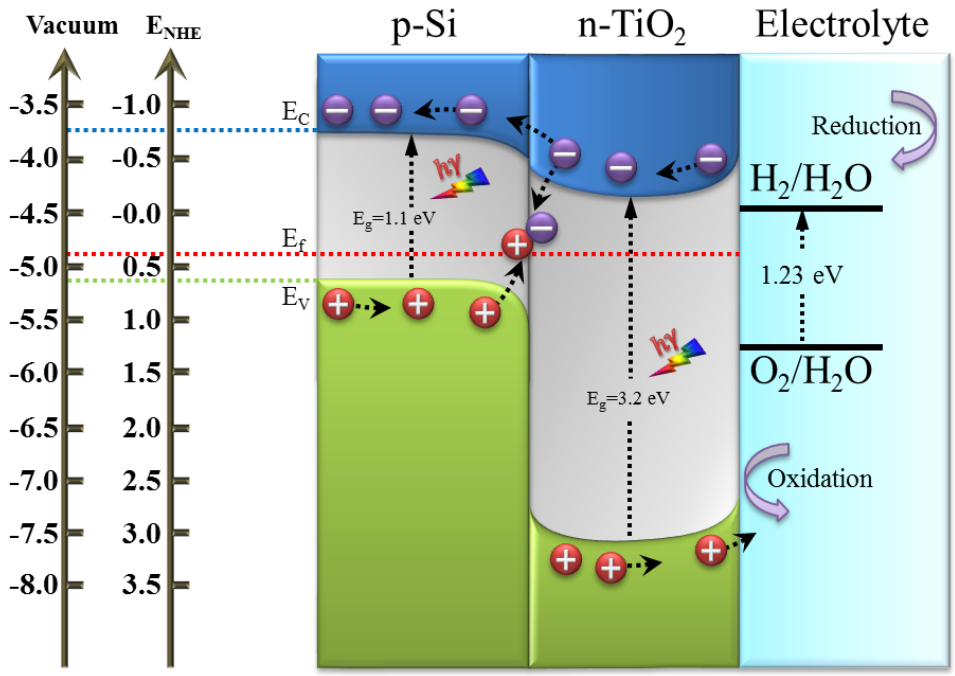

Figure 6–11. Energy band diagram of the TiO_2/Si heterostructure photoanode interface as a Z-scheme model under solar light irradiation.

To further understand the structure advantages of the presented photoelectrodes (rooted TNTs and TNWs into Si) for enhancing PEC water splitting, the finite difference time domain (FDTD) simulations were performed to calculate electric field distribution across the interfaces in TNTs⫫Si and TNTs⫲Si photoelectrodes under 450 and 780 nm, respectively, as shown in Figure 5-11. The color index represents the magnitude of electric field intensity normalized with the light propagating in free space. Obviously, all TNTs⫫Si, TNTs⫲Si, TNWs⊥Si and TNWs┼Si heteronanostructures show a significant absorbance enhancement at 450 and 780 nm. Especially, a greater electric field enhancement is observed around the TNTs and TNWs surface as well as the porous Si in TNTs⫲Si and TNWs┼Si heteronanostructures (Figure 6-12a, b top). Furthermore, even more electric field enhancement is produced in TNTs⫲Si and TNWs┼Si heteronanostructures at 780 nm (Figure 6-12a, b bottom). The electric field enhancement means the more light to be trapped in TNTs⫲Si and TNWs┼Si heteronanostructures than that in TNTs⫫Si and TNWs⊥Si heteronanostructures, and thus resulting in the higher

photocurrent density and IPCE. Therefore, it could be concluded that the enhanced PEC performance does result specially from the distinguished structural features of the rooted TNTs and TNWs photoelectrodes.

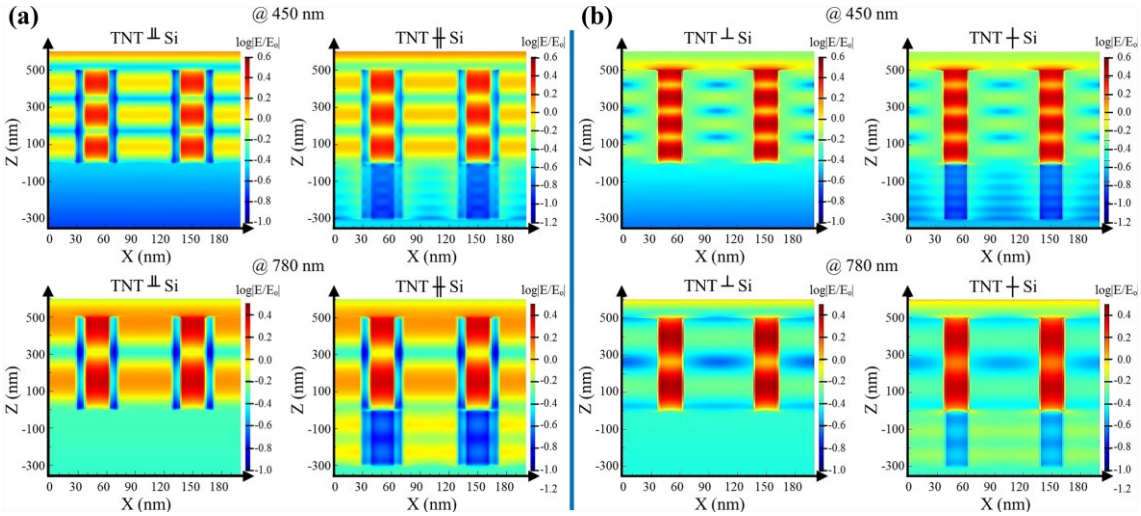

Figure 6–12. Cross-sectional electric field intensity distributions for TNTs (a) and TNWs (b) nanostructures at an incident light wavelength of 450 and 780 nm, respectively.

6.3.5. TiO_2/Si heterostructures as a solid-state solar cell

The fabrication of 4-inch of TiO_2/Si heteronanostructures were coated with 30 nm of AZO as a transparent conductive layer to cover the entire porous structures including the pores of the TNTs and the interpore distance in TNTs and TNWs as shown in Figure 6-13a. Since the deposition of AZO layer was covered the whole surface of the samples including the TNTs, TNWs, and also the Si in the back side, the 4-inch sample was served into smaller pieces (~ 1 inch diameter) as displayed in in Figure 6-13b. Finally, 20 nm of gold layer was deposited by e-beam evaporation as a front and back contacts.

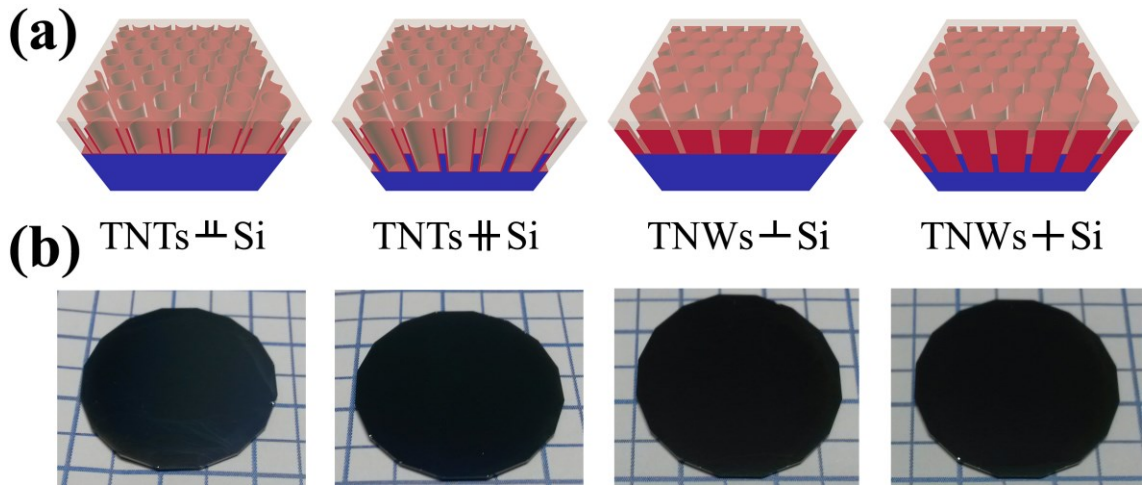

Figure 6–13. (a) Schematic of the AZO layer deposition covered the TiO_2 nanostructures in TNTs⫫Si, TNTs⫩Si, TNWs⊥Si and TNWs┼Si samples. (b) Photographs after severed the 4-inch sample into 1-in.

Figure 6-14 depicts the J-V characteristic under white light illumination (AM 1.5G, 100 mW cm^{-2}) of these devices. As accepted the open-circuit voltage and the short-circuit current density were 0.124 V and 1.81 mA cm^{-2} in TNWs┼Si and TNTs⫩Si (0.116 V and 1.52 mA cm^{-2}) higher than the obtained results in TNWs⊥Si and TNTs⫫Si. The efficiencies of the four configurations are estimated as shown in Table 6-2.

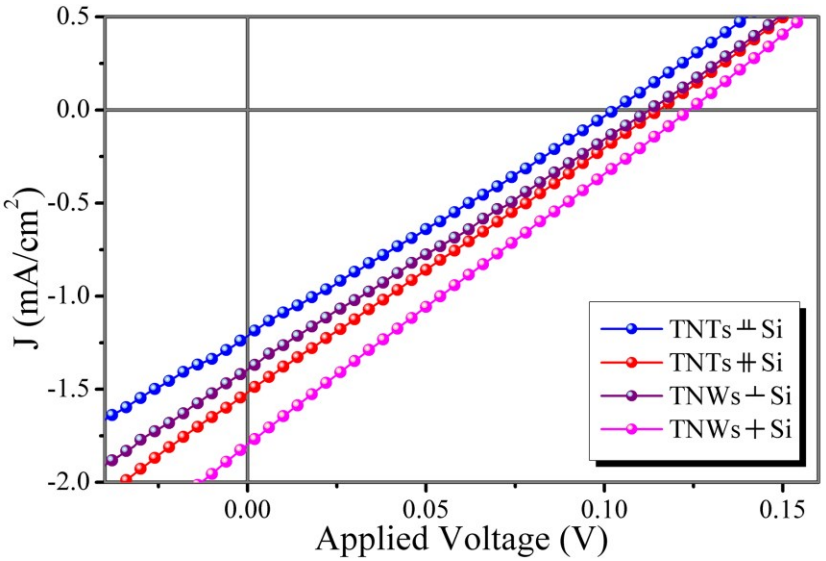

Figure 6–14. J–V characteristics of TNTs⫫Si, TNTs⫩Si, TNWs⊥Si and TNWs┼Si heteronanostructures under white light illumination (AM 1.5G, 100 mW cm^{-2}).

In addition, the external quantum efficiency (EQE) was gauged at 0 bais (Figure 6-15), Showing that a higher photocurrent can also be achieved by these unique heteronanostractures (TNWs┼Si and TNTs╫Si) improving the carrier gathering of the device. Indeed, the recombinations take place at the defect sites at the interface between TiO_2 and Si,[358, 386] according to the large lattice mismatch between TiO_2 and Si and misfit-dislocation density, especially that there was no any peak of impurity traced in the XRD patterns (see Figure 5-6). It should noted that the materials in this study are just an example to display the enhancement of the performance of solar energy applications during such of innovative nanostractures. The varied of TiO_2/Si heteronanostractures appeared an improvement in TNWs┼Si and TNTs╫Si than that in TNWs┴Si and TNTs╨Si as recorded in Table 6-1.

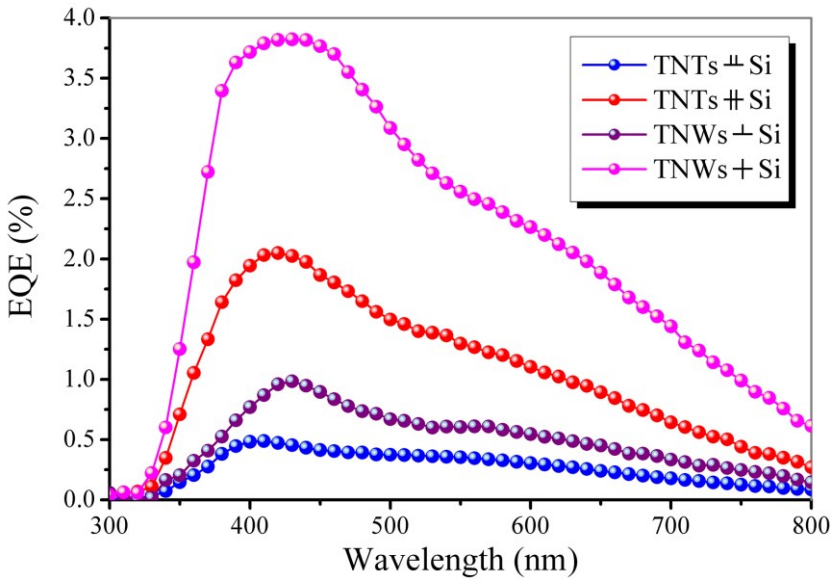

Figure 6–15. The external quantum efficiency of the corresponding heteronanostructures (TNTs╨Si, TNTs╫Si, TNWs┴Si and TNWs┼Si) at a bias of 0 V.

Table 6-2. The results estimated from the TiO_2/Si heteronanostructures as a direct solar cell.

Cell type	V_{OC} (V)	J_{SC} (mA cm^{-2})	η (%)	EQE (%)
TNWs┼Si	0.124	1.81	0.55	3.82
TNTs╫Si	0.116	1.52	0.44	2.05
TNWs┼Si	0.112	1.39	0.4	0.99
TNTs╫Si	0.104	1.22	0.32	0.49

6.4. Conclusion

The unique structure of TNTs╫Si photoelectrodes enable higher light harvesting efficiency, offer larger interface for recombination of majority photogenerated charge carriers, and also have larger semiconductor-electrolyte interfacial area for the water oxidation reactions. Notably, all these advantages ensure a significant enhanced PEC performance. Further optimization of structure, photocatalyst and other factors (plasmonic and co-catalysts, etc.) could be highly expected to finally realize the full potentials of PEC water splitting. In addition, AZO/TNWs┼Si/Au heteronanostructure shosws better performance in solid-state solar cell, which can utilized for advanced photovoltaics device with different semiconductor materials.

7. Summary and Outlook

Many of the results achieved in this dissertation are in themselves a proof of concept. In future research, the AAO templates could be improved and their limits tested. This would include analysis of the optimum nanostructure arrays for area, size, and shape. To summarize the scientific developments achieved in the present work:

1) Through a unique design of the fabrication and transferring processes, a facile transferring of wafer-scale (4 inch) A-UTAM onto substrates without any twisting, folding, cracking and contamination has been achieved. The most important element of the demonstrated method is fixing the UTAM onto the wafer-scale substrate before removing the remaining Al and alumina barrier layer. The thickness and surface smoothing of UTAMs play crucial roles in this transferring process. By using these perfectly transferred UTAMs as masks, various nanostructure patterns including nanoparticle, nanopore (nano-mesh) and nanowire arrays have been fabricated on wafer-scaled Si substrate, with tunable and uniform dimensions. Technically, there is no limit to the size of the A-UTAM and there are no absolute prerequisites for UTAMs, substrates and the materials of the UTAM-prepared nanostructures in this approach. Metals, insulators and semiconductors can all be patterned.

2) 4-inch A-UTAM is an important breakthrough for the broad research field of surface nanopatterning and nanostructuring, and the related devices. To the author's knowledge, the route is the only efficient technique so far to have realized ordered arrays of nano-patterns with adjustable dimensions under 100 nm over a wafer-scale area without the need of lithographic processes. Neither does there appear to be any other non-lithographic method (non-lithographic methods have potential for highly efficient and large-scale surface patterning) which can fabricate nano-patterns with a similar level of

scale, size and regularity. The simple but efficient method described in this dissertation provides a cost-effective platform for the fabrication of ordered nanostructures on large substrates for various applications in nanotechnology.

3) Highly ordered TiO_2 nanotube arrays with excellent crystal quality have been fabricated by techniques combining anodic aluminum oxide (AAO) templates and atomic layer deposition (ALD). Unlike the conventional ALD method that usually results in a relatively low crystal quality of the prepared materials, the annealing treatment between two-step ALD procedure could greatly improve the crystal quality of the resultants, proving a decent methodology to prepare ultra-thin films with high crystal quality.

4) Instead of a quantum effect for influencing the absorption band edge of TiO_2 nanostructures, this study finds that the periodical parameters can also be utilized to manipulate the optical bandgap of the TiO_2 nanotube arrays. Through absorption spectroscopic analysis, it is observed that the optical absorption band edge of the TiO_2 nanotube arrays exhibits a red shift as the diameter of the nanotube is tuned to be larger and the distance between two nanotubes becomes smaller accordingly, while the thickness of the wall of the nanotube is kept constant. Finite-difference time-domain simulations support the observation from the theoretical point of view and reveal a large near-field enhancement around the nanotubes for the arrays with densely distributed nanotubes, when the corresponding arrays are illuminated. These results will be of value to researchers working in the realms of AAO templates, nanostructure engineering and photoelectronics.

5) CdTe has long been regarded as a suitable material in solar cells. Introducing such material to photoelectrochemistry for water splitting provides an alternative means of solar energy utilization. Instead of using CdTe as a sensitizer for wide bandgap semiconductors, CdTe is used as the core material for solar energy conversion by constructing CdTe/TiO_2

core/shell nanowire arrays. Both the CdTe and TiO_2 components present a high crystalline quality. In comparison with the photoanode with only a TiO_2 nanotube array, the CdTe/TiO_2 electrodes are vastly better in performance. By modulating the diameters of the CdTe/TiO_2 nanorod arrays, the photocurrent is raised to be as much as 1.1 mA cm^{-2}. Subsequent characterizations reveal that the CdTe core is responsible for utilization of photons in the visible range and the TiO_2 shell is beneficial for core protection, promoting charge separation in the structures. The Z-scheme configuration of the heterojunction is also of great advantage to promote the photoelectrochemical reactions.

6) Unlike many previously reported heterogeneous photoelectrodes that adopt core/shell configurations, what are here fabricated are novel heterostructures (TNTs╫Si and TNWs┼Si) with a configuration of TiO_2 nanotubes vertically rooted into Si substrate for photoelectrochemical water splitting and a solid-state solar cell.

7) The configuration of TNTs╫Si heterostructures offers structural advantages for PEC water splitting in which the freestanding TiO_2 nanotube arrays together with nanoporous Si enhance light harvesting efficiency; the bottom Si/TiO_2 core/shell structure offers large contact area at Si/TiO_2 interface for the recombination of the majority of photogenerated charge carriers; the Si substrate also serves as a charge collector for instantaneous charge collection and transport; the freestanding TiO_2 nanotubes with high aspect ratio have a large TiO_2-electrolyte interfacial area to provide abundant reactive sites for the water oxidation reactions. As a result, the PEC performance of TiO_2╫Si heterostructures is among the best for heterogeneous photoelectrodes based on TiO_2 and Si. Compared to the heterogeneous photoelectrodes reported in the literature, the structures of TiO_2 nanotubes vertically rooted into Si substrate show excellent structural stability during the water oxidation reaction. The agglomeration of high aspect ratio TiO_2 nanotubes and the detachment of TiO_2 nanotubes from the Si substrate have been efficiently avoided.

8) The configuration of TNWs┼Si heterostructures achieves better light absorption than reported TiO_2/Si nanostructures, which may open up new options in the design of high-performance photovoltaic devices.

8. Extended Work

8.1. Introduction

During the PhD studies, the resistive switching random access memories (RRAM) based on perfect ordered porous AAO membrane have also been studied. This section of the dissertation focuses on preparation of RRAM system with high density, low power consumption, fast writing/erasing speed, good endurance and simple and small operation system. However, the low power consumption and the high density are still facing significant challenges. Here, by using a nonlithographic technique, a three-dimensional vertical RRAM device array with perfect order and density as high as that of the nanopores of the template (10^8~10^9 cm^{-2}) has been demonstrated, which can also fabricated in large area. The high crystallinity of the materials and the perfect interfacial effect (3 nm interfacial layer) make the ultralow power consumption possible (millivolt magnitude). This procedure for fabricating the nanodevice arrays in large area can be used for producing many other different materials and such three dimensional electronic device arrays with the capability to adjust the device densities can be extended to other applications of the next generation nanodevice technology.

8.2. Experimental Section

8.2.1. Preparation of perfect AAO template

Perfectly ordered AAO templates with different diameters were prepared by using high-purity (99.99%) aluminum foil with a thickness of 0.2 mm. Al foils were first cleaned by acetone, ethanol and DI water successively then electrochemical polished in a 1:7 solution of perchloric acid and ethanol. The Ni stamp with nanopillar periods of 400 nm was placed on electropolished Al foil, and a reverse replication of nanopillar array was conducted on the Al foil by using an oil press under a pressure of about 10.0 MP for 10 min. The anodization of the Al foil was performed under a constant voltage of 160 V in 0.4 M H_3PO_4 at 15 ˚C for 10 min. The obtained AAO templates were put in 5 wt % of the

H_3PO_4 solution at 30 ˚C to realize desirable pore-diameter. After 120 or 140 min of the pore-widening process, the resulted AAO template will have a pore diameter of about 250 nm and 300 nm, respectively.

8.2.2. Fabrication of the core-shell nanostructure arrays

The deposition of TiN@TiO_2@Pt core-shell nanostructure arrays was conducted in a Picosun SUNALETM R150 ALD System. The AAO template was placed in the chamber of the ALD system and TiN was first deposited at a temperature of 400 °C. $TiCl_4$ and NH_3 were used as precursors with respective pulse/purge times of 0.1 s/6 s and 1 s/10 s and a carrier gas flow of 120 sccm. N_2 gas was used as both carrier and purge gas. This ALD process was repeated 1700 times, leading to TiN layer of about 30 nm. Before the deposition of the TiO_2, the surface of the sample was etched by ion-milling with an angle of 60° at energy power of 5 kV and rotation of 5 Hz to remove the top surface of TiN, leading to separated TiN nanotube arrays for achieving high density device arrays. To deposit the second layer of TiO_2, two-step ALD procedure was adopted to deposit 1200 cycles of TiO_2 deposition by using $TiCl_4$ and H_2O as Ti and O sources under 25 °C. The typical pulse/purge time for $TiCl_4$ and H_2O precursors was 0.1 s/5 s and the carrier gas flow was set at 200 sccm. Then Pt was deposited as the other electrode under a chamber temperature of 300 °C and a Pt(MeCp)Me_3 precursor temperature of 80 °C. 500 ALD process cycles were conducted for the deposition of Pt nanowire array with typical pulse/purge time of Pt(MeCp)Me_3 and O_2 was 1.3 s/30 s, while the N_2 carrying gases are kept at 100 sccm.

8.2.3. Device fabrication and characterization

After the fabrication of the core-shell nanostructure arrays, the Al on the backside of the AAO template was removed in a mixture solution of $CuCl_2$ (90 wt %) and HCl (10 wt %). The sample was transferred in 5 wt % H_3PO_4 solution at 30 °C for 50 min to remove the barrier layer and show up the TiN nanotube electrodes. Using a line array shadow mask with distance 3 μm, Au thin film (30 nm) was deposited by using electron beam physical vapor deposition from Kurt J. Lesker. The SEM images and EDX patterns of the as-prepared core-shell TiN@TiO_2@Pt nanostructure arrays were investigated using a scanning electron microscope (SEM, Hitachi S4800). The TEM lamella was prepared by using focused ion beam equipment in a Zeiss NVision 40 CrossBeam^{TM} focus ion beam (FIB) instrument equipped with a Ga liquid metal ion source. The energy of the Ga ions can be adjusted from 1 keV to 30 keV. In order to obtain ultrathin lamella, double-tilt method have been applied. Figure S3 shows the main steps of the TEM lamella preparation: (1) deposition of amorphous carbon, (2) rough milling and lift-out and (3) double-tilt thinning. Prior to the rough thinning, an amorphous carbon layer with a thickness of ~ 2 μm was deposited using ion beam induced deposition (IBID) to protect the nanowires from subsequent Ga ion bombardment. Rough milling was carried out using 30 keV Ga ions to remove materials around the region of interest. For lift out, the lamella was attached to a manipulator using IBID and then cut free from the bulk. The dimension of the lamella was approximately 10 μm wide, 10 μm high and 2 μm thick. After lift out process, the lamella was transferred to a TEM grid using the manipulator and IBID. The TEM grid was mounted on a special rotation-tilt holder which allows double-tilt thinning to be carried out. As shown in the lower-right figure in Figure 8-1, the backside of the lamella was thinned perpendicular to the nanotubes. The thinning of the backside was stopped when the depth of the groove reached approximately half of the lamella thickness.

Subsequently, the front side was thinned orthogonally to the first milling groove. At the end, a thin window containing a several nanowires was created where the two milling grooves overlap. During thinning, the Ga ion energy was gradually reduced from 30 keV to 1 keV to reduce ion-bombardment induced damage. The glancing angle was kept at a low value between 1° to 3° to obtain flat surfaces. The thickness of the thin window was monitored by measuring the secondary electron (SE) intensity. Figure 8-2a represents a 2 kV SE image of the lamella after double-tilt thinning. The thin window is indicated by the rectangle. Figure 8-2b shows a 300 kV TEM image of the lamella, six nanowires can be clearly seen within the thin window. HRTEM images were performed on an image-side Cs-corrected FEI Titan 80–300 microscope operated at an acceleration voltage of 300 kV. X-ray diffraction patterns were studied by utilizing a Siemens D5000 XRD equipment. Electrical measurements of the fabricated devices were performed using a micromanipulator 4060 probe station with a Keithley 4200-SCS semiconductor characterization system in the air atmosphere.

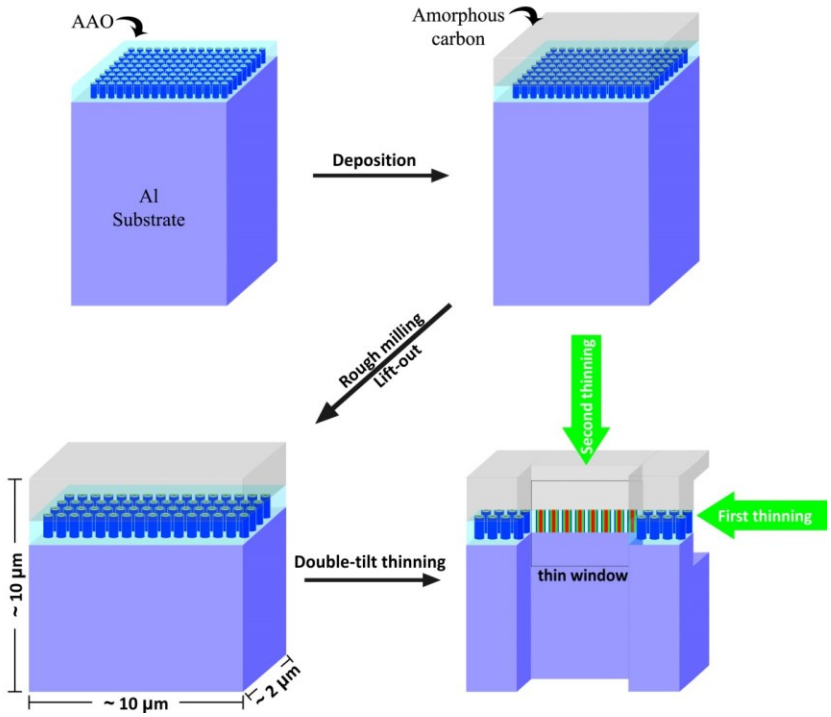

Figure 8–1. Main steps of TEM lamella preparation using focused ion beam equipment.

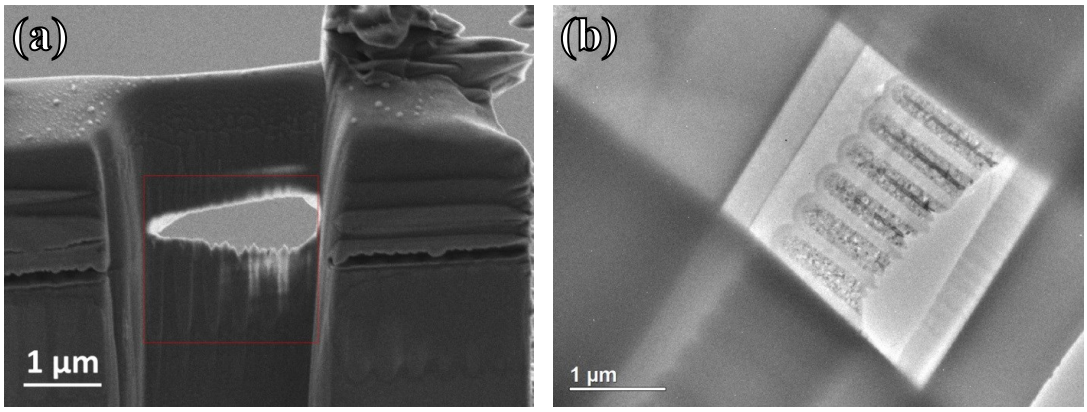

Figure 8–2. (a) 2 kV SE image of the lamella after double-tilt thinning. The image was acquired by using Everhart-Thornley detector. The thin window is indicated by the red rectangle. (b) 300 kV TEM image showing six nanowires within the thin window

8.3. Results and Discussion

The nonlithographic technique for achieving the highly-ordered RRAM device arrays starts from the fabrication of the AAO template. Perfect ordered porous AAO templates were prepared by using anodization of pre-patterned Al foil according to some of previous work.[14, 20, 31, 92, 387] The pre-patterned Al foil was obtained through imprinting of a Ni nanopillars stamp that is replicated from a silicon master mold with perfectly ordered nanocave arrays in a square lattice with lattice period of 400 nm. It should be noted that in this case the defect-free area was only limited by the sizes of the mold and the hydraulic pressure machine. Then the AAO template with nanopore arrays was obtained by using the anodic oxidization of the imprinted aluminum foil. In other words, the device array can be fabricated in a large area with perfect order. The length of the nanopores is dependent on the anodization time and the diameter of the nanopores can be controlled by the pore-widening process. Figure 8-3a, b show the typical scanning electron microscopy (SEM) images of the nanopore arrays with diameter 250 and 300 nm respectively. Increasing the length of the nanopores means increasing the channel width and, therefore, reducing the sheet resistance, which is helpful to reduce the power consumption. However, the increasing of the nanopore length will hinder the miniaturization and integration of the

devices. Hence, the nanopore length is controlled around 1.8 μm here. Two electrodes and the active material were deposited successively by using ALD technique, resulting in a conductive shell of TiN nanotube, an active material TiO_2 nanotube array and a conducting core of Pt nanowire array.[14, 75, 388]

Figure 8-3c-g show the SEM images of top view of the samples after every step, corresponding to c) the AAO template, d) after deposition of TiN layer forming a TiN nanotube array (process A in Figure 8-3j), e) after ion-milling to remove TiN on the surface for separating every TiN nanotube and every device (process B in Figure 8-3j), f) after deposition of TiO_2 layer giving a TiO_2 nanotube array located at the inner TiN nanotube (process C in Figure 8-3j), g) after deposition of Pt layer forming a Pt nanowire array inside of the TiO_2 nanotube (process D in Figure 8-3j). Figure 8-3h shows a clear image of the core-shell nanotube/nanowire arrays consisting of three materials TiN, TiO_2 and Pt after using etching of ion milling. The photographs of the samples after every deposition were shown in Figure 8-4. Through this process, the nanostructure array can be fabricated at the same density of the nanopores of the template in an area as large as the mold with perfect order.

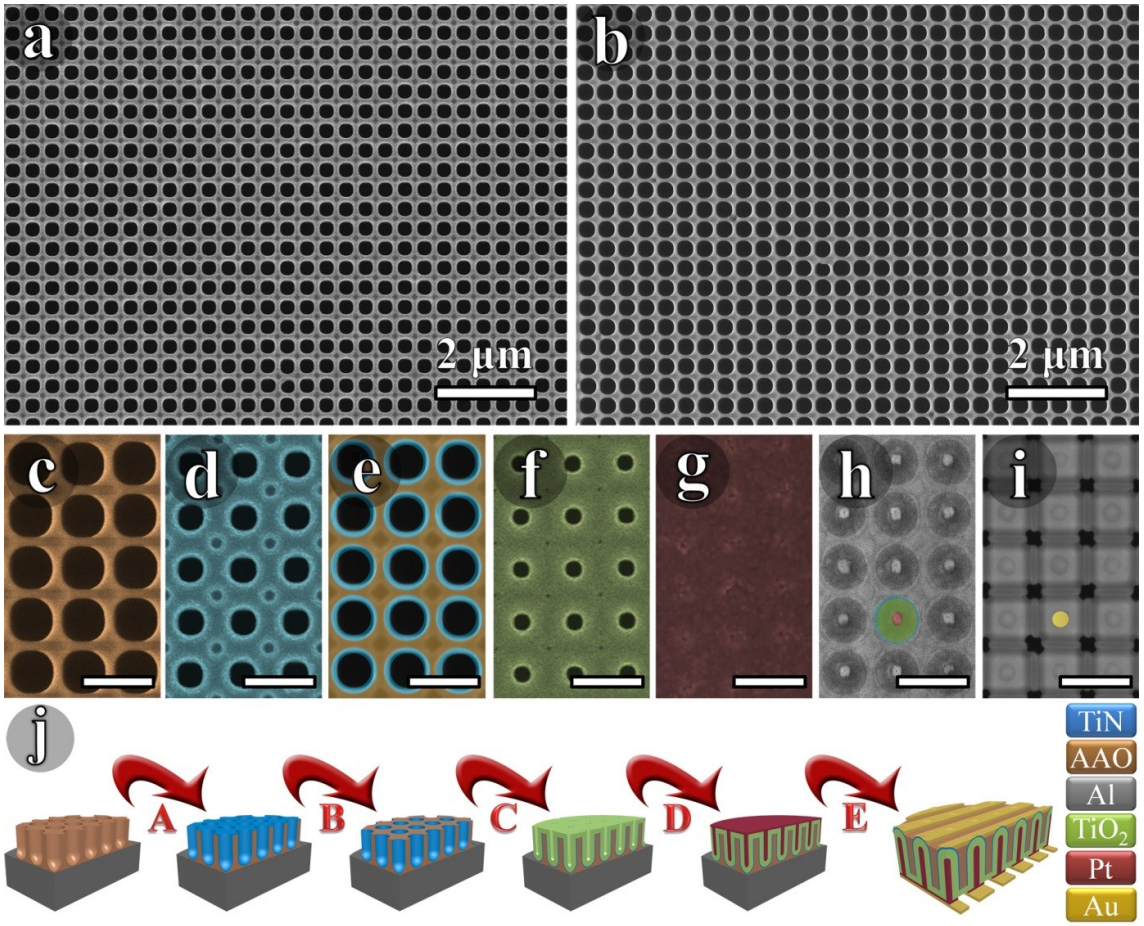

Figure 8–3. Top view of SEM images of as prepared AAO template depicted the perfect array of nanopores with the controllable diameter of (a) 250 and (b) 300 nm ((c) magnified SEM image), respectively. SEM images of the sample (d) after deposition of TiN, (e) after surface etching, (f) after deposition of TiO_2, (g) after deposition of Pt, (h) after surface etching to display the core-shell nanostructure of TiN, TiO_2 and Pt, respectively. (i) SEM image of the backside of the sample after removing the Al and the barrier layer, showing the individual TiN nanotube shell. Scale bars of (c-i) is 500 nm. (j) Schematic outline of the fabrication processes of TiN@TiO_2@Pt core-shell nanotube/nanowire arrays by template-assisted ALD technique.

Figure 8-5a shows a typical SEM image of the freestanding nanostructure array. In this case, every core-shell nanotube/nanowire represents one device consisting two electrodes and one active material. By using ion-milling etching, the cross-sectional view of every nanotube/nanowire is shown in Figure 8-5b. Such a device configuration can give a device array with density as high as the density of the nanopores (10^8~10^9 cm^{-2}). From Figure 8-3h and Figure 8-5b, it is difficult to distinguish the TiN nanotube from the TiO_2 nanotube, indicating that a good interface is formed between them (further proofs can be found

below). Then the aluminum and alumina barrier layer at the backside were removed to expose the electrode array of TiN, as shown in Figure 8-3i. To protect the core-shell nanotube/nanowire array and the supportive AAO framework during the etching processes, the samples were fixed onto ITO glass with connecting ITO and Pt electrode by Ag paste. Finally, in order to measure the device array by using a probe station, an Au layer was deposited on the top surface of the TiN side, shown as process E in Figure 8-3j.

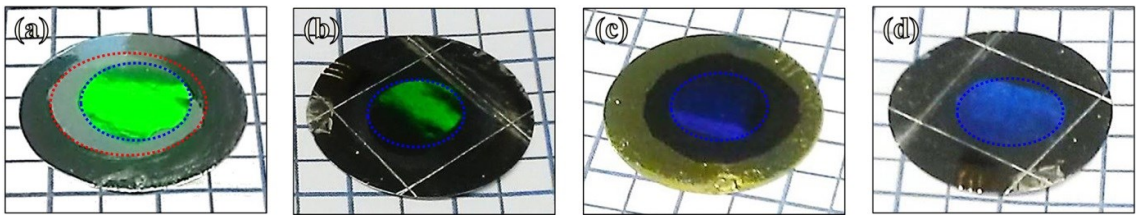

Figure 8–4. Photographs of the TiN@TiO_2@Pt nanotube/nanowire arrays. (a) As prepared AAO membrane, the area inside the blue marked region is printed area (perfect ordered nanopore arrays), the area between red and blue marked region is the normal self-organized AAO membrane. (b) After 1700 cycles of TiN deposition by ALD. (c) After 1200 cycles of TiO_2 deposition by ALD. (d) After 500 cycles of Pt deposition by ALD.

Figure 8-5c shows a cross-sectional SEM image of the freestanding TiN@TiO_2@Pt nanostructure array, indicating a length of 1.8 μm that is coincident with the length of the nanopores. The inset displays the energy dispersive X-ray spectrometry (EDX) line-scan profile of the cross-section nanowire arrays. From the EDX spectra, it is clear that a core-shell nanostructure was obtained, consisting a TiN nanotube shell, a Pt nanowire core and a TiO_2 nanotube between them. The EDX line-scan profile (Figure 8-6) of a single core-shell nanostructure clearly confirms the formation of the desired materials and the thickness of TiN, TiO_2 and Pt are 30, 70 and 28 nm (diameter of Pt nanowire is about 55 nm) respectively, in a good agreement with the ALD techniques reported in previous work.[14, 75, 388] Figure 8-5d shows the X-ray diffraction (XRD) pattern of the as-prepared core-shell nanostructure arrays. The TiN nanotube can be identified to osbornite phase and the main diffraction peaks at 36.6°, 42.5° and 61.8° can be indexed to (111), (200) and (222)

orientations, respectively. The TiO_2 nanotube belongs to anatase phase and the highest intensity diffraction peak at 25.3° can be indexed to face (101). The highest intensity diffraction peak of Pt nanowire was oriented at 39.4°, which can be assigned to face (111) of the Pt. The high intensities of the XRD patterns suggest that the three materials are highly crystalline.

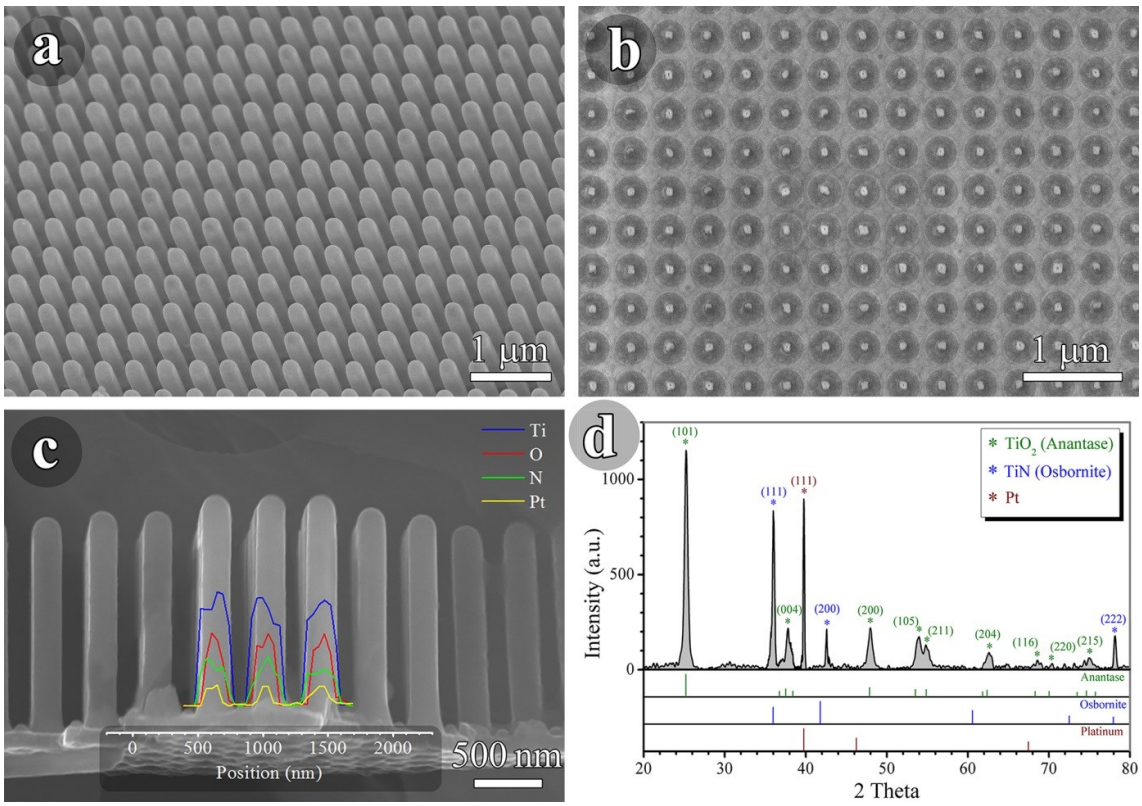

Figure 8–5. (a-b) Top view SEM images of core-shell nanotube/nanowire array of TiN@TiO_2@Pt: (a) freestanding and (b) after etching to display the core-shell nanostructures without removal of the template. (c) Cross-sectional SEM images of freestanding core-shell nanotube/nanowire array of TiN@TiO_2@Pt with inset of EDX line-scan profile. (d) XRD patterns of TiN@TiO_2@Pt core-shell nanotube/nanowire arrays with standard XRD patterns of each component from Crystallography Open Database (COD).

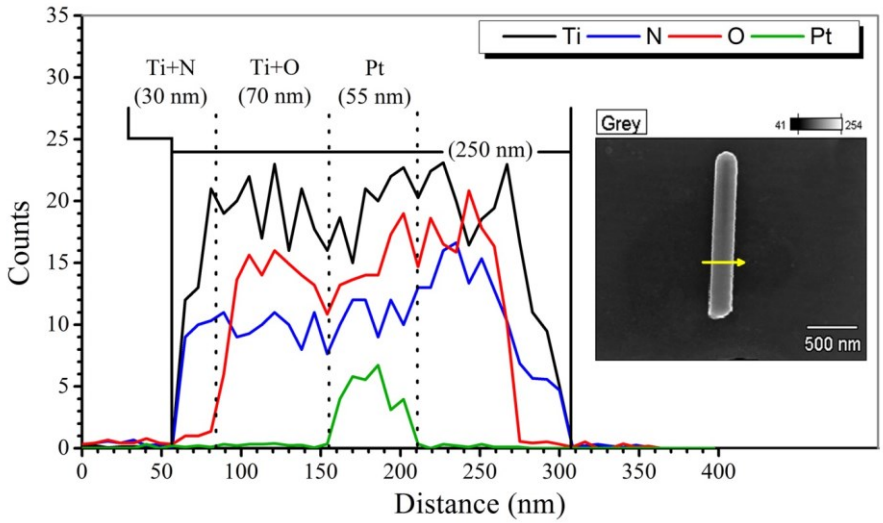

Figure 8–6. EDX line-scan profile of the single nanotube/nanowire along the line in the SEM image (inset).

The composition and the structural information of the core-shell nanostructure were further examined by transmission electron microscopy (TEM). Figure 8-7a shows a cross-section TEM image of one individual core-shell nanotube/nanowire, which consists of three materials inside of the nanopores of the perfectly ordered AAO template. The intensity profile across the nanostructures in the inset of Figure 8-7a indicates that the thicknesses of TiN, TiO_2 and Pt layers were 30, 70 and 28 nm, respectively, which is coincident with the EDX measurement. It should be noted that the surface of every layer is very smooth, which is indisputable for ALD deposition and can be observed in the cross-sectional SEM images (Figure 8-3 and 8-5).

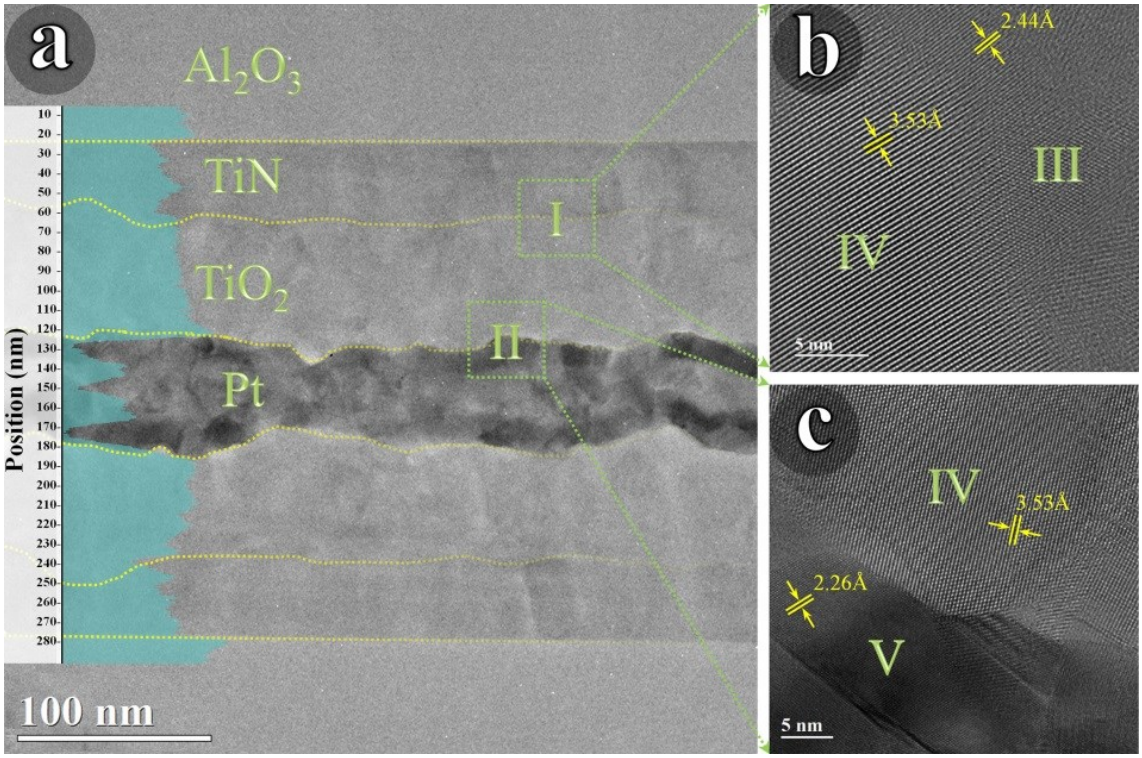

Figure 8–7. (a) Cross-sectional TEM images of one individual nanostructure containing an Al_2O_3 nanopore, a TiN nanotube, a TiO_2 nanotube and a Pt nanowire. HRTEM images of (b) area I showing the interface between TiN and TiO_2, and (c) area II showing the interface between TiO_2 and Pt.

Figure 8-7b, c presents the high-resolution transmission electron microscopy (HRTEM) images of the two interfacial areas of TiN/TiO_2 (the area I in Figure 8-7a) and TiO_2/Pt (area II in Figure 8-7a). The HRTEM images indicate that the three materials are highly crystalline with clear crystal lattice fringes. The HRTEM images further proved that the components of the three areas are TiN, TiO_2 and Pt respectively. The facet distance of area III is 2.44 Å, which can be indexed to the TiN (111) facet with an interplanar spacing of 2.49 Å by using the crystal structure of refcode 1011099 from the COD. The facet distance of area IV is 3.53 Å, belonging to the TiO_2 (101) facet that has an interplanar spacing of 3.52 Å by using the crystal structure of TiO_2 (refcode 7206075 from the COD). On the other hand, area V has a facet distance of 2.26Å, which is close to the interplanar spacing of Pt (111) facet (2.27 Å, refcode 9008480 from the COD). Moreover, a clear interfacial layer was observed at the interface between TiN and TiO_2. This interfacial layer

probably was generated from the surface of TiN due to the exposure to oxygen for the deposition of TiO_2.

Figure 8-8a, b present the magnified HRTEM images of the interfacial area (the area I in Figure 8-7a) between TiN and TiO_2, where the overlapping of the crystal lattice fringes of TiN and TiO_2 can be clearly observed. The overlapping interfacial layer is as large as 3 nm. The FFT pattern and the inverse FFT images support the formation of the thick interfacial layer between the TiN electrode and TiO_2 (Figure 8-9, supporting information). Such interface is expected to reduce the resistance (potential barrier, contact resistance) between the electrode and the semiconductor and, therefore, facilitate the charge transport between them.

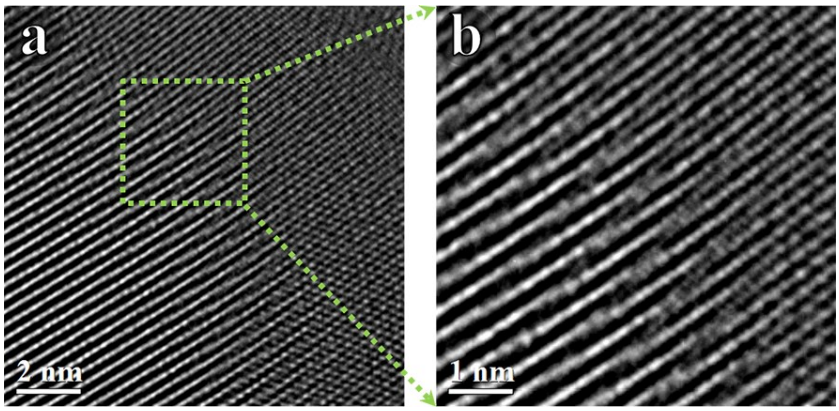

Figure 8–8. (a, b) HRTEM images of the interface between TiN and TiO_2.

To demonstrate the potential application of this kind of nanostructure for RRAM application, an Au film was deposited on the top surface to connect with the TiN electrode (process E in Figure 8-3j). It should be noted for a practical application, two cross electrode arrays deposited on both side of the sample for connection with TiN and Pt electrode are feasible (by using photolithography or electron beam lithography) and necessary to achieve a device array with a same density of the nanostructures (nanopores). Such a high density of nanostructure array (10^8~10^9 cm^{-2}) makes the high density of three-

dimensional (3-D) vertical RRAM array possible because the device size is no longer limited by the lithographic half-pitch as in two-dimensional (2-D) architectures.

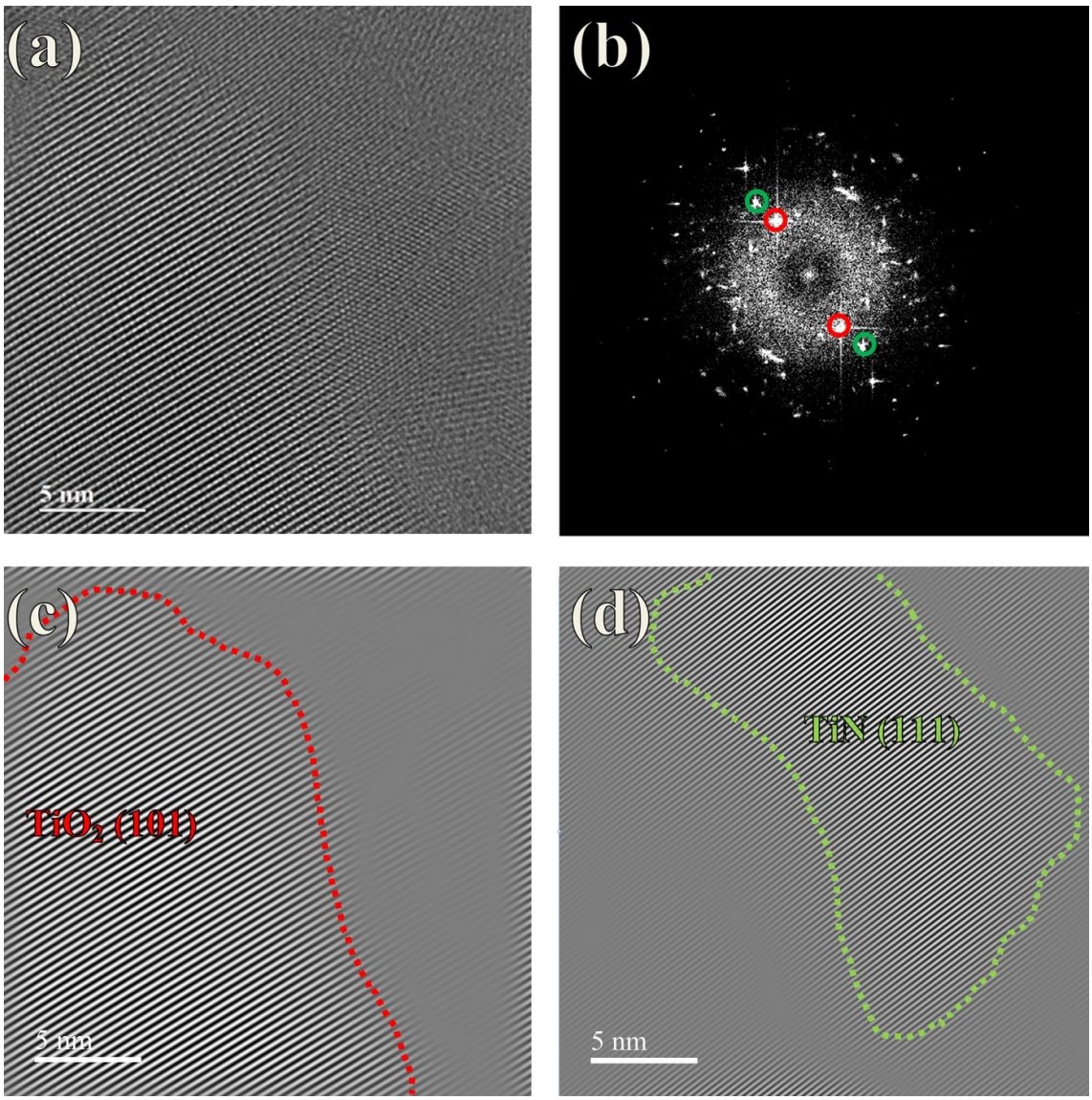

Figure 8–9. (a) HRTEM image of the interfacial layer between TiN and TiO_2. (b) FFT pattern of image (a). (c, d) The inverse FFT images calculated from the peaks in the image (b).

Figure 8-10 shows an asymmetrical I-V curves (semilogarithmic) based on the TiN@TiO_2@Pt nanostructure array (diameter of the nanopores is about 250 nm for S1 and 300 nm for S2), indicating a sharp increase of the current around the potential of -1.5 and -1.4 mV in reverse bias (or +1.2 and +1.1 mV for forward), respectively. The asymmetrical property can be ascribed to the asymmetrical device configuration. The reports have shown

that the bipolar resistive switching behavior is due to the migration of oxygen ions.[389-391] When a positive electrical field is applied to the TiN electrode, the oxygen ions, generated from the interfacial area between TiN and TiO_2 due to the injection of the electrons, will be attracted to the TiN electrode, resulting in an oxygen reservoir in the TiN electrode and leaving oxygen vacancies in the conducting channel. If the electric potential (set potential) is higher than the threshold potential, the device switches into the low resistance state (LRS) from the high resistance state (HRS). On the contrary, if a reverse bias (reset potential) is applied on TiN electrode, the oxygen ions are pushed from the TiN electrode and fill in the oxygen vacancies in the conducting channel, leading to a high resistance state afterward. Because the oxygen ions fundamentally existed in the TiN/TiO_2 interface and oxygen reservoir was not observed in the Pt/TiO_2 interface (also see Figure 8-7),[390, 392, 393] the set potential (+1.2 or +1.1 mV) is lower than the reset potential (-1.5 or -1.4 mV). However, both millivolt-scaled threshold potential are amazing which makes it possible to apply the core-shell nanostructures for ultralow power consumption RRAM. Such a low threshold potential probably can be attributed to the high crystallinity and the perfect interfacial effect between the TiN electrode and the TiO_2 active material (Figure 8-7 and 4). The device formed a complete switching cycle when scanning back, indicating the reversible electrical bistable switching property of the nanostructures.

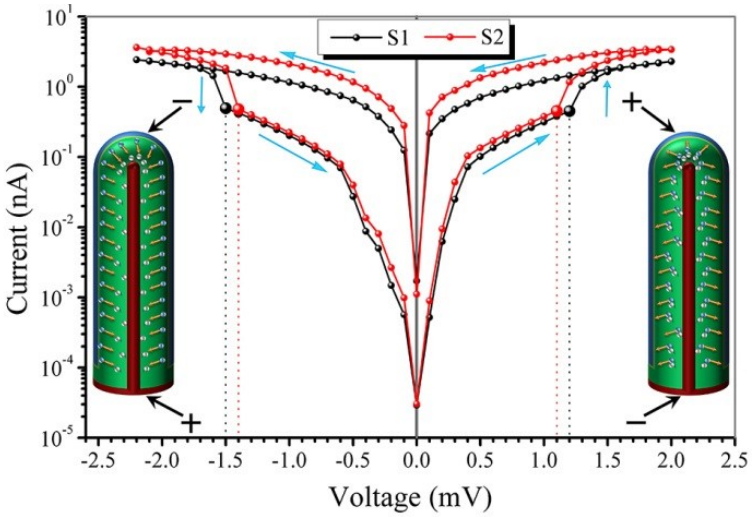

Figure 8–10. Semilogarithmic I–V characteristics as a comparing of RS behavior of two different diameters of TiN@TiO_2@Pt core-shell nanotube/nanowire. The insets are a schematic description of the oxygen ion (blue point) and vacancy (white point) distribution inside TiO_2. The polarity of the applied voltage during each stage represented by + and -.

As mentioned above, compared with the nanodot arrays, the increased channel width by using the 3-D nanostructures is helpful to decrease the sheet resistance and thereby to reduce the power consumption. It is clear that besides of the material itself, its morphology and structural packing, the channel length and width also affect the sheet resistance. In order to verify this assumption, here two kinds of samples with a different diameter of the nanopores (same length of the nanopores and the same thickness of the active materials), i.e. having different channel width, were investigated, shown in Figure 8-11. As expected, the sample with larger diameter exhibits a smaller threshold potential of -1.4 (or +1.1) mV (compared with -1.5 (or +1.2) mV). All these results indicate that the ultralow power consumption is due to the high crystal quality of the materials, the perfect interfacial effect between the semiconductor and the electrodes and the suitable device configuration. Figure 8-11a, b show 300 cycles of bipolar resistive switching properties of two different samples with diameter around 250 nm and 300 nm, respectively. Both the HRS and LRS are very stable, indicating the excellent electrical stability of the core-shell nanostructures. Both the two samples show high repeatability of the switching behavior even after 300 cycles. The

high electrical stability for both low resistance state (LRS) and high resistance state (HRS) at 0.3 mV are shown in Figure 8-11c. There is no significant variation even after cycled 300 times. In order to demonstrate the potential application of these high density core-shell nanostructures for memory device, writing-reading-erasing-reading cycles were applied onto the device. As shown in Figure 8-11d, the simultaneous response of the current to the writing and erasing process and the high on/off ratio (LRS/HRS conductivity ratio) indicate its capability for high-speed memory applications. Moreover, the switching process from OFF state to ON state is reproducible without any obvious variation, which confirms the stability of switching behavior.

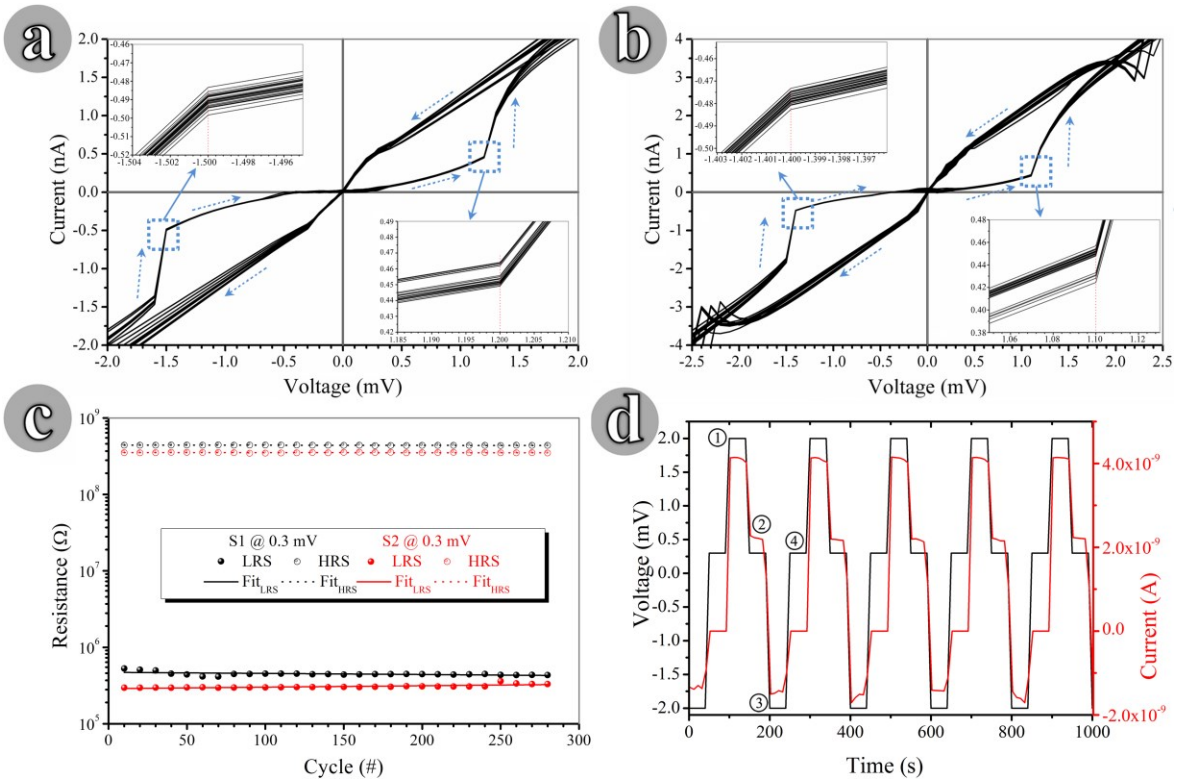

Figure 8–11. (a, b) Typical I–V curves (300 cycles) of single TiN@TiO_2@Pt core-shell nanostructure with the diameter of 250 and 300 nm, respectively. The inset shows the low threshold potential of SET and ReSET stages. (c) Endurance performance of TiN@TiO_2@Pt core-shell nanostructure, showing the high stability for both HRS and LRS. (d) Writing-reading-erasing-reading cycles of TiN@TiO_2@Pt memory device. The writing, reading, erasing and reading potentials are 2.0, 0.3, -2.0 and 0.3 mV respectively.

8.4. Conclusion

A core-shell nanowire/nanotube array with a density of as high as 10^8~10^9 cm^{-2} has been fabricated using a template-assisted technique. Both the electrodes (TiN and Pt) and semiconductor (TiO_2) could be fabricated by using conformal ALD technique. The potential application of this core-shell nanostructure array for RRAM was presented. Such 3D vertical RRAM array can provide high device density with the same density of the nanostructures which only needs one-time lithography for patterning the nanopores. Because of the high crystallinity of the materials, the large contact area and the intimate interface (3 nm) between the TiN and TiO_2, ultralow voltage operation (mV magnitude) and ultralow power consumption (pW magnitude) were achieved. It should be noted that many kinds of materials can be fabricated by using the procedure similar to the present method. The materials used here are to demonstrate the template-assisted technique for creating a non-volatile memory technology as proof of concept. This cost-effective method to fabricate such kind of 3D electronic device arrays with the capability to adjust the device densities can be extended to other applications of the next generation nanodevice technology.

9. Bibliography

[1] K. Kono, K. Takeda, X. Li, E. Yuba, A. Harada, T. Ozaki and S. Mori, *RSC Advances*, 2014, 4, 27811.

[2] D. J. Lewis and Z. Pikramenou, *Coordination Chemistry Reviews*, 2014, 273–274, 213.

[3] C. D. Walkey, J. B. Olsen, F. Song, R. Liu, H. Guo, D. W. H. Olsen, Y. Cohen, A. Emili and W. C. Chan, *ACS Nano*, 2014, 8, 2439.

[4] Y.-C. Liang, W.-K. Liao and X.-S. Deng, *Journal of Alloys and Compounds*, 2014, 599, 87.

[5] F. Priolo, T. Gregorkiewicz, M. Galli and T. F. Krauss, *Nat. Nanotechnol.*, 2014, 9, 19.

[6] P. L. Hernández-Martínez, A. O. Govorov and H. V. Demir, *J. Phys. Chem. C*, 2014, 118, 4951.

[7] M. L. Brongersma, Y. Cui and S. Fan, *Nat. Mater.*, 2014, 13, 451.

[8] N. Serpone, D. Lawless and R. Khairutdinov, *J. Phys. Chem.*, 1995, 99, 16646.

[9] Y.-H. Chang, C.-M. Liu, H.-E. Cheng and C. Chen, *ACS Appl. Mater. Interfaces*, 2013, 5, 3549.

[10] D. V. Bavykin, S. N. Gordeev, A. V. Moskalenko, A. A. Lapkin and F. C. Walsh, *The journal of physical chemistry. B*, 2005, 109, 8565.

[11] H. J. Fan, P. Werner and M. Zacharias, *small*, 2006, 2, 700.

[12] M. Li and J. C. Li, *Materials Letters*, 2006, 60, 2526.

[13] N. Haberkorn, J. S. Gutmann and P. Theato, *ACS Nano*, 2009, 3, 1415.

[14] L. Wen, Y. Mi, C. Wang, Y. Fang, F. Grote, H. Zhao, M. Zhou and Y. Lei, *Small*, 2014, 10, 3162.

[15] F. Rumiche, H. Wang, W. Hu, J. Indacochea and M. Wang, *Sensors and Actuators B: Chemical*, 2008, 134, 869.

[16] S. Chen, O. Khor, M. Liao and C. Chung, *Sensors and Actuators B: Chemical*, 2014, 199, 384.

[17] X. Z. Chen, Q. Li, X. Chen, X. Guo, H. X. Ge, Y. Liu and Q. D. Shen, *Adv. Funct. Mater.*, 2013, 23, 3124.

[18] L. Jiang, Y. Sun, C. Nowak, A. Kibrom, C. Zou, J. Ma, H. Fuchs, S. Li, L. Chi and X. Chen, *ACS Nano*, 2011, 5, 8288.

[19] M. J. Klein, M. Guillaumée, B. Wenger, L. A. Dunbar, J. Brugger, H. Heinzelmann and R. Pugin, *Nanotechnology*, 2010, 21, 205301.

[20] Z. Zhan and Y. Lei, *ACS Nano*, 2014, 8, 3862.

[21] A. S. Maria Chong, L. K. Tan, J. Deng and H. Gao, *Adv. Funct. Mater.*, 2007, 17, 1629.

[22] T. S. Kustandi, W. W. Loh, H. Gao and H. Y. Low, *ACS Nano*, 2010, 4, 2561.

[23] W. Wang, D. Li, M. Tian, Y.-C. Lee and R. Yang, *Appl. Surf. Sci.*, 2012, 258, 8649.

[24] M. Zhou, J. Bao, Y. Xu, J. Zhang, J. Xie, M. Guan, C. Wang, L. Wen, Y. Lei and Y. Xie, *ACS Nano*, 2014, 8, 7088.

[25] M. L. Hammock, A. N. Sokolov, R. M. Stoltenberg, B. D. Naab and Z. Bao, *ACS Nano*, 2012, 6, 3100.

[26] S. Yang and Y. Lei, *Nanoscale*, 2011, 3, 2768.

[27] B. D. Gates, Q. Xu, M. Stewart, D. Ryan, C. G. Willson and G. M. Whitesides, *Chemical reviews*, 2005, 105, 1171.

[28] M. E. Warkiani, A. A. S. Bhagat, B. L. Khoo, J. Han, C. T. Lim, H. Q. Gong and A. G. Fane, *ACS Nano*, 2013, 7, 1882.

[29] C. Wang, L. Wen, T. Kups, Y. Mi, R. Vellacheri, Y. Fang, P. Schaaf, H. Zhao and Y. Lei, *J. Mater. Chem. C*, 2013, 1, 8003.

[30] F. Grote and Y. Lei, *Nano Energy*, 2014, 10, 63.

[31] Z. Zhan, R. Xu, Y. Mi, H. Zhao and Y. Lei, *ACS Nano*, 2015, 9, 4583.

[32] Z. Chen, Y. Lei, H. Chew, L. Teo, W. Choi and W. Chim, *J. Cryst. Growth*, 2004, 268, 560.

[33] K. Kim, M. Kim and S. M. Cho, *Materials Chemistry and Physics*, 2006, 96, 278.

[34] X. Meng, M. N. Banis, D. Geng, X. Li, Y. Zhang, R. Li, H. Abou-Rachid and X. Sun, *Applied Surface Science*, 2013, 266, 132.

[35] H. Zhao, C. Wang, R. Vellacheri, M. Zhou, Y. Xu, Q. Fu, M. Wu, F. Grote and Y. Lei, *Adv. Mater.*, 2014, 26, 7654.

[36] Y. Lei, S. Yang, M. Wu and G. Wilde, *Chemical Society reviews*, 2011, 40, 1247.

[37] Y. Lei, W. Cai and G. Wilde, *Prog. Mater. Sci.*, 2007, 52, 465.

[38] M. Wu, L. Wen, Y. Lei, S. Ostendorp, K. Chen and G. Wilde, *Small*, 2010, 6, 695.

[39] S. Zhao, H. Roberge, A. Yelon and T. Veres, *J. Am. Chem. Soc.*, 2006, 128, 12352.

[40] Y. Lei, C. Liang, Y. Wu, L. Zhang and Y. Mao, *J. Vac. Sci. Technol. B*, 2001, 19, 1109.

[41] Y.-H. Chang, C.-M. Liu, C. Chen, H.-E. Cheng and T.-C. Lu, *J. Electrochem. Soc.*, 2012, 159, K136.

[42] Y. Lei and W.-K. Chim, *Chem. Mater.*, 2005, 17, 580.

[43] Y. Lei, W. Chim, J. Weissmüller, G. Wilde, H. Sun and X. Pan, *Nanotechnology*, 2005, 16, 1892.

[44] M. Ni, M. K. Leung, D. Y. Leung and K. Sumathy, *Renew Sust. Energ Rev.*, 2007, 11, 401.

[45] W.-J. Yin, H. Tang, S.-H. Wei, M. M. Al-Jassim, J. Turner and Y. Yan, *Phys. Rev. B*, 2010, 82, 45106.

[46] Y. C. Pu, G. Wang, K. D. Chang, Y. Ling, Y. K. Lin, B. C. Fitzmorris, C. M. Liu, X. Lu, Y. Tong, J. Z. Zhang, Y. J. Hsu and Y. Li, *Nano Lett.*, 2013, 13, 3817.

[47] I. S. Cho, J. Choi, K. Zhang, S. J. Kim, M. J. Jeong, L. Cai, T. Park, X. Zheng and J. H. Park, *Nano Lett.*, 2015, 15, 5709.

[48] J. Shi and X. Wang, *Energy Environ. Sci.*, 2012, 5, 7918.

[49] Y. W. Chen, J. D. Prange, S. Duhnen, Y. Park, M. Gunji, C. E. Chidsey and P. C. McIntyre, *Nat. Mater.*, 2011, 10, 539.

[50] B. Seger, S. D. Tilley, T. Pedersen, P. C. Vesborg, O. Hansen, M. Grätzel and I. Chorkendorff, *J. Mater. Chem. A*, 2013, 1, 15089.

[51] A. Fujishima and K. Honda, *Nature*, 1972, 238, 37.

[52] M. Grätzel, *Nature*, 2001, 414, 338.

[53] F. E. Osterloh, *Chem. Soc. Rev.*, 2013, 42, 2294.

[54] S. Bai, J. Jiang, Q. Zhang and Y. Xiong, *Chem. Soc. Rev.*, 2015, 44, 2893.

[55] W. Schmittinger and A. Vahidi, *J. Power Sources*, 2008, 180, 1.

[56] D. W. Boukhvalov, Y.-W. Son and R. S. Ruoff, *ACS Catal.*, 2014, 4, 2016.

[57] C. Tang, N. Cheng, Z. Pu, W. Xing and X. Sun, *Angew. Chem. Int. Ed. Engl.*, 2015, 54, 9351.

[58] M. T. Mayer, C. Du and D. Wang, *J. Am. Chem. Soc.*, 2012, 134, 12406.

[59] M. Xie, X. Fu, L. Jing, P. Luan, Y. Feng and H. Fu, *Adv. Energy Mater.*, 2014, 4, 1300995.

[60] Z. Tachan, I. Hod and A. Zaban, *Adv. Energy Mater.*, 2014, 4, 1301249.

[61] M. G. Walter, E. L. Warren, J. R. McKone, S. W. Boettcher, Q. Mi, E. A. Santori and N. S. Lewis, *Chem. Rev.*, 2010, 110, 6446.

[62] C. Liu, N. P. Dasgupta and P. Yang, *Chem. Mater.*, 2013, 26, 415.

[63] P. Zhou, J. Yu and M. Jaroniec, *Adv. Mater.*, 2014, 26, 4920.

[64] F. Keller, M. Hunter and D. Robinson, *J. Electrochem. Soc.*, 1953, 100, 411.

[65] H. Masuda and K. Fukuda, *Science*, 1995, 268, 1466.

[66] Y. Lei, L. Zhang, G. Meng, G. Li, X. Zhang, C. Liang, W. Chen and S. Wang, *Appl. Phys. Lett.*, 2001, 78, 1125.

[67] Y. Sui, D. Acosta, J. Gonzalez-Leon, A. Bermudez, J. Feuchtwanger, B. Cui, J. Flores and J. Saniger, *J. Phys. Chem. B*, 2001, 105, 1523.

[68] Y. Xia, P. Yang, Y. Sun, Y. Wu, B. Mayers, B. Gates, Y. Yin, F. Kim and H. Yan, *Adv. Mater.*, 2003, 15, 353.

[69] Y. Lei, L. Teo, K. Yeong, Y. See, W. K. Chim, W. K. Choi and J. Thong, 2003.

[70] J. Elam, D. Routkevitch, P. Mardilovich and S. George, *Chem. Mater.*, 2003, 15, 3507.

[71] J. P. O'Sullivan and G. C. Wood, *Proc. Roy. Soc. Lond. A*, 1970, 317, 511.

[72] K. Nielsch, J. Choi, K. Schwirn, R. B. Wehrspohn and U. Gösele, *Nano Lett.*, 2002, 2, 677.

[73] R. C. Alkire, Y. Gogotsi, P. Simon and A. Eftekhari, *Nanostructured materials in electrochemistry*, John Wiley & Sons, 2008.

[74] K. Ebihara, H. Takahashi and M. Nagayama, *J. Met. Finish. Soc. Jpn*, 1983, 34, 548.

[75] A. Al-Haddad, Z. Wang, R. Xu, H. Qi, R. Vellacheri, U. Kaiser and Y. Lei, *J. Phys. Chem. C*, 2015, 119, 16331.

[76] W. Lee and S.-J. Park, *Chemical reviews*, 2014, 114, 7487.

[77] G. Sulka and K. Parkoła, *Electrochim. Acta*, 2007, 52, 1880.

[78] L. Zaraska, W. J. Stępniowski, M. Jaskuła and G. D. Sulka, *Applied Surface Science*, 2014, 305, 650.

[79] C. Larsson, P. Thomsen, B.-O. Aronsson, M. Rodahl, J. Lausmaa, B. Kasemo and L. Ericson, *Biomaterials*, 1996, 17, 605.

[80] S. Chu, K. Wada, S. Inoue, M. Isogai, Y. Katsuta and A. Yasumori, *J. Electrochem. Soc.*, 2006, 153, B384.

[81] S. Tajima, N. Baba, K. Shimizu and I. Mizuki, *Active and Passive Electronic Components*, 1976, 3, 91.

[82] V. Sadasivan, C. Richter, L. Menon and P. Williams, *AIChE J.*, 2005, 51, 649.

[83] A. Mozalev, I. Mozaleva, M. Sakairi and H. Takahashi, *Electrochim. Acta*, 2005, 50, 5065.

[84] S. Ono, M. Saito and H. Asoh, *Electrochim. Acta*, 2005, 51, 827.

[85] S. Ono, A. Oide and H. Asoh, *Electrochim. Acta*, 2007, 52, 2898.

[86] W. De Azevedo, D. De Carvalho, H. Khoury, E. De Vasconcelos and E. Da Silva, *Materials Science and Engineering: B*, 2004, 112, 171.

[87] A. Al-Haddad, Z. Zhan, C. Wang, S. Tarish, R. Vellacheria and Y. Lei, *ACS Nano*, 2015, 9, 8584.

[88] S. A. Tarish, Z. Wang, A. Al Haddad, C. Wang, A. Ispas, H. Romanus, P. Schaaf and Y. Lei, *J. Phys. Chem. C*, 2014.

[89] S. Shingubara, *Journal of Nanoparticle Research*, 2003, 5, 17.

[90] S. Ono and N. Masuko, *Surf. Coat. Technol.*, 2003, 169, 139.

[91] G. Wood, J. O'sullivan and B. Vaszko, *J. Electrochem. Soc.*, 1968, 115, 618.

[92] Y. Xu, M. Zhou, L. Wen, C. Wang, H. Zhao, Y. Mi, L. Liang, Q. Fu, M. Wu and Y. Lei, *Chem. Mater.*, 2015, 27, 4274.

[93] J. S. Suh and J. S. Lee, *Appl. Phys. Lett.*, 1999, 75, 2047.

[94] S. Prasad and J. Quijano, *Biosensors and Bioelectronics*, 2006, 21, 1219.

[95] H.-J. Oh, G.-S. Park, J.-G. Kim, Y. Jeong and C.-S. Chi, *Materials chemistry and physics*, 2003, 82, 331.

[96] H. Uchi, T. Kanno and R. Alwitt, *J. Electrochem. Soc.*, 2001, 148, B17.

[97] G. Wood, P. Skeldon, G. Thompson and K. Shimizu, *J. Electrochem. Soc.*, 1996, 143, 74.

[98] S.-M. Moon and S.-I. Pyun, *Electrochim. Acta*, 1999, 44, 2445.

[99] H. Masuda and M. Satoh, *Jpn. J. Appl. Phys.*, 1996, 35, L126.

[100] K. R. Hebert, H. Wu, T. Gessmann and K. Lynn, *J. Electrochem. Soc.*, 2001, 148, B92.

[101] T. Martin and K. R. Hebert, *J. Electrochem. Soc.*, 2001, 148, B101.

[102] F. Li, L. Zhang and R. M. Metzger, *Chem. Mater.*, 1998, 10, 2470.

[103] J. W. Diggle, T. C. Downie and C. Goulding, *Chemical Reviews*, 1969, 69, 365.

[104] A. Despić and V. P. Parkhutik, in *Modern Aspects of Electrochemistry No. 20*, Springer, 1989, 401.

[105] G. E. J. Poinern, N. Ali and D. Fawcett, *Materials*, 2011, 4, 487.

[106] H. Masuda, F. Hasegwa and S. Ono, *J. Electrochem. Soc.*, 1997, 144, L127.

[107] O. Jessensky, F. Müller and U. Gösele, *Appl. Phys. Lett.*, 1998, 72, 1173.

[108] A. Li, F. Müller, A. Birner, K. Nielsch and U. Gösele, *J. Appl. Phys.*, 1998, 84, 6023.

[109] D. Routkevitch, T. Bigioni, M. Moskovits and J. M. Xu, *J. Phys. Chem.*, 1996, 100, 14037.

[110] K. Nielsch, F. Müller, A.-P. Li and U. Gösele, *Adv. Mater.*, 2000, 12, 582.

[111] H. Cao, Z. Xu, H. Sang, D. Sheng and C. Tie, *Adv. Mater.*, 2001, 13, 121.

[112] C. Mu, Y. X. Yu, R. Wang, K. Wu, D. Xu and G. L. Guo, *Adv. Mater.*, 2004, 16, 1550.

[113] G. Che, B. B. Lakshmi, E. R. Fisher and C. R. Martin, *Nature*, 1998, 393, 346.

[114] S. Grimm, R. Giesa, K. Sklarek, A. Langner, U. Gösele, H.-W. Schmidt and M. Steinhart, *Nano Lett.*, 2008, 8, 1954.

[115] M. Wu, L. Wen, Y. Lei, S. Ostendorp, K. Chen and G. Wilde, *Small*, 2010, 6, 695.

[116] G. Cheng and M. Moskovits, *Adv. Mater.*, 2002, 14, 1567.

[117] Q. Guo, X. Mei, H. Ruda, T. Tanaka, M. Nishio and H. Ogawa, *Jpn. J. Appl. Phys.*, 2003, 42, L508.

[118] W. Xu, M. Zheng, G. Ding and W. Shen, *Chem. Phys. Lett.*, 2005, 411, 37.

[119] P. A. Kossyrev, A. Yin, S. G. Cloutier, D. A. Cardimona, D. Huang, P. M. Alsing and J. M. Xu, *Nano Lett.*, 2005, 5, 1978.

[120] L. Wen, Z. Shao, Y. Fang, K. M. Wong, Y. Lei, L. Bian and G. Wilde, *Appl. Phys. Lett.*, 2010, 97, 053106.

[121] U. Malinovskis, R. Poplausks, I. Apsite, R. Meija, J. Prikulis, F. Lombardi and D. Erts, *J. Phys. Chem. C*, 2014, 118, 8685.

[122] N. Lim, Y. Pak, J. T. Kim, Y. Hwang, R. Lee, Y. Kumaresan, N. Myoung, H. C. Ko and G. Y. Jung, *Nanoscale*, 2015, 7, 13489.

[123] G. a. Tai, K. Wang, Z. Sun, J. Yin, S. M. Ng, J. Zhou, F. Yan, C. W. Leung, K. H. Wong and W. Guo, *J. Phys. Chem. C*, 2011, 116, 532.

[124] L. B. Freund and S. Suresh, *Thin film materials: stress, defect formation and surface evolution*, Cambridge University Press, 2004.

[125] U. Helmersson, M. Lattemann, J. Bohlmark, A. P. Ehiasarian and J. T. Gudmundsson, *Thin Solid Films*, 2006, 513, 1.

[126] Z. Wang and S. A. Cohen, *Journal of Vacuum Science & Technology A*, 1999, 17, 77.

[127] A. S. Maria Chong, L. K. Tan, J. Deng and H. Gao, *Adv. Funct. Mater.*, 2007, 17, 1629.

[128] S. B. Clendenning, S. Aouba, M. S. Rayat, D. Grozea, J. B. Sorge, P. M. Brodersen, R. N. Sodhi, Z. H. Lu, C. M. Yip and M. R. Freeman, *Adv. Mater.*, 2004, 16, 215.

[129] S. Matsui and Y. Ochiai, *Nanotechnology*, 1996, 7, 247.

[130] G. M. Whitesides and B. Grzybowski, *Science*, 2002, 295, 2418.

[131] S. Krämer, R. R. Fuierer and C. B. Gorman, *Chemical Reviews*, 2003, 103, 4367.

[132] E. Moyen, W. Wulfhekel, W. Lee, A. Leycuras, K. Nielsch, U. Gösele and M. Hanbücken, *Applied Physics A*, 2006, 84, 369.

[133] W. Lee, E. Moyen, W. Wulfhekel, A. Leycuras, K. Nielsch, U. Gösele and M. Hanbücken, *Applied Physics A*, 2006, 83, 361.

[134] S. Wang, G. J. Yu, J. L. Gong, Q. T. Li, H. J. Xu, D. Z. Zhu and Z. Y. Zhu, *Nanotechnology*, 2006, 17, 1594.

[135] W. Wang, S.-Y. Wang, Y.-L. Gao, K.-Y. Wang and M. Liu, *Materials Science and Engineering: B*, 2006, 133, 167.

[136] Z. Hu, Y. Hu, Q. Chen, X. Duan and L.-M. Peng, *J. Phys. Chem. B*, 2006, 110, 8263.

[137] Y. Wang, K. Zang and S. Chua, *J. Appl. Phys.*, 2006, 100, 054306.

[138] S. Wang, G. Yu, J. Gong, D. Zhu and H. Xia, *Nanotechnology*, 2006, 18, 015303.

[139] X. Liu, J. Luo and J. Zhu, *Nano Lett.*, 2006, 6, 408.

[140] D. Ding, Z. Chen and C. Lu, *Sensors and Actuators B: Chemical*, 2006, 120, 182.

[141] A. Yin, J. H. Kim and J. Xu, in *MRS Proceedings*, Cambridge Univ Press, 2006, 0951.

[142] M. Lahav, E. A. Weiss, Q. Xu and G. M. Whitesides, *Nano Lett.*, 2006, 6, 2166.

[143] S. Kang, P. Su, Y. Park, Y. Saito and F. Prinz, *J. Electrochem. Soc.*, 2006, 153, A554.

[144] W. S. Liao, T. Yang, E. T. Castellana, S. Kataoka and P. S. Cremer, *Adv. Mater.*, 2006, 18, 2240.

[145] A. Zhao, J. Liang, Z. Xiong and Y. Qian, *Chem. Lett.*, 2007, 36, 432.

[146] B. Seo, U. Shaislamov, S.-W. Kim, H.-K. Kim, S. Hong and B. Yang, *Physica E Low Dimens. Syst. Nanostruct.*, 2007, 37, 279.

[147] B. Yan, H. T. Pham, Y. Ma, Y. Zhuang and P. M. Sarro, *Appl. Phys. Lett.*, 2007, 91, 053117.

[148] Z. Wang and M. Brust, *Nanoscale Research Letters*, 2007, 2, 34.

[149] A. P. Robinson, G. Burnell, M. Hu and J. L. MacManus-Driscoll, *Appl. Phys. Lett.*, 2007, 91, 143123.

[150] A. Yin, M. Tzolov, D. Cardimona, L. Guo and J. Xu, *Circuits, Devices & Systems, IET*, 2007, 1, 205.

[151] S. Lee, S. Shin, J. Lee, J. Lee, J. Song, J. Choi, H. Lee and H. Lee, *JOURNAL-KOREAN PHYSICAL SOCIETY*, 2007, 51, 178.

[152] A. Pereira, F. Laplante, M. Chaker and D. Guay, *Adv. Funct. Mater.*, 2007, 17, 443.

[153] X. Jiang, N. Mishra, J. N. Turner and M. G. Spencer, *Nanotechnology, IEEE Transactions on*, 2007, 6, 328.

[154] X. Zhao, S.-K. Seo, U.-J. Lee and K.-H. Lee, *J. Electrochem. Soc.*, 2007, 154, C553.

[155] M. T. Rahman, C.-H. Lai, D. Vokoun and N. N. Shams, *Magnetics, IEEE Transactions on*, 2007, 43, 2133.

[156] B. Seo, U. Shaislamov, S.-W. Kim, H.-K. Kim, B. Yang and S. Hong, *Physica E Low Dimens. Syst. Nanostruct.*, 2007, 37, 274.

[157] P. R. Evans, X. Zhu, P. Baxter, M. McMillen, J. McPhillips, F. D. Morrison, J. F. Scott, R. J. Pollard, R. M. Bowman and J. M. Gregg, *Nano Lett.*, 2007, 7, 1134.

[158] L. K. Tan, A. M. Chong, X. E. Tang and H. Gao, *J. Phys. Chem. C*, 2007, 111, 4964.

[159] E. Rotem, J. M. Shainline and J. M. Xu, *Optics express*, 2007, 15, 14099.

[160] K. Nakayama, K. Tanabe and H. A. Atwater, *Appl. Phys. Lett.*, 2008, 93, 121904.

[161] W. Lee, H. Han, A. Lotnyk, M. A. Schubert, S. Senz, M. Alexe, D. Hesse, S. Baik and U. Gösele, *Nat. Nanotechnol.*, 2008, 3, 402.

[162] R. Mao, S. Lin and C. Tsai, *Nanotechnology*, 2008, 20, 025301.

[163] Z. Huang, X. Zhang, M. Reiche, L. Liu, W. Lee, T. Shimizu, S. Senz and U. Gösele, *Nano Lett.*, 2008, 8, 3046.

[164] J. H. Choi, S. K. Han, S. K. Hong, J. H. Song, S. Y. Jeong, Y. S. Cho, D. Kim, Y. S. Nam, K. S. Baek and S. K. Chang, *physica status solidi (a)*, 2008, 205, 1598.

[165] S. Cho, S. Kim, N.-H. Kim, U.-J. Lee, S.-H. Jung, E. Oh and K.-H. Lee, *J. Phys. Chem. C*, 2008, 112, 17760.

[166] H. Wang, M. Zou, P. Larson, E. Sanchez, K. Hobbs, M. Curtis, M. Johnson and O. Awitor, *Nanotechnology*, 2008, 19, 295708.

[167] T. R. Foong, A. Sellinger and X. Hu, *ACS Nano*, 2008, 2, 2250.

[168] L. K. Tan, M. A. Chong and H. Gao, *J. Phys. Chem. C*, 2008, 112, 69.

[169] X. Dou, G. Li, X. Huang and L. Li, *J. Phys. Chem. C*, 2008, 112, 8167.

[170] A. Vlad, M. Mátéfi‐Tempfli, V. A. Antohe, S. Faniel, N. Reckinger, B. Olbrechts, A. Crahay, V. Bayot, L. Piraux and S. Melinte, *Small*, 2008, 4, 557.

[171] X. Gao, L. Liu, B. Birajdar, M. Ziese, W. Lee, M. Alexe and D. Hesse, *Adv. Funct. Mater.*, 2009, 19, 3450.

[172] H. Han, K. Lee, W. Lee, M. Alexe, D. Hesse and S. Baik, *J. Mater. Sci.*, 2009, 44, 5167.

[173] Z. Zhang, T. Shimizu, S. Senz and U. Gösele, *Adv. Mater.*, 2009, 21, 2824.

[174] N. Geyer, Z. Huang, B. Fuhrmann, S. Grimm, M. Reiche, T.-K. Nguyen-Duc, J. de Boor, H. S. Leipner, P. Werner and U. Gösele, *Nano Lett.*, 2009, 9, 3106.

[175] D. Yang, G. Meng, C. Zhu and X. Zhu, *Chem. Commun.*, 2009, 7110.

[176] B. A.-Q. H. Di Ding, W.-C. S. S.-J. Hu, W.-X. X. C. Zhong-Chao, C. B.-W. Y. Yu-De and W. Qi-Ming, *Acta Physica Sinica*, 2009, 7, 098.

[177] H. Kim, H.-B.-R. Lee, W.-H. Kim, S.-J. Park and I. C. Hwang, in *Nanotechnology Materials and Devices Conference, 2009. NMDC'09. IEEE*, IEEE, 2009, 3.

[178] Z. Zhang, T. Shimizu, L. Chen, S. Senz and U. Gösele, *Adv. Mater.*, 2009, 21, 4701.

[179] W. Zhou, X. Niu, G. Min, Z. Song, J. Zhang, Y. Liu, X. Li, J. Zhang and S. Feng, *Microelectron. Eng.*, 2009, 86, 2375.

[180] Z. Huang, T. Shimizu, S. Senz, Z. Zhang, X. Zhang, W. Lee, N. Geyer and U. Gösele, *Nano Lett.*, 2009, 9, 2519.

[181] L. G. Parkinson, N. L. Giles, K. F. Adcroft, M. W. Fear, F. M. Wood and G. E. Poinern, *Tissue Engineering Part A*, 2009, 15, 3753.

[182] H. W. Lee, J. K. Anthony, H.-D. Nguyen, S.-i. Mho, K. Kim, H. Lim, J. Lee and F. Rotermund, *Optics express*, 2009, 17, 19093.

[183] K. A. Lau, H. Duran and W. Knoll, *J. Phys. Chem. B*, 2009, 113, 3179.

[184] K. Sengupta, E. Moyen, M. Macé, A. M. Benoliel, A. Pierres, F. Thibaudau, L. Masson, L. Limozin, P. Bongrand and M. Hanbücken, *Small*, 2009, 5, 449.

[185] H. Shin, Y. Park, Y. Seo and B. Kim, *Journal of the Korean Society of Manufacturing Technology Engineers*, 2009, 18, 697.

[186] J. Huang, S. Y. Chiam, H. H. Tan, S. Wang and W. K. Chim, *Chem. Mater.*, 2010, 22, 4111.

[187] X. Gao, B. J. Rodriguez, L. Liu, B. Birajdar, D. Pantel, M. Ziese, M. Alexe and D. Hesse, *ACS Nano*, 2010, 4, 1099.

[188] L.-C. Chen and B.-H. Liu, *Electrochemical and Solid-State Letters*, 2010, 13, H108.

[189] D. Choi, Y. Choi, S. Hong, T. Kang and L. P. Lee, *Small*, 2010, 6, 1741.

[190] J. Hong, K. Kim, N. Kwon, J. Lee, D. Whang and I. Chung, *Journal of Vacuum Science & Technology A*, 2010, 28, 735.

[191] N. Haberkorn, S. A. Weber, R. Berger and P. Theato, *ACS Appl. Mater. Interfaces*, 2010, 2, 1573.

[192] K.-S. Kim, W.-H. Baek, J.-M. Kim, T.-S. Yoon, H. H. Lee, C. J. Kang and Y.-S. Kim, *Sensors*, 2010, 10, 765.

[193] T. D. Lazzara, K. A. Lau, A. I. Abou-Kandil, A.-M. Caminade, J.-P. Majoral and W. Knoll, *ACS Nano*, 2010, 4, 3909.

[194] D. Ramírez, H. Gómez, G. Riveros, R. Schrebler, R. Henríquez and D. Lincot, *J. Phys. Chem. C*, 2010, 114, 14854.

[195] C.-T. Wu, C.-H. Lin, C. Cheng, C.-S. Wu, H.-C. Ting, F.-C. Chang and F.-H. Ko, *Chem. Mater.*, 2010, 22, 6583.

[196] S. A. Weber, N. Haberkorn, P. Theato and R. Berger, *Nano Lett.*, 2010, 10, 1194.

[197] J. N. Tiwari, F.-M. Pan, T.-M. Chen, R. N. Tiwari and K.-L. Lin, *J. Power Sources*, 2010, 195, 729.

[198] G. D. Sulka, A. Brzózka and L. Liu, *Electrochim. Acta*, 2011, 56, 4972.

[199] A. F. Feil, P. Migowski, J. Dupont, L. Amaral and S. R. Teixeira, *J. Phys. Chem. C*, 2011, 115, 7621.

[200] C. W. Kwon, J. W. Son, J. H. Lee, H. M. Kim, H. W. Lee and K. B. Kim, *Adv. Funct. Mater.*, 2011, 21, 1154.

[201] J. Kim, H. Han, Y. H. Kim, S.-H. Choi, J.-C. Kim and W. Lee, *ACS Nano*, 2011, 5, 3222.

[202] H. Jin and L. G. Liu, in *SPIE NanoScience&Engineering*, International Society for Optics and Photonics, 2011, 810211.

[203] H. Jin, T. W. Chang and L. G. Liu, in *SPIE Solar Energy&Technology*, International Society for Optics and Photonics, 2011, 811118.

[204] K. Noh, C. Choi, H. Kim, Y. Oh, J.-Y. Kim, S.-Y. Jung, T.-Y. Seong and S. Jin, *J. Vac. Sci. Technol. B*, 2011, 29, 06F207.

[205] K. Huang, Y. Li, Z. Wu, C. Li, H. Lai and J. Kang, *Optics express*, 2011, 19, 1301.

[206] X. Lu, Y. Kim, S. Goetze, X. Li, S. Dong, P. Werner, M. Alexe and D. Hesse, *Nano Lett.*, 2011, 11, 3202.

[207] S. H. Lee, B. Cho, S. Yoon, H. Jeong, S. Jon, G. Y. Jung, B. K. Cho, T. Lee and W. B. Kim, *ACS Nano*, 2011, 5, 5543.

[208] J. Kim, Y. H. Kim, S.-H. Choi and W. Lee, *ACS Nano*, 2011, 5, 5242.

[209] M. K. Choi, H. Yoon, K. Lee and K. Shin, *Langmuir*, 2011, 27, 2132.

[210] C.-H. Huang, H.-Y. Lin, S. Chen, C.-Y. Liu, H.-C. Chui and Y. Tzeng, *Optics express*, 2011, 19, 11441.

[211] G. Fois, C. T. Bolger, J. D. Holmes and G. L. Cross, *J. Mater. Chem.*, 2011, 21, 8772.

[212] W. Guan, J. Ghatak, Y. Peng, N. Peng, C. Jeynes, B. Inkson and G. Möbus, *Nanotechnology*, 2012, 23, 045605.

[213] S.-H. Lyu and J.-S. Lee, *J. Mater. Chem.*, 2012, 22, 1852.

[214] L.-J. Li, B. Zhu, S.-J. Ding, H.-L. Lu, Q.-Q. Sun, A. Jiang, D. W. Zhang and C. Zhu, *Nanoscale research letters*, 2012, 7, 1.

[215] N. Kwon, N. Kim, S. Sung, B. Kang and I. Chung, *J. Vac. Sci. Technol. B*, 2012, 30, 041810.

[216] M.-S. Park, G.-D. Yu and K.-S. Shin, *Bulletin of the Korean Chemical Society*, 2012, 33, 83.

[217] Z. Zeng, X. Huang, Z. Yin, H. Li, Y. Chen, H. Li, Q. Zhang, J. Ma, F. Boey and H. Zhang, *Adv. Mater.*, 2012, 24, 4138.

[218] M. Jung, S. K. Kim, S. Lee, T. Lee, S. H. Kim, D. Woo and J. H. Kim, in *Opto-Electronics and Communications Conference (OECC), 2012 17th*, IEEE, 2012, 687.

[219] E. Moyen, L. Santinacci, L. Masson, H. Sahaf, M. Macé, L. Assaud and M. Hanbücken, *International Journal of Nanotechnology*, 2012, 9, 246.

[220] G. Giallongo, C. Durante, R. Pilot, D. Garoli, R. Bozio, F. Romanato, A. Gennaro, G. Rizzi and G. Granozzi, *Nanotechnology*, 2012, 23, 325604.

[221] M. Jung, S. K. Kim, T. Lee, S. Lee, D. Woo and J. H. Kim, in *Nanotechnology (IEEE-NANO), 2012 12th IEEE Conference on*, IEEE, 2012, 1.

[222] Y.-C. Huang, P.-Y. Chen, T.-S. Chin, R.-S. Liu, C.-Y. Huang and C.-H. Lai, *Appl. Phys. Lett.*, 2012, 101, 153106.

[223] J. Fang, I. Aharonovich, I. Levchenko, K. Ostrikov, P. G. Spizzirri, S. Rubanov and S. Prawer, *Cryst. Growth Des.*, 2012, 12, 2917.

[224] M. Raoufi, D. Tranchida and H. Schönherr, *Langmuir*, 2012, 28, 10091.

[225] S.-J. Park, I. Hwang, H. S. Lee, S. Baik and H. Kim, *Journal of Alloys and Compounds*, 2012, 536, 166.

[226] M. M. Maqableh, X. Huang, S.-Y. Sung, K. S. M. Reddy, G. Norby, R. Victora and B. J. Stadler, *Nano Lett.*, 2012, 12, 4102.

[227] S. Yue, Z. Yan, Y. Shi and G. Ran, *Materials Letters*, 2013, 98, 246.

[228] A. Sangar, A. Merlen, P. Torchio, S. Vedraine, F. Flory, L. Escoubas, L. Patrone, G. Delafosse, V. Chevallier and E. Moyen, *Solar Energy Materials and Solar Cells*, 2013, 117, 657.

[229] S.-J. Park, H. Han, H. Rhu, S. Baik and W. Lee, *J. Mater. Chem. C*, 2013, 1, 5330.

[230] I.-C. Chen, Y.-H. Chen, Y.-C. Wang and M.-H. Shih, *Applied Physics A*, 2013, 112, 381.

[231] Y. Song, W. Yin, C. Fernandes and H. E. Ruda, *Thin Solid Films*, 2013, 548, 130.

[232] W. Guan, N. Peng, C. Jeynes, J. Ghatak, Y. Peng, I. M. Ross, U. M. Bhatta, B. J. Inkson and G. Möbus, *Nuclear Instruments and Methods in Physics Research Section B: Beam Interactions with Materials and Atoms*, 2013, 307, 273.

[233] K. Kim, H. D. Nguyen, S. Mho and J. Lee, *International Journal of Photoenergy*, 2013, 2013.

[234] S. Hong, T. Choi, J. H. Jeon, Y. Kim, H. Lee, H. Y. Joo, I. Hwang, J. S. Kim, S. O. Kang and S. V. Kalinin, *Adv. Mater.*, 2013, 25, 2339.

[235] A. Mozalev, R. Calavia, R. M. Vázquez, I. Gràcia, C. Cané, X. Correig, X. Vilanova, F. Gispert-Guirado, J. Hubálek and E. Llobet, *Int. J. Hydrogen Energy*, 2013, 38, 8011.

[236] M. Kim, C. Bae, H. Kim, H. Yoo, J. M. M. Moreno, H. S. Jung, J. Bachmann, K. Nielsch and H. Shin, *J. Mater. Chem. A*, 2013, 1, 14080.

[237] C.-C. Chang, D. Botez, L. Wan, P. F. Nealey, S. Ruder and T. F. Kuech, *J. Vac. Sci. Technol. B*, 2013, 31, 031801.

[238] J. Son, M. Sakhuja, A. J. Danner, C. S. Bhatia and H. Yang, *Solar Energy Materials and Solar Cells*, 2013, 116, 9.

[239] G. Ding, Y. Wu, Y. Weng, W. Zhang and Z. Hu, *Macromolecules*, 2013, 46, 8638.

[240] C. T. Nemes, D. K. Vijapurapu, C. E. Petoukhoff, G. Z. Cheung and D. M. O'Carroll, *Journal of nanoparticle research*, 2013, 15, 1.

[241] H. Y. Jang, S.-K. Lee, S. H. Cho, J.-H. Ahn and S. Park, *Chem. Mater.*, 2013, 25, 3535.

[242] P. P. Pillai, K. Pacławski, J. Kim and B. A. Grzybowski, *Adv. Mater.*, 2013, 25, 1623.

[243] P.-H. Lo, S.-H. Tseng, J.-H. Yeh and W. Fang, *Journal of Micromechanics and Microengineering*, 2013, 23, 035013.

[244] D. Liu, C. Zhang, G. Wang, Z. Shao, X. Zhu, N. Wang and H. Cheng, *Journal of Physics D: Applied Physics*, 2014, 47, 085108.

[245] H. Tang, G. Meng, Q. Huang, C. Zhu, Z. Huang, Z. Li, Z. Zhang and Y. Zhang, *RSC Advances*, 2014, 4, 19654.

[246] G. Jeon, J.-S. Moon, S. Lee, J. H. Lee, B.-S. An, D. Y. Hwang, H. S. Kim, Y. J. Jung, J. K. Kim and S. Y. Yang, *Materials Letters*, 2014, 137, 373.

[247] Z. Feng, C. Jiang, Y. He, S. Chu, G. Chu, R. Peng and D. Li, *Advanced Optical Materials*, 2014, 2, 1174.

[248] D. Yu, H. Huang, L. Lu, J. Che, X. Chen, X. Zhu, Y. Song and D. Li, *Nanotechnology*, 2014, 25, 465303.

[249] D. Choi, C. K. Shin, D. Yoon, D. S. Chung, Y. W. Jin and L. P. Lee, *Nano Lett.*, 2014, 14, 3374.

[250] M. Sharma, P. R. Pudasaini, F. Ruiz-Zepeda, E. Vinogradova and A. A. Ayon, *ACS Appl. Mater. Interfaces*, 2014, 6, 15472.

[251] G. Chen, Y. Wang, H. Wang, M. Cong, L. Chen, Y. Yang, Y. Geng, H. Li, S. Xu and W. Xu, *RSC Advances*, 2014, 4, 54434.

[252] A. M. Abd-Elnaiem, A. Mebed, W. A. El-Said and M. Abdel-Rahim, *Thin Solid Films*, 2014, 570, 49.

[253] D. Shan, L. Huang, X. Li, W. Zhang, J. Wang, L. Cheng, X. Feng, Y. Liu, J. Zhu and Y. Zhang, *J. Phys. Chem. C*, 2014, 118, 23930.

[254] Z. Zuo, K. Zhu, G. Cui, W. Huang, J. Qu, Y. Shi, Y. Liu and G. Ji, *Solar Energy Materials and Solar Cells*, 2014, 125, 248.

[255] F. Grote, L. Wen and Y. Lei, *J. Power Sources*, 2014, 256, 37.

[256] Y. Zheng, W. Wang, Q. Fu, M. Wu, K. Shayan, K. M. Wong, S. Singh, A. Schober, P. Schaaf and Y. Lei, *ChemPlusChem*, 2014, 79, 1622.

[257] Q. Fu, K. M. Wong, Y. Zhou, M. Wu and Y. Lei, *RSC Advances*, 2015, 5, 6172.

[258] Q. Fu, Z. Zhan, J. Dou, X. Zheng, R. Xu, M. Wu and Y. Lei, *ACS Appl. Mater. Interfaces*, 2015, 7, 13322.

[259] K. M. Chahrour, N. M. Ahmed, M. Hashim, N. G. Elfadill, A. M. Al-Diabat and M. Bououdina, *J. Phys. Chem. Solids*, 2015, 87, 1.

[260] D. Choi, C. Kuru, C. Choi, K. Noh, S. Hwang, W. Choi and S. Jin, *Small*, 2015, 11, 3143.

[261] D. Choi, C. Kuru, Y. Kim, G. Kim, T. Kim, R. Chen and S. Jin, *Nanoscale research letters*, 2015, 10, 1.

[262] E. C. Choi, H. J. Kim, J.-H. Boo and B. Hong, *Journal of nanoscience and nanotechnology*, 2015, 15, 8395.

[263] W.-J. Ho, P.-Y. Cheng and K.-Y. Hsiao, *Applied Surface Science*, 2015, 354, 25.

[264] K.-Y. Hsiao, W.-J. Ho, P.-Y. Cheng, C.-W. Yeh, R.-S. Sue, Y.-T. Shen, C.-H. Hu and Y.-J. Deng, in *Next-Generation Electronics (ISNE), 2015 International Symposium on*, IEEE, 2015, 1.

[265] X. Zhang, M. Kang, K. Huang, F. Zhang, S. Lin, X. Gao, X. Lu, Z. Zhang and J. Liu, *Nanoscale research letters*, 2015, 10, 1.

[266] Y. Wang, Y. Wang, H. Wang, X. Wang, M. Cong, W. Xu and S. Xu, *Nanotechnology*, 2015, 27, 025302.

[267] H. Zheng and M. Han, in *Magnetics Conference (INTERMAG), 2015 IEEE*, IEEE, 2015, 1.

[268] H. Zheng, M. Han, L. Zheng, P. Zheng, Q. Wu, L. Deng and H. Qin, *Appl. Phys. Lett.*, 2015, 107, 062401.

[269] L. Zhao, Z. Lu, F. Zhang, G. Tian, X. Song, Z. Li, K. Huang, Z. Zhang, M. Qin and X. Lu, *Scientific reports*, 2015, 5.

[270] Q. Kai, Z. Yuhua, Z. Tianwei, L. Zhi, Z. Jun, L. Chuanbo and C. Buwen, *Journal of Semiconductors*, 2015, 36, 104005.

[271] M. Balde, A. Vena and B. Sorli, *Sensors and Actuators B: Chemical*, 2015, 220, 829.

[272] G. He-shuai, F. Qun, L. Wei, Z. Xian-zheng, L. Bo, W. Ming-hong and L. Yong, *J. Shanghai Uni. (Nat. Sci.)*, 2015, 21, 54.

[273] G. Tian, F. Zhang, J. Yao, H. Fan, P. Li, Z. Li, X. Song, X. Zhang, M. Qin and M. Zeng, *ACS Nano*, 2015.

[274] W. Guo, R. Kirste, Z. Bryan, I. Bryan, M. Gerhold, R. Collazo and Z. Sitar, *J. Appl. Phys.*, 2015, 117, 113107.

[275] H. Dang and V. P. Singh, *Scientific reports*, 2015, 5.

[276] T. Ozel, M. J. Ashley, G. R. Bourret, M. B. Ross, G. C. Schatz and C. A. Mirkin, *Nano Lett.*, 2015, 15, 5273.

[277] C. Desrousseaux, R. Cueff, C. Aumeran, G. Garrait, B. Mailhot-Jensen, O. Traoré and V. Sautou, *PLoS One*, 2015, 10, e0135632.

[278] J. Kim, D. H. Lee, J. H. Kim and S.-H. Choi, *ACS Appl. Mater. Interfaces*, 2015, 7, 24242.

[279] M. S. Sander, M. J. Cote, W. Gu, B. M. Kile and C. P. Tripp, *Adv. Mater.*, 2004, 16, 2052.

[280] T. R. Foong, Y. Shen, X. Hu and A. Sellinger, *Adv. Funct. Mater.*, 2010, 20, 1390.

[281] Y. Mei, X. Wu, X. Li, X. Bao, X. Wang, Z. Hu and G. Siu, *J. Cryst. Growth*, 2003, 255, 414.

[282] T. Suntola, in *AVS Topical Conference on Atomic Layer Deposition (ALD2004)*.

[283] S. M. George, *Chemical reviews*, 2009, 110, 111.

[284] J. Liu, M. N. Banis, X. Li, A. Lushington, M. Cai, R. Li, T.-K. Sham and X. Sun, *J. Phys. Chem. C*, 2013, 117, 20260.

[285] M. Ritala and M. Leskela, *Handbook of thin film materials*, 2001, 1, 103.

[286] V. Miikkulainen, M. Leskelä, M. Ritala and R. L. Puurunen, *J. Appl. Phys.*, 2013, 113, 021301.

[287] V. Pore, A. Rahtu, M. Leskelä, M. Ritala, T. Sajavaara and J. Keinonen, *Chem. Vap. Deposition*, 2004, 10, 143.

[288] R. L. Puurunen, *J. Appl. Phys.*, 2005, 97, 121301.

[289] C. Marichy, M. Bechelany and N. Pinna, *Adv. Mater.*, 2012, 24, 1017.

[290] G. Sveshnikova, S. Kol'tsov and V. Aleskovskii, *J. Appl. Chem. USSR*, 1967, 40, 2644.

[291] M. Ritala, M. Leskelä, E. Nykänen, P. Soininen and L. Niinistö, *Thin Solid Films*, 1993, 225, 288.

[292] J. Aarik, A. Aidla, V. Sammelselg, H. Siimon and T. Uustare, *J. Cryst. Growth*, 1996, 169, 496.

[293] M. Cameron, I. Gartland, J. Smith, S. Diaz and S. George, *Langmuir*, 2000, 16, 7435.

[294] N. G. Kubala, P. C. Rowlette and C. A. Wolden, *J. Phys. Chem. C*, 2009, 113, 16307.

[295] Y. Mi, L. Wen, R. Xu, Z. Wang, D. Cao, Y. Fang and Y. Lei, *Adv. Energy Mater.*, 2016, 6, 1501496.

[296] Y. J. Hwang, C. Hahn, B. Liu and P. Yang, *ACS Nano*, 2012, 6, 5060.

[297] L. K. Tan, M. K. Kumar, W. W. An and H. Gao, *ACS Appl. Mater. Interfaces*, 2010, 2, 498.

[298] R. L. Puurunen, T. Sajavaara, E. Santala, V. Miikkulainen, T. Saukkonen, M. Laitinen and M. Leskelä, *Journal of nanoscience and nanotechnology*, 2011, 11, 8101.

[299] S.-Y. Lu, C.-W. Tang, Y.-H. Lin, H.-F. Kuo, Y.-C. Lai, M.-Y. Tsai, H. Ouyang and W.-K. Hsu, *Appl. Phys. Lett.*, 2010, 96, 231915.

[300] C. Prasittichai, J. R. Avila, O. K. Farha and J. T. Hupp, *J. Am. Chem. Soc.*, 2013, 135, 16328.

[301] X. Liang, A. D. Lynn, D. M. King, S. J. Bryant and A. W. Weimer, *ACS Appl. Mater. Interfaces*, 2009, 1, 1988.

[302] A. Szeghalmi, E. B. Kley and M. Knez, *J. Phys. Chem. C*, 2010, 114, 21150.

[303] Y. Zhou, D. M. King, J. Li, K. S. Barrett, R. B. Goldfarb and A. W. Weimer, *Ind. Eng. Chem. Res.*, 2010, 49, 6964.

[304] H. Kumagai, M. Matsumoto, K. Toyoda, M. Obara and M. Suzuki, *Thin Solid Films*, 1995, 263, 47.

[305] V. Sammelselg, A. Tarre, J. Lu, J. Aarik, A. Niilisk, T. Uustare, I. Netšipailo, R. Rammula, R. Pärna and A. Rosental, *Surf. Coat. Technol.*, 2010, 204, 2015.

[306] N. G. Kubala and C. A. Wolden, *Thin Solid Films*, 2010, 518, 6733.

[307] V. Pore, T. Kivelä, M. Ritala and M. Leskelä, *Dalton Trans.*, 2008, 6467.

[308] J. Aarik, A. Aidla, T. Uustare, K. Kukli, V. Sammelselg, M. Ritala and M. Leskelä, *Applied Surface Science*, 2002, 193, 277.

[309] I. Soroka, M. Rooth, J. Lu, M. Boman, P. Svedlindh, J.-O. Carlsson and A. Harsta, *J. Appl. Phys.*, 2009, 106, 4313.

[310] M. Rooth, R. A. Quinlan, E. Widenkvist, J. Lu, H. Grennberg, B. C. Holloway, A. Hårsta and U. Jansson, *J. Cryst. Growth*, 2009, 311, 373.

[311] K. Kukli, M. Ritala, M. Schuisky, M. Leskelä, T. Sajavaara, J. Keinonen, T. Uustare and A. Hårsta, *Chem. Vap. Deposition*, 2000, 6, 303.

[312] K. Kukli, A. Aidla, J. Aarik, M. Schuisky, A. Hårsta, M. Ritala and M. Leskelä, *Langmuir*, 2000, 16, 8122.

[313] M. Schuisky, A. Hårsta, A. Aidla, K. Kukli, A. A. Kiisler and J. Aarik, *J. Electrochem. Soc.*, 2000, 147, 3319.

[314] M. Schuisky, K. Kukli, J. Aarik, J. Lu and A. Hårsta, *J. Cryst. Growth*, 2002, 235, 293.

[315] I. Alessandri, M. Zucca, M. Ferroni, E. Bontempi and L. E. Depero, *Small*, 2009, 5, 336.

[316] E. R. Cleveland, P. Banerjee, I. Perez, S. B. Lee and G. W. Rubloff, *ACS Nano*, 2010, 4, 4637.

[317] T. Blanquart, J. Niinistö, M. Gavagnin, V. Longo, V. R. Pallem, C. Dussarrat, M. Ritala and M. Leskelä, *Chem. Mater.*, 2012, 24, 3420.

[318] M. Kemell, V. Pore, M. Ritala, M. Leskelä and M. Lindén, *J. Am. Chem. Soc.*, 2005, 127, 14178.

[319] T. W. Hamann, A. B. Martinson, J. W. Elam, M. J. Pellin and J. T. Hupp, *J. Phys. Chem. C*, 2008, 112, 10303.

[320] M. Popovici, S. Van Elshocht, N. Menou, J. Swerts, D. Pierreux, A. Delabie, B. Brijs, T. Conard, K. Opsomer and J. Maes, *J. Electrochem. Soc.*, 2010, 157, G1.

[321] I.-D. Kim, H. L. Tuller, H.-S. Kim and J.-S. Park, *Appl. Phys. Lett.*, 2004, 85.

[322] A. Alekhin, G. Lapushkin, A. Markeev, A. Sigarev and V. Toknova, *Journal of Surface Investigation. X-ray, Synchrotron and Neutron Techniques*, 2010, 4, 379.

[323] S. Duenas, H. Castán, H. García, E. San Andrés, M. Toledano-Luque, I. Mártil, G. González-Díaz, K. Kukli, T. Uustare and J. Aarik, *Semiconductor Science and Technology*, 2005, 20, 1044.

[324] I. Jõgi, M. Pärs, J. Aarik, A. Aidla, M. Laan, J. Sundqvist, L. Oberbeck, J. Heitmann and K. Kukli, *Thin Solid Films*, 2008, 516, 4855.

[325] Z. Zhang, G. Triani and L.-J. Fan, *Journal of Materials Research*, 2008, 23, 2472.

[326] A. Sinha, D. W. Hess and C. L. Henderson, *J. Vac. Sci. Technol. B*, 2006, 24, 2523.

[327] J. Lee, H. Ju, J. K. Lee, H. S. Kim and J. Lee, *Electrochemistry Communications*, 2010, 12, 210.

[328] Q. Xie, J. Musschoot, D. Deduytsche, R. L. Van Meirhaeghe, C. Detavernier, S. Van den Berghe, Y.-L. Jiang, G.-P. Ru, B.-Z. Li and X.-P. Qu, *J. Electrochem. Soc.*, 2008, 155, H688.

[329] J. Joo and S. M. Rossnagel, *Journal of the Korean Physical Society*, 2009, 54, 1048.

[330] J. P. Lee, M. H. Park, T.-M. Chung, Y.-S. Kim and M. M. Sung, *Bulletin of the Korean Chemical Society*, 2004, 25, 475.

[331] Y. A. Wasslen, E. Tois, S. Haukka, K. A. Kreisel, G. P. Yap, M. D. Halls and S. T. Barry, *Inorg. Chem.*, 2010, 49, 1976.

[332] S. Potts, W. Keuning, E. Langereis, G. Dingemans, M. Van de Sanden and W. Kessels, *J. Electrochem. Soc.*, 2010, 157, P66.

[333] M. Rose, J. Bartha and I. Endler, *Applied Surface Science*, 2010, 256, 3778.

[334] M. Rose, J. Niinistö, P. Michalowski, L. Gerlich, L. Wilde, I. Endler and J. W. Bartha, *J. Phys. Chem. C*, 2009, 113, 21825.

[335] W. Brattain and C. Garrett, *Bell System Technical Journal*, 1955, 34, 129.

[336] R. Marcus, *Annu. Rev. Phys. Chem.*, 1964, 15, 155.

[337] H. Gerischer, *J. Electrochem. Soc.*, 1966, 113, 1174.

[338] Y. V. Pleskov and Y. Y. Gurevich, 1986.

[339] A. Fujishima, *nature*, 1972, 238, 37.

[340] M. R. Hoffmann, S. T. Martin, W. Choi and D. W. Bahnemann, *Chemical reviews*, 1995, 95, 69.

[341] D. Tryk, A. Fujishima and K. Honda, *Electrochim. Acta*, 2000, 45, 2363.

[342] J. H. Park, S. Kim and A. J. Bard, *Nano Lett.*, 2006, 6, 24.

[343] A. J. Nozik, *Annu. Rev. Phys. Chem.*, 1978, 29, 189.

[344] A. Mills and S. Le Hunte, *Journal of photochemistry and photobiology A: Chemistry*, 1997, 108, 1.

[345] B. O'Regan, D. T. Schwartz, S. M. Zakeeruddin and M. Grätzel, *Adv. Mater.*, 2000, 12, 1263.

[346] S. Linic, P. Christopher and D. B. Ingram, *Nat. Mater.*, 2011, 10, 911.

[347] K. Shankar, J. I. Basham, N. K. Allam, O. K. Varghese, G. K. Mor, X. Feng, M. Paulose, J. A. Seabold, K.-S. Choi and C. A. Grimes, *J. Phys. Chem. C*, 2009, 113, 6327.

[348] M. Liu, N. de Leon Snapp and H. Park, *Chemical Science*, 2011, 2, 80.

[349] G. Liu, H. G. Yang, J. Pan, Y. Q. Yang, G. Q. Lu and H.-M. Cheng, *Chemical reviews*, 2014, 114, 9559.

[350] M. F. Weber and M. J. Dignam, *J. Electrochem. Soc.*, 1984, 131, 1258.

[351] J. R. Bolton, S. J. Strickler and J. S. Connolly, *Nature*, 1985, 316, 495.

[352] S. M. Sze, *Semiconductor Devices: Physics and Technology*, Wiley, 2001.

[353] H. Masuda, H. Asoh, M. Watanabe, K. Nishio, M. Nakao and T. Tamamura, *Adv. Mater.*, 2001, 13, 189.

[354] H. H. Wang, C. Y. Liu, S. B. Wu, N. W. Liu, C. Y. Peng, T. H. Chan, C. F. Hsu, J. K. Wang and Y. L. Wang, *Adv. Mater.*, 2006, 18, 491.

[355] H. Masuda, K. Yada and A. Osaka, *Jpn. J. Appl. Phys.*, 1998, 37, L1340.

[356] S.-F. Leung, M. Yu, Q. Lin, K. Kwon, K.-L. Ching, L. Gu, K. Yu and Z. Fan, *Nano Lett.*, 2012, 12, 3682.

[357] K. Shankar, G. K. Mor, H. E. Prakasam, S. Yoriya, M. Paulose, O. K. Varghese and C. A. Grimes, *Nanotechnology*, 2007, 18, 065707.

[358] M. Zhang, Y.-N. Wang, E. Moulin, D. Grützmacher, C.-J. Chien, P.-C. Chang, X. Gao, R. Carius and J. G. Lu, *J. Mater. Chem.*, 2012, 22, 10441.

[359] H. Lin, C. Huang, W. Li, C. Ni, S. Shah and Y. Tseng, *Appl. Catal. B*, 2006, 68, 1.

[360] D.-H. Kwon, K. M. Kim, J. H. Jang, J. M. Jeon, M. H. Lee, G. H. Kim, X.-S. Li, G.-S. Park, B. Lee and S. Han, *Nat. Nanotechnol.*, 2010, 5, 148.

[361] F. Le, D. W. Brandl, Y. A. Urzhumov, H. Wang, J. Kundu, N. J. Halas, J. Aizpurua and P. Nordlander, *ACS Nano*, 2008, 2, 707.

[362] C.-M. Liu, C. Chen and H.-E. Cheng, *J. Electrochem. Soc.*, 2011, 158, K58.

[363] Y. H. Chang, C. M. Liu, H. E. Cheng and C. Chen, *ACS Appl. Mater. Interfaces*, 2013, 5, 3549.

[364] S. J. Park, J. P. Lee, J. S. Jang, H. Rhu, H. Yu, B. Y. You, C. S. Kim, K. J. Kim, Y. J. Cho, S. Baik and W. Lee, *Nanotechnology*, 2013, 24, 295202.

[365] P. K. Jain, W. Huang and M. A. El-Sayed, *Nano Lett.*, 2007, 7, 2080.

[366] K. Crozier, A. Sundaramurthy, G. Kino and C. Quate, *J. Appl. Phys.*, 2003, 94, 4632.

[367] A. Sundaramurthy, K. Crozier, G. Kino, D. Fromm, P. Schuck and W. Moerner, *Phys. Rev. B*, 2005, 72, 165409.

[368] A. Hagfeldt and M. Graetzel, *Chemical Reviews*, 1995, 95, 49.

[369] Y. Mi, L. Wen, R. Xu, Z. Wang, D. Cao, Y. Fang and Y. Lei, *Adv. Energy Mater.*, 2015.

[370] S. Tarish, Z. Wang, A. Al-Haddad, C. Wang, A. Ispas, H. Romanus, P. Schaaf and Y. Lei, *J. Phys. Chem. C*, 2015, 119, 1575.

[371] Y. Sugimoto and L. Peter, *J. Electroanal. Chem.*, 1995, 386, 183.

[372] M. Miyake, K. Murase, T. Hirato and Y. Awakura, *J. Electroanal. Chem.*, 2004, 562, 247.

[373] X. Zhang, Y. Liu, S.-T. Lee, S. Yang and Z. Kang, *Energy Environ. Sci.*, 2014, 7, 1409.

[374] Z. Pan, Y. Qiu, J. Yang, M. Liu, L. Zhou, Y. Xu, L. Sheng, X. Zhao and Y. Zhang, *J. Mater. Chem. A*, 2015, 3, 4004.

[375] G. Wang, H. Wang, Y. Ling, Y. Tang, X. Yang, R. C. Fitzmorris, C. Wang, J. Z. Zhang and Y. Li, *Nano Lett.*, 2011, 11, 3026.

[376] J. Shi, Y. Hara, C. Sun, M. A. Anderson and X. Wang, *Nano Lett.*, 2011, 11, 3413.

[377] M. H. Lee, K. Takei, J. Zhang, R. Kapadia, M. Zheng, Y. Z. Chen, J. Nah, T. S. Matthews, Y. L. Chueh, J. W. Ager and A. Javey, *Angew. Chem. Int. Ed. Engl.*, 2012, 51, 10760.

[378] H. Zhao, M. Zhou, L. Wen and Y. Lei, *Nano Energy*, 2015, 13, 790.

[379] J. M. Foley, M. J. Price, J. I. Feldblyum and S. Maldonado, *Energy Environ. Sci.*, 2012, 5, 5203.

[380] Z. Zhang and P. Wang, *Energy Environ. Sci.*, 2012, 5, 6506.

[381] Y. J. Hwang, A. Boukai and P. Yang, *Nano Lett.*, 2008, 9, 410.

[382] B. Chen, J. Hou and K. Lu, *Langmuir*, 2013, 29, 5911.

[383] W. Q. Fang, Z. Huo, P. Liu, X. L. Wang, M. Zhang, Y. Jia, H. Zhang, H. Zhao, H. G. Yang and X. Yao, *Chem. Eur. J.*, 2014, 20, 11439.

[384] S. Y. Noh, K. Sun, C. Choi, M. Niu, M. Yang, K. Xu, S. Jin and D. Wang, *Nano Energy*, 2013, 2, 351.

[385] M. Zhou, J. Bao, Y. Xu, J. Zhang, J. Xie, M. Guan, C. Wang, L. Wen, Y. Lei and Y. Xie, *ACS Nano*, 2014, 8, 7088.

[386] H. H. Nguyen, W. Prellier, J. Sakai and A. Ruyter, *J. Appl. Phys.*, 2004, 95, 7378.

[387] L. Liang, Y. Xu, C. Wang, L. Wen, Y. Fang, Y. Mi, M. Zhou, H. Zhao and Y. Lei, *Energy Environ. Sci.*, 2015, 8, 2954.

[388] F. Grote, H. Zhao and Y. Lei, *J. Mater. Chem. A*, 2015, 3, 3465.

[389] Y. H. Do, J. S. Kwak, Y. C. Bae, J. H. Lee, Y. Kim, H. Im and J. P. Hong, *Curr. Appl. Phys.*, 2010, 10, e71.

[390] J. S. Kwak, Y. H. Do, Y. C. Bae, H. S. Im, J. H. Yoo, M. G. Sung, Y. T. Hwang and J. P. Hong, *Appl. Phys. Lett.*, 2010, 96, 223502.

[391] J. Kwon, A. A. Sharma, J. A. Bain, Y. N. Picard and M. Skowronski, *Adv. Funct. Mater.*, 2015, 25, 2876.

[392] D. S. Jeong, H. Schroeder, U. Breuer and R. Waser, *J. Appl. Phys.*, 2008, 104, 123716.

[393] J. H. Kim, Y. C. Bae, A. R. Lee, K. H. Baek and J. P. Hong, *Appl. Phys. Lett.*, 2015, 106, 033506.

Scientific Contributions

During the Ph.D. period, I have coauthored 6 papers published in SCI-indexed international scientific journals including *ACS Nano*, *Nano Energy*, *Journal of Materials Chemistry – C*, *Journal of Physical Chemistry – C* and *Advanced Materials Technologies*. The resulted papers from this dissertation are 5 papers, up to date, 4 papers are published and 1 manuscripts is submitted. Furthermore, I have 4 jointly published papers. I have given 19 contributions to conferences, including 2 conference proceedings, 13 talks and 6 posters.

1. Publications in SCI-indexed Scientific Journals

The following are the total publications in SCI-indexed international scientific journals during the period of Ph.D. studies.

1. A. Al-Haddad, Z. Wang, M. Zhou, S. Tarish, R. Vellacheri, Y. Lei, Constructing Well-Ordered CdTe/TiO_2 Core/Shell Nanowire Arrays for Solar Energy Conversion. *Small*, 2016, doi:10.1002/smll.201601412.

2. A. Al-Haddad, C. Wang, H. Qi, F. Grote, L. Wen, J. Bernhard, R. Vellacheri, S. Tarish, G. Nabi, U. Kaiser, Y. Lei, Highly-Ordered 3D Vertical Resistive Switching Memory Arrays with Ultralow Power Consumption and Ultrahigh Density. *ACS Appl. Mater. Interfaces*, 2016, 8, 23348-23355.

3. R. Vellacheri, H. Zhao, M. Mühlstädt, J. Ming, A. Al-Haddad, M. Wu, K. D. Jandt, Lei Y., All-Solid-State Cable-Type Supercapacitors with Ultra-High Rate Capability. *Adv. Mater. Technol.* 2016, doi: 10.1002/admt.201600012.

4. S. Tarish, A. Al-Haddad, R. Xu, D. Cao, Z. Wang, S. Qu, G. Nabi, Y. Lei, The Shift of the Optical Absorption Band Edge of ZnO/ZnS Core/Shell Nanotube Arrays Beyond Quantum Effects. *J. Mater. Chem. C* 2016, 4, 1369-1374.

5. A. Al-Haddad, Z. Zhan, C. Wang, S. Tarish, R. Vellacheria, Y. Lei, Facile Transferring of Wafer-Scale Ultrathin Alumina Membranes onto Substrates for Nanostructure Patterning. *ACS Nano* 2015, 9, 8584-8591.

6. A. Al-Haddad, Z. Wang, R. Xu, H. Qi, R. Vellacheri, U. Kaiser, Y. Lei, Dimensional Dependence of the Optical Absorption Band Edge of TiO_2 Nanotube Arrays Beyond the Quantum Effect. *J. Phys. Chem. C* 2015, 119, 16331-16337.

7. S. Tarish, Z. Wang, A. Al-Haddad, C. Wang, A. Ispas, H. Romanus, P. Schaaf, Y. Lei, Synchronous Formation of ZnO/ZnS Core/Shell Nanotube Arrays with Removal of Template for Meliorating Photoelectronic Performance. *J. Phys. Chem. C* 2015, 119, 1575-1582.

8. R. Vellacheri, A. Al-Haddad, H. Zhao, W. Wang, C. Wang, Y. Lei, High Performance Supercapacitor for Efficient Energy Storage under Extreme Environmental Temperatures. *Nano Energy* 2014, 8, 231-237.

2. Unpublished manuscripts

1. A. Al-Haddad, H. Zhao, R. Xu, S. Tarish, R. Vellacheri, Y. Lei, Facile Construction of Novel TiO_2╫Si Heterostructure Arrays in Wafer-Scale for Photoelectrochemical Water Splitting. (Submitted to *J. Mater. Chem. A*.2016)

2. R. Vellacheri, H. Zhao, K. S. Krishna, A. Al-Haddad, Nasori, J. Ming, Y. Wang, M. Wu, Y. Lei, Cable-Type Supercapacitor Electrodes with High Specific Capacitance and Ultrahigh Rate Capability. (To be submitted)

3. Conference Contribution

The contributions to conferences during the Ph.D. period are as following:

1. A. Al-Haddad, H. P. Zhao, Z. Zhan, L. Y. Wen, M. Zhou, Y. Lei, Templates for Nanostructuring Functional Materials Toward Potential Device Applications, 2nd International Conference & 4th International MacroNano-Colloquium on the Challenges and Perspectives of Functional Nanostructures (CPFN), June 30-31.2015, Ilmenau, Germany. **(Poster)**

2. Z. Zhan, A. Al-Haddad, R. Xu, Y. Mi, H. Zhao, Y. Lei, Highly Controllable Surface Plasmon Resonance (SPR) Property Based on the Improved Ultrathin Alumina Membrane (UTAM) Technique, 2nd International Conference & 4th International MacroNano-Colloquium on the Challenges and Perspectives of Functional Nanostructures (CPFN), June 30-31.2015, Ilmenau, Germany. **(Talk)**

3. Z. Wang, D. Cao, Y. Mi, N. Nasori, A. Al-Haddad, S. Tarish, W. Wang, L. Cheng, Y. Lei, Manipulations of Various Nano-structures for Photoelectrochemical and Electronic Applications, 1st International Conference & 3rd International MacroNano-Colloquium on the Challenges and Perspectives of Functional Nanostructures (CPFN), July 29-31.2014, Ilmenau, Germany. **(Talk)**

4. H. Zhao, Z. Zhan, A. Al-Haddad, F. Grote, L. Wen, Y. Mi, Y. Zheng, W. Wang, Y. Lei, Aluminum Oxide (AAO) Template and Ultra-Thin Alumina Membrane (UTAM) Technique for Preparation of Functional Nanostructures, 1st International Conference

& 3rd International MacroNano-Colloquium on the Challenges and Perspectives of Functional Nanostructures (CPFN), July 29-31.2014, Ilmenau, Germany. **(Poster)**

5. R. Vellacheri, F. Grote, L. Wen, H. Zhao, A. Al-Haddad, Y. Mi, Y. Lei, High Performance Supercapacitors for Efficient Energy Storage, 1st International Conference & 3rd International MacroNano-Colloquium on the Challenges and Perspectives of Functional Nanostructures (CPFN), July 29-31.2014, Ilmenau, Germany. **(Poster)**

6. A. Al-Haddad, S. Tarish, R. Vellacheri, W. Wang, F. Grote, Z. Zhan, Y. Lei, Diameter-Dependent Absorption Edges of One-Dimensional TiO_2 Nanotube Arrays by Atomic Layer Deposition, 78th Annual Conference of the DPG, March 30- April 04, 2014, Dresden, Germany. **(Talk)**

7. A. Al-Haddad, S. Tarish, R. Vellacheri, Y. Zheng, L. Y. Wen, Y. Xu, Y. Lei, Tunable Silicon Nanowire Arrays Based on A New Method to Transfer Large Area of Ultra-Thin Alumina Membranes, 78th Annual Conference of the DPG, March 30- April 04, 2014, Dresden, Germany. **(Poster)**

8. Y. Zheng, W. Wang, A. Al-Haddad, H. Zhao, C. Wang, Y. Lei, Organic Surface Nano-Patterns Prepared by Using Nano-Porous Templates, 78th Annual Conference of the DPG, March 30- April 04, 2014, Dresden, Germany. **(Talk)**

9. S. Tarish, C. Wang, A. Al-Haddad, Z. Wang, Z. Zhan, Y. Lei, Controlled fabrication of ZnO/ZnS Core-Shell Nanotube Arrays Prepared on Anodic Aluminum Oxide with Enhanced Photoluminces and Electronic Properties, 78th Annual Conference of the DPG, March 30- April 04, 2014, Dresden, Germany. **(Talk)**

10. R. Vellacheri, A. Al-Haddad, W. Wang, H. Zhao, C. Wang, Z. Wang, Y. Lei, Graphene-Based Supercapacitors for Energy Storage Under Extreme Temperature Conditions, 78th Annual Conference of the DPG, March 30- April 04, 2014, Dresden, Germany. **(Talk)**

11. W. Wang, Y. Zheng, R. Vellacheri, L. Cheng, C. Wang, H. Zhao, A. Al-Haddad, Y. Lei, Metal Plasmonic Structures Based on Anodic Aluminum Oxide (AAO) and Ultrathin Alumina Membranes (UTAM) for SERS and Sensor Applications, 78th Annual Conference of the DPG, March 30- April 04, 2014, Dresden, Germany. **(Talk)**

12. A. Al-Haddad, H. P. Zhao, R. Vellacheri, Y. Mi, S. Tarisch, Y. Lei, Large Aria Ultrathin Alumina Membranes to Fabricate Highly Ordered Heterojunction Core-Shell Nanostructure, 77th Annual Conference of the DPG, March 10-15, 2013, Regensburg, Germany. **(Talk)**

13. R. Vellacheri, H. P. Zhao, A. Al-Haddad, F. Grote, Y. Lei, High-Performance Supercapacitors Based on Ordered Nanoarrays, 77th Annual Conference of the DPG, March 10-15, 2013, Regensburg, Germany. **(Talk)**

14. F. Grote, L. Wen, Z. Zhan, A. Al-Haddad, Y. Mi, S. Tarish, C. Wang, R. Vellacheri, H. Zhao, Y. Lei, Realizing Three-Dimensional Nanostructures Using Nano-Templates: Concept, Properties and High Performance Devices, 77th Annual Conference of the DPG, March 10-15, 2013, Regensburg, Germany. **(Talk)**

15. L. Wen, Y. Mi, F. Grote, A. Al-Haddad, Z. Zhan, H. Zhao, Y. Lei, Nano-Engineered Three-Dimensional Pt/MnO_2 Thin Films for Flexible, High Performance Supercapacitors, 77th Annual Conference of the DPG, March 10-15, 2013, Regensburg, Germany. **(Talk)**

16. W. Wang, Y. Zheng, A. Al-Haddad, Y. Mi, H. Zhao, Y. Lei, Fabrication of Plasmonic Ag/Au Arrays Used as Sensitive Platform for Glucose Assay, 77th Annual Conference of the DPG, March 10-15, 2013, Regensburg, Germany. **(Talk)**

17. S. Tarish, C. Wang, A. Al-Haddad, Z. Zhan, H. Zhao, Y. Lei, Fabrication and Characteristics of ZnO/ZnS Core-Shell Nanotubes Based on Template-Fabrication Techniques, 77th Annual Conference of the DPG, March 10-15, 2013, Regensburg, Germany. **(Poster)**

18. A. Al-Haddad, Y. Fang, H. P. Zhao, Y. Lei, Three-Dimensional TiO_2 Nanotube Arrays for Photo-Device Application, 76th Annual Conference of the DPG, April 25-30, 2012, Berlin, Germany. **(Poster)**

19. L. Wen, H. Zhao, F. Grote, Y. Mi, R. Vellacheri, Z. Zhan, A. Al-Haddad, Y. Fang, K. M. Wong, Y. Lei, Template-Based Surface Nano-Patterning to Realize High Performance Devices, 76th Annual Conference of the DPG, April 25-30, 2012, Berlin, Germany. **(Talk)**

Declaration

I hereby confirm that this Ph.D. dissertation entitled "Large area of Ultrathin Alumina Membranes Toward Innovative Heterogeneous Nanostructure Arrays for Solar Energy Conversion" represents my own work for the degree of Doctor of Philosophy under the supervision of Prof. Dr. Yong Lei. All dates and information in this work that have been directly or indirectly derived from other sources are clearly stated. This dissertation has not been submitted, in part or in whole, for the award of any other degree or examination in any other University or other tertiary institution. I have acknowledged all the sources of help, and I have made a clear statement of what was done by others. Most of the results have been published in scientific journals or elsewhere. I am aware that any falsity of this declaration would be regarded as an attempt at deception and will cause the derogation of the doctoral procedure.

Ilmenau, May 2016
Ahmed Al-Haddad